An analysis of two-phase flows in conditions relevant to microgravity

by

SANTIAGO ARIAS

ACTA DE QUALIFICAIÓ DE LA TESI DOCTORAL

Reunit el tribunal integrat pels sota signants per jutjar la tesi doctoral:

Títol de la tesi: .....
Autor de la tesi: .....

Acorda atorgar la qualificació de:

- ☐ No apte
- ☐ Aprovat
- ☐ Notable
- ☐ Excel·lent
- ☐ Excel·lent Cum Laude

Barcelona, ... de/d' ..... de .....

El President

..... (nom i cognoms)

El Sectretari

..... (nom i cognoms)

El Vocal

..... (nom i cognoms)

El Vocal

..... (nom i cognoms)

El Vocal

..... (nom i cognoms)

An analysis of two-phase flows in conditions relevant to microgravity

by

SANTIAGO ARIAS

A Thesis Submitted to
UNIVERSITAT POLITÈCNICA DE CATALUNYA
in Partial Fulfillment of the
Requirements for the Degree of
Doctor of Philosophy
in Aerospace Science and Technology

Thesis Supervisor:
RICARD GONZÁLEZ-CINCA

Aerospace Science and Technology Program
UNIVERSITAT POLITÈCNICA DE CATALUNYA

Barcelona, 2011

To my family

Abstract

Promising technological applications of two-phase flows in space have captured the increasing interest of the space sector, provoking a strong demand for more fundamental knowledge. Great efforts have been made in recent decades to study the behavior of two-phase flows in low-gravity environments, which is expected to be different than the behavior observed in the presence of gravitational forces. Nevertheless, many phenomena are still poorly understood. The development of any of these new technologies demands a better knowledge of two-phase flows.

In this manuscript we address questions regarding the generation of gas-liquid flows and their behavior in conditions relevant for a microgravity environment. In particular, we focus on an air-water mixture formed in a capillary T-junction. To this end, an experimental setup has been designed to accurately control both gas and liquid flow rates. We performed a quantitative characterization on ground of the T-junction, whose operation is robust to changes in gravity level. Its main performance is the generation of bubbles at a regular frequency with small size dispersion. We obtained two working regimes of the T-junction and identified the crossover region between them.

Bubble, slug, churn and annular flow regimes have been observed during the experiments and a flow pattern map has been plotted. We present an experimental study on the bubble-slug transition in microgravity-related conditions. In addition, we address questions regarding the existence of a critical void fraction in order for the bubble-slug transition to occur.

The gas-liquid flow has been characterized by measuring the bubble generation frequency as well as the bubble and liquid slug sizes. Since bubble dynamics is also expected to be different in the absence of buoyancy, the bubble velocity has also been studied. The mean void fraction appears as one relevant parameter that allows for the prediction of frequency, bubble velocity, and lengths. We propose curves obtained empirically for the behavior of generation frequency, the bubble velocity and the lengths. The dependence of the frequency on the Strouhal dimensionless number has been analyzed.

A numerical study of the formation of mini-bubbles in a 2D T-junction by means of the fluid dynamics numerical code JADIM is also presented. Simulations were carried out for different flow conditions, giving rise to results on the bubble generation frequency, bubble velocity, void fraction and characteristic lengths. Numerical results have been then compared with experimental data.

Acknowledgements

During the evolution of this thesis I have become indebted to many people, only a portion of whom I have the space to acknowledge here.

I owe a great deal to my supervisor, Dr. Ricard González-Cinca, who throughout the entire realization of this thesis has continuously supported, encouraged and enlightened me. His continuous good mood and humor have been very important to me.

I would like to thank to Dr. Catherine Colin and Dr. Valentina Shevtsova for the care with which they reviewed the original manuscript of this thesis and for their useful feedback. I would also like to thank the other committee members: Dr. Jaume Casademunt, Dr. David Pino, Dr. Laureano Ramírez-Piscina, Dr. Francesca Ribas and Dr. Véronique Roig.

Chapter 6 benefited greatly from working with Dr. Jaume Casademunt, Dr. Laureano Ramírez-Piscina and Dr. Xavier Ruiz, as well as from their extensive knowledge and experience.

I would like to acknowledge the debt I owe to Dr. Dominique Legendre. His deep knowledge on Computational Fluid Dynamics has been of great help in developing Chapter 8. I am indebted to the *Institut de Mécanique des Fluides de Toulouse* (IMFT), especially to the Interface Group, for its kind hospitality and assistance. I wish to express my sincerest gratitude to Dr. Catherine Colin and Dr. Dominique Legendre for making my stay there possible and enjoyable.

Dr. Oscar Casas was especially generous in taking time to help me prepare the experimental setup for the 47th ESA's Parabolic Flight Campaign. Without their valuable contribution, it would not have been possible to have the experiment available in time.

The working environment at the Microgravity Laboratory at UPC has been made pleasant by Mr. Oscar Maldonado and Dr. Francesc Suñol. Their help in the daily tasks is gratefully acknowledged. Their friendship and professional collaboration meant a great deal to me.

I would particularly like to thank Mr. Blake Johnson for all of his help with the grammatical correction of this manuscript, as well as for his friendship and all of our conversations.

To all of the individuals above and to several colleagues, whose names I cannot continue listing and who have assisted me in one way or another, I feel very much indebted.

Above all, I owe immeasurable thanks to my family. To my parents, Teresa and Alfonso. To my grandmother Antonia. A special memory to my grandfather Silvestre. To my siblings, Alfonso, Jose Antonio, María Teresa and Rocío, and my sister and brother-in-law, Eloisa and Sergio. Last, but not the least, to the true king and queen of the family, Alfonso and María. All of them, with their constant love, are the true reason that this thesis has been possible. All my love and heartfelt thanks go to them.

This work has been financially supported by the Spanish *Ministerio de Ciencia e Innovación* (Project number AYA2009-11493) and the *Ministerio de Educación y Ciencia* (Projects number ESP2006-28459-E, FIS2006-03525, FIS2006-11452-C03-02, ESP2007-30637-E, FIS2009-13360-C03-03). Finally, I also acknowledge the financial support from the Spanish *Ministerio de Educación* (Mobility Grant for Doctoral Students).

Santiago Arias
Barcelona, July 2011

Contents

List of Figures

List of Tables

List of Symbols

Roman Symbols

A	Annular flow
A	Cross-sectional area
A_G	Area occupied by gas
A_L	Area occupied by liquid
a	Initial slope
$\bar{a}$	Normalized initial slope
B	Bubble flow
C	Churn flow
C_0	Void fraction distribution coefficient
FP	Flow pattern
F_c	Capillary forces
F_D	Liquid drag
f	Bubble generation frequency
f_{sat}	Saturation frequency
G	Mass flux
g	Gravitational acceleration
L	Characteristic length
L_B	Bubble length
L_L	Minimum liquid slug length
L_{LS}	Liquid slug length
L_{UC}	Unit cell length
$\bar{L}_B$	Normalized bubble length
$\bar{L}_L$	Normalized minimum liquid slug length

$\bar{L}_{LS}$	Normalized liquid slug length
$\bar{L}_{UC}$	Normalized unit cell length
$\dot{m}$	Overall mass flow rate
$\dot{m}_G$	Gas mass flow rate
$\dot{m}_L$	Liquid mass flow rate
Q	Volumetric flow rate
Q_G	Gas flow rate
Q_L	Liquid flow rate
R	Radius of a circular tube
r	Radial distance
S	Slug flow
t	Time
U_c	Local velocity at the centerline
U_G	Gas true average velocity
U_L	Liquid true average velocity
U_M	Superficial mixture velocity
U_{DG}	Gas drift velocity
U_{DL}	Liquid drift velocity
U_{SG0}	Crossover point
U_{SG}	Superficial gas velocity
U_{SL}	Superficial liquid velocity
$U_L{}^*$	Effective liquid velocity
$\bar{U}_G$	Weighted mean gas velocity
$\bar{U}_{DG}$	Weighted mean gas drift velocity
$\bar{U}_{DL}$	Weighted mean liquid drift velocity
V	Characteristic velocity
V_B	Bubble volume
V_L	Liquid slug volume
x	Vapor quality
x, y, z	Cartesian coordinates

Greek Symbols

α	Mean void fraction
α_B	Bubble cross-sectional void fraction
α_C	Critical void fraction
α_c	Local void fraction at the tube centerline
α_H	Homogeneous void fraction
α_w	Local void fraction at the tube wall
β	Volumetric gas quality
γ	Geometric factor
$\Delta\rho$	Difference in density of the two phases
δWe^c	Critical Weber number dispersion
δ	Liquid layer thickness
ϵ	Scale of the crossover
ϕ	Diameter of a circular channel
ϕ_B	Equivalent bubble diameter
$\bar{\phi}_B$	Normalized equivalent bubble diameter
$\delta\phi_B$	Bubble size dispersion
ϕ_c	Diameter of a circular capillary channel
μ_G	Gas dynamic viscosity
μ_L	Liquid dynamic viscosity
ρ_G	Gas density
ρ_L	Liquid density
σ	Surface tension

Dimensionless number

Bo	Bond number
Ca	Capillary number
Ca_M	Capillary number based on the superficial mixture velocity
Ca_{SL}	Capillary number based on the superficial liquid velocity
Eo	Eötvös number
Fr	Froude number
Fr_M	Froude number based on the superficial mixture velocity
Re	Reynolds number

Re_B	Bubble Reynolds number
Re_G	Reynolds number based on the gas true average velocity
Re_L	Reynolds number based on the liquid true average velocity
Re_M	Reynolds number based on the superficial mixture velocity
Re_{SG}	Reynolds number based on the superficial gas velocity
Re_{SL}	Reynolds number based on the superficial liquid velocity
St	Strouhal number
Su	Suratman number
We	Weber number
We^c	Critical Weber number
We^*	Effective Weber number
We_G	Weber number based on the gas true average velocity
We_{SG}	Weber number based on the superficial gas velocity
We_{SL}	Weber number based on the superficial liquid velocity

Subscripts

B	Bubble
c	Capillary
G	Gas
L	Liquid
LS	Liquid slug
sat	Saturation
SG	Superficial Gas
$SG0$	Superficial Gas at the crossover point
SL	Superficial Liquid

CHAPTER 1

Introduction

1.1 Motivations

In recent years, multiphase flows in microgravity conditions have become a dynamic area of research since this environment provides an excellent instrument to study flows without the masking effects of gravity. Concretely, a growing interest in the study of gas-liquid flows has arisen as a consequence of their promising technological applications in space, such as propulsion systems [61], life support systems [40], thermal management systems [39], as well as power generation and storage systems [54]. Replacing the widely used single-phase for two-phase systems could lead to an improvement in performance as well as to significant reductions in weight. As a consequence, there is a strong demand for fundamental knowledge of two-phase flows in a variety of devices and in particular in minichannels.

Bubbles or drops can be dispersed into a different phase in order to favor either energy or mass exchange. In this context, it may be necessary to maximize the contact area between both phases, which implies the generation of large numbers of small bubbles or drops, with sizes which ideally should be subject to control. A good understanding of the behavior of the gas-liquid interfaces is the cornerstone of any new technologies using two-phase flows [58, 68, 69].

Bubble generation in low-gravity environments is a key issue which requires accurate control. This requires a good knowledge of interface geometry and a regular generation of bubbles with the smallest as possible size dispersion. In

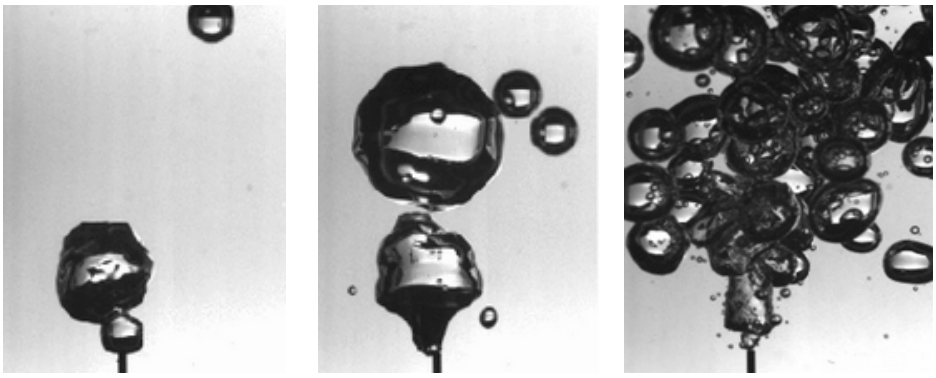

Figure 1.1: Bubble formation under microgravity conditions when increasing the gas injection (from left to right) [14].

addition, bubble dynamics is also expected to be different in the absence of buoyancy.

Concerning bubble generation, buoyancy alone is usually enough on Earth to produce detachment of bubbles [45, 71]. However, in microgravity environments this is not the case. Fig. 1.1 [14] shows the generation of bubbles by using a capillary immersed in quiescent liquid under microgravity conditions. These figures show how uncontrolled and large the bubble size dispersion is in the absence of the buoyancy force. The microgravity environment thus makes necessary specific configurations in order to detach bubbles from the generator device in a control way.

Different methods have been envisaged to produce bubble detachment in the microgravity environment [53, 86, 87]. Typical methods used are the co-flow configuration [7] (see Fig. 1.2-a), in which liquid flows parallel to the gas injection direction, cross-flow configuration [30] (see Fig. 1.2-b), in which liquid flows perpendicularly to the gas, combinations of these two previous methods such as the flow-focusing method [35, 67], the application of electric fields [41, 57], etc. Performance of these methods was not completely satisfactory for certain purposes, bubble sizes being typically too large, with large size dispersion, and the methods being sensitive to the gravity level.

Based on these previous analyses of the detachment process, a new method for generating small bubbles was recently proposed [15] and tested [2, 3], which addressed these issues with significant improvement. In this thesis, we focus on the analysis of the formation of a train of bubbles by means of the cross-flow

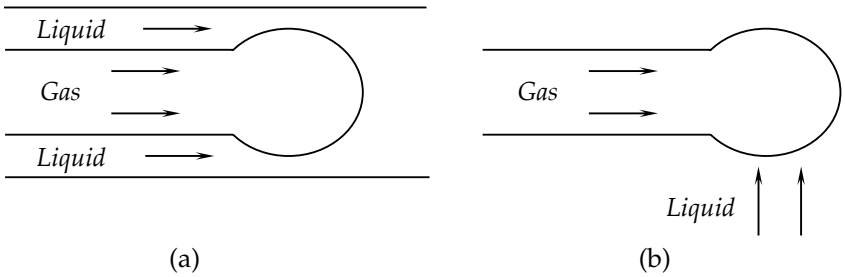

Figure 1.2: Sketch of the *a*) co-flow, and *b*) cross-flow configurations.

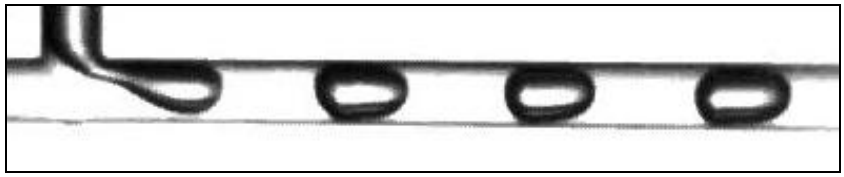

Figure 1.3: Detail of the bubble generator. Gas is injected from the top and liquid from the left side. Gravity is in the vertical direction.

generated in a capillary T-shaped junction [32, 34]. In this bubble generator, gas is injected from a capillary into another capillary in a perpendicular direction in which liquid is flowing (see Fig. 1.3). We consider here the simplest case, in which both capillaries have the same circular cross-section of 1 mm i.d. Bubbles are generated as a result of the competition between the involved forces in the capillary T-junction, the capillary forces being predominant over inertia (small Weber number) and buoyancy (small Bond number) in the regimes studied here. Bubble formation thus results from the competition between capillary forces and the drag due to the liquid cross-flow. The resulting bubbles can range in size from small size (of the order of the employed capillaries) up to several diameter lengths, with very small size dispersion, being insensitive to gravity level.

The key point of this method is that one does not generate only air but a train of bubbles, that is, a controlled mixture of gas and liquid. A periodic train of bubbles is thus already formed before the actual injection, and the inertia of the injected flow is used in turn to spread the bubbles to form a jet if required. Note that since the walls are completely wet by the liquid, capillary forces have no action against detachment of the bubbles from the injection tube into a cavity or any container of the injection, contrary to other injection configurations. Indeed, for this bubble generator the relevant processes controlling bubble formation are the same as those generating the two-phase flow at the T-junction.

We present in this manuscript a study of the flows obtained with the bubble generator, exploring different operating regimes. We focus on a range of gas and liquid flow rates which gives rise to bubble and slug flow regimes. The characterization of the bubble generation consists in the analysis of bubble velocity and void fraction, bubble generation frequency, unit cell, bubble and liquid slug lengths in the observed flow regimes. We propose expressions obtained empirically for the behavior of the bubble generation frequency as well as theoretical predictions for the bubble velocity, characteristic lengths, and the average void fraction distribution.

1.2 Objectives

Based on previous analysis of the bubble detachment process, this work analyzes the generation and characterization of two-phase (gas and liquid) flows with the T-junction method [2, 3]. The major goals are:

- Provide a new flow pattern map, paying special attention to the bubble-slug transition.
- Study the bubble dynamics by analyzing their velocity and the mean void fraction distribution.
- Analyze the bubble generation process by focusing in the generation frequency.
- Characterization of the two-phase flows by analyzing the geometry of the unit cell, bubble and liquid slug.
- Validate the use of a numerical code for the generation of two-phase flows by means of the comparison of numerical simulation results with those from experiments.

1.3 Manuscript outline

To such an end, this manuscript is organized as follow:

- Chapter 1: introduction.
- Chapter 2: presents the fundamental definitions in two-phase flow and the nomenclature used in this work.

- Chapter 3: reviews the state of the art in the topics addressed in this thesis: the flow pattern maps and transitions between regimes, bubble velocity and void fraction distribution, bubble generation process in the capillary dominated regime. Finally, previous numerical works are also presented.
- Chapter 4: presents the experimental setup used in this work, as well as a description of the experiments and the image processing protocol designed to obtain the data.
- Chapter 5: shows the experimental results regarding the bubble velocity and the mean void fraction according to the drift-flux model. A new flow pattern map is also presented. A criteria regarding the bubble-slug transition is discussed.
- Chapter 6: analyzes the bubble generation frequency. A new expression for the non-dimensional generation frequency, based upon the Strouhal number is also provided.
- Chapter 7: presents the experimental results in bubble, unit cell and slug liquid lengths.
- Chapter 8: offers a comparison between the experimental results and a numerical simulation on the bubble generation in the T-junction.
- Chapter 9: outlines the conclusions of this work as well as suggests possible research for the future.

CHAPTER 2

Fundamental definitions and nomenclature

In this chapter we present a brief review of some fundamental definitions and nomenclature in two-phase flows, which will be used throughout this manuscript.

2.1 Two-phase flow in microgravity

In fluid mechanics, two-phase flow is defined as a mixture flow containing two different phases separated by an interface. This is indeed a particular case of multiphase flow. The mixture could be generated by different phases of a single fluid or, in a more general case, be composed of two different fluids. A case of special interest is the situation in which gas and liquid are mixed. Under these circumstances, the ratio between both phases' densities usually differs by several orders of magnitude.

Several patterns can be found in two-phase flows. At a basic level, they can be classified in two main groups: continuous or intermittent flows, the former being spatially homogeneous whereas the latter are not.

The term microgravity (often referred to as μg) indicates that apparent experienced gravitational forces are low, but different than zero. Microgravity differs from weightlessness in that point. Accelerations in such an environment typically range from 10^{-6} up to 0.1 g.

The study of two-phase flows in microgravity-related conditions concerns the analysis of these flows in different conditions than those provided by an influential gravitational environment. A direct consequence is that two-phase flows in a microgravity environment can reveal behaviors that otherwise would be masked by the effects of gravity.

2.2 Mass flux and vapor quality

In a channel through which a gas-liquid mixture flows, each phase contributes with a mass flow rate of $\dot{m}_G$ and $\dot{m}_L$ (with dimensions of $[M/T]$), respectively. Therefore, the overall mass flow rate can be calculated as the sum of both contributions:

$$\dot{m} = \dot{m}_G + \dot{m}_L \tag{2.1}$$

An alternate way to express the mass flow rate is as a mass flux G (with dimensions of $[M/L^2\,T]$), that is, dividing $\dot{m}$ by the cross-sectional area of the channel, A (with dimensions of $[L^2]$):

$$G = \frac{\dot{m}}{A} \tag{2.2}$$

In circular channels, the diameter ϕ is usually used as a characteristic length, which commonly is referred to as ϕ_c when working with capillaries. The cross-sectional area can then be written as $A = \pi\,{\phi_c}^2/4$.

The vapor quality is defined as the ratio of the gas mass flow rate to the total mass flow rate:

$$x = \frac{\dot{m}_G}{\dot{m}} \tag{2.3}$$

In an adiabatic system with no phase change, the vapor quality can be calculated merely by knowing the vapor quality at the inlet.

2.3 Volume flow rates

The gas and liquid volume flow rates (with dimensions of $[L^3/T]$) are given by, respectively:

$$Q_G = \frac{\dot{m}_G}{\rho_G} \tag{2.4}$$

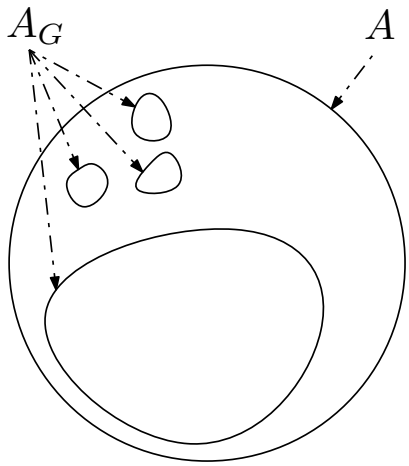

Figure 2.1: Sketch of the cross-section of a circular channel partially occupied by gas.

$$Q_L = \frac{\dot{m}_L}{\rho_L} \tag{2.5}$$

where ρ_G and ρ_L are the gas and liquid densities (with dimensions of $[\, M/L^3]$).

2.4 Void fraction

The cross-sectional void fraction α is the ratio of the area occupied by the gas to the total cross-sectional area (see Fig. 2.1). The void fraction is expressed locally at a cross-section of the channel by means of Eqs. 2.6 and 2.7.

$$\alpha = \frac{A_G}{A_G + A_L} = \frac{A_G}{A} \tag{2.6}$$

$$1 - \alpha = \frac{A_L}{A_G + A_L} = \frac{A_L}{A} \tag{2.7}$$

where A_G and A_L are the area occupied by gas and liquid, respectively.

On the other hand, a volume averaged void fraction, which is the ratio of the gas volume to the total volume, can also be defined. For intermittent flows the void fraction is averaged along the part of the channel occupied by the gas and the liquid slug, and is then called the averaged or mean void fraction. Finally, in view of the fact that the volume flow rates are inlet readily available data, the

ratio between the gas and liquid flow rate is frequently used as a pseudo void fraction.

2.5 Velocities

There are a large number of velocities that can be defined in two-phase flows. Generally, gas and liquid velocities are different, as a consequence of the existence of a relative velocity between them.

2.5.1 Gas/liquid and mixture superficial velocities

The superficial velocity (with dimensions of $[L/T]$) is the velocity that each phase would have under the assumption that gas/liquid mass alone were flowing through the channel:

$$U_{SG} = \frac{Q_G}{A} = \frac{G}{\rho_G}\, x \tag{2.8}$$

$$U_{SL} = \frac{Q_L}{A} = \frac{G}{\rho_L}\,(1-x) \tag{2.9}$$

The mixture superficial velocity can thus be defined as the sum of the gas and liquid superficial velocities:

$$U_M = U_{SG} + U_{SL} \tag{2.10}$$

2.5.2 True average velocities

The true velocity of each phase (with dimensions of $[L/T]$) is assumed to be greater than its respective superficial velocity, due to the smaller true cross-section area occupied by the phases. This velocity is an average across the cross-section, and can be estimated as:

$$U_G = \frac{Q_G}{A_G} = \frac{Q_G}{\alpha\, A} = \frac{U_{SG}}{\alpha} \tag{2.11}$$

$$U_L = \frac{Q_L}{A_L} = \frac{Q_L}{(1-\alpha)\, A} = \frac{U_{SL}}{1-\alpha} \tag{2.12}$$

The true averaged velocities can be rearranged in terms of x, α, $\dot{m}$ and G:

$$U_G = \frac{x}{\alpha}\frac{\dot{m}}{\rho_G\, A} = \frac{x}{\alpha}\frac{G}{\rho_G} \tag{2.13}$$

$$U_L = \frac{1-x}{1-\alpha}\frac{\dot{m}}{\rho_L A} = \frac{1-x}{1-\alpha}\frac{G}{\rho_L} \tag{2.14}$$

With the previous expressions, $\dot{m}_G$ and $\dot{m}_L$ can also be expressed in terms of their respective true velocities as follows:

$$\dot{m}_G = \rho_G U_G A_G = \rho_G U_G \alpha A \tag{2.15}$$

$$\dot{m}_L = \rho_L U_L A_L = \rho_L U_L (1-\alpha) A \tag{2.16}$$

2.5.3 Drift velocities

Gas and liquid drift velocities (with dimensions of $[L/T]$) are defined as the relative velocity of each phase and the mixture superficial velocity:

$$U_{DG} = U_G - U_M \tag{2.17}$$

$$U_{DL} = U_L - U_M \tag{2.18}$$

2.6 Volumetric gas quality

The volumetric gas quality is the ratio of the gas and the total volume flow rates:

$$\beta = \frac{Q_G}{Q_G + Q_L} \tag{2.19}$$

which can also be rewritten in terms of the superficial velocities by means of Eqs. 2.8 and 2.9

$$\beta = \frac{U_{SG}}{U_{SG} + U_{SG}} \tag{2.20}$$

β is also known as the homogeneous void fraction, α_H, due to the fact that it is equal to the averaged void fraction for a homogeneous flow, in which both phases move with the same velocity and thus no slip velocity exists between them.

2.7 Dimensionless groups

2.7.1 Bond number

The Bond number, Bo, which is also known as Eötvös number, Eo, is defined as:

$$Bo = \frac{\Delta\rho\, g\, L^2}{\sigma} = \frac{buoyancy\ \ forces}{surface\ \ forces} \tag{2.21}$$

where $\Delta\rho$ is the difference in density of the two phases $[kg/m^3]$, g is the gravitational acceleration $[m/s^2]$, L is the characteristic length $[m]$, and σ the surface tension at the interface formed by both phases $[N/m]$. Bo represents the balance between the gravitational and surface tension forces, becoming one of the relevant dimensionless group to determine if the two-phase flow is conditions relevant for a microgravity environment.

In a gas-liquid mixture inside circular capillaries, ϕ_c is usually used as the characteristic length, and Bo is commonly stated as:

$$Bo = \frac{(\rho_L - \rho_G)\, g\, {\phi_c}^2}{\sigma} \tag{2.22}$$

2.7.2 Weber number

The Weber number, We, is defined as:

$$We = \frac{\rho\, V^2\, L}{\sigma} = \frac{inertial\ \ forces}{surface\ \ forces} \tag{2.23}$$

with V being the characteristic velocity of the flow $[m/s]$. In microgravity conditions, where buoyancy forces are neglected, We becomes an important correlating parameter, representing the balance between inertial and surface tension forces.

Depending on the selected characteristic velocity, We can be defined in several ways for circular capillaries. When using the superficial velocities, the superficial We numbers can be expressed in the following forms:

$$We_{SG} = \frac{\rho_G\, U_{SG}^2\, \phi_c}{\sigma} \tag{2.24}$$

$$We_{SL} = \frac{\rho_L\, U_{SL}^2\, \phi_c}{\sigma} \tag{2.25}$$

When working with two-phase flows where the gas inertia is much smaller than liquid inertia, the former can be neglected and ρ_G is often replaced by ρ_L in Eq. 2.24.

In the case that the gas true average velocity is known, the *We* number is usually defined as:

$$We_G = \frac{\rho_L \, {U_G}^2 \, \phi_c}{\sigma} \tag{2.26}$$

2.7.3 Reynolds number

The Reynolds number, *Re*, is defined as:

$$Re = \frac{\rho \, V \, L}{\mu} = \frac{inertial \;\; forces}{viscous \;\; forces} \tag{2.27}$$

where μ is the dynamic viscosity $[kg/m\,s]$. *Re* represents the ratio between the inertial and the viscous forces, thus defining when the flow is laminar or turbulent.

Analogously to *We*, *Re* can be defined in different ways depending on the characteristic velocity used. When using the superficial velocities:

$$Re_{SG} = \frac{\rho_G \, U_{SG} \, \phi_c}{\mu_G} \tag{2.28}$$

$$Re_{SL} = \frac{\rho_L \, U_{SL} \, \phi_c}{\mu_L} \tag{2.29}$$

where μ_G and μ_L are the gas and liquid dynamics viscosities, respectively. Additionally, *Re* can be defined in terms of the true velocities when U_G and U_L is known:

$$Re_G = \frac{\rho_G \, U_G \, \phi_c}{\mu_G} \tag{2.30}$$

$$Re_L = \frac{\rho_L \, U_L \, \phi_c}{\mu_L} \tag{2.31}$$

Finally, *Re* number is also commonly used in terms of the mixture superficial velocity through the liquid physical properties:

$$Re_M = \frac{\rho_L \, U_M \, \phi_c}{\mu_L} \tag{2.32}$$

2.7.4 Strouhal number

The Strouhal number, St, is defined as:

$$St = \frac{f\,L}{V} \tag{2.33}$$

where f $[1/s]$ is the characteristic frequency that describes a given physical phenomenon. St then describes oscillating flow mechanisms. When using St to describe the phenomenon of the generation of bubbles in a capillary, it is worthy to define St in terms of the gas true average velocity:

$$St = \frac{f\,\phi_c}{U_G} \tag{2.34}$$

being f in this situation the bubble generation frequency.

2.7.5 Froude number

The Froude number, Fr, is defined as:

$$Fr = \sqrt{\frac{We}{Bo}} = \frac{V}{\sqrt{g\,L}} = \sqrt{\frac{inertial\ \ forces}{buoyancy\ \ forces}} \tag{2.35}$$

Fr is used to compare the body's inertia to the gravitational forces. Depending on the combination of We and Bo used, it is possible to define a number of different Fr, but it is commonly used in terms of the mixture velocity:

$$Fr_M = \sqrt{\frac{We_M}{Bo_M}} = \frac{U_M}{\sqrt{g\,\phi_c}} \tag{2.36}$$

2.7.6 Capillary number

The Capillary number, Ca, is defined as:

$$Ca = \frac{We}{Re} = \frac{\mu\,V}{\sigma} = \frac{viscous\ \ forces}{surface\ \ forces} \tag{2.37}$$

Ca is used to compare viscosity and surface tension effects at the interface. Depending on the combination of We and Re used, it is possible to define a number of different Ca, but it is commonly used in terms of the liquid superficial or the mixture velocities, respectively:

$$Ca_{SL} = \frac{We_{SL}}{Re_{SL}} = \frac{\mu_L\,U_{SL}}{\sigma} \tag{2.38}$$

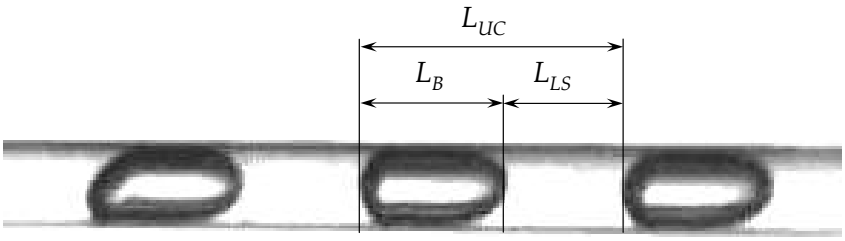

Figure 2.2: Example of an intermittent two-phase flow formed by a train of bubbles. The unit cell is pointed out by means of L_B, L_{LS} and L_{UC}.

$$Ca_M = \frac{We_M}{Re_M} = \frac{\mu_L U_M}{\sigma} \tag{2.39}$$

2.7.7 Suratman number

The Suratman number, Su, also known as the Laplace number, La, is defined as:

$$Su = \frac{Re^2}{We} = \frac{\rho \sigma L}{\mu^2} \tag{2.40}$$

Su number represents the ratio of surface tension to the momentum-transport inside a flow and is a dimensionless group commonly used for describing the phenomenon of coalescence. Analogous to the previous dimensionless numbers, Su can be defined in different ways but it is often used in terms of the liquid's physical properties:

$$Su = \frac{{Re_{SL}}^2}{We_{SL}} = \frac{\rho_L \sigma \phi_c}{{\mu_L}^2} \tag{2.41}$$

2.8 Unit cell

In most of the cases, intermittent two-phase flows follow a complex structure in which a high dispersion in bubbles size appears even when conditions at the inlets remain constant. By reducing intermittence to periodicity, the structure can be analyzed by an equivalent unit cell [23, 26, 28, 89]. A simpler situation arises when bubbles are generated with regularity and a negligible size dispersion exists. In any case, the existence of an elementary part of the flow, the unit cell, can be assumed.

The unit cell consists of a bubble and a liquid slug (see Fig. 2.2). Their

respective lengths can be written as L_B and L_{LS}. The total unit cell length, $L_{UC} = L_B + L_{LS}$, can thus be defined as the distance between the tips of two consecutive bubbles.

CHAPTER 3

State of the art

In this chapter we present a brief review of the state of the art in some topics in two-phase flows. Section 3.1 presents predictions on gas velocity and void fraction, focusing on the general drift-flux model. Section 3.2 analyzes several flow pattern maps available in the literature. Special attention is paid to the bubble-slug transition. Section 3.3 focuses on the capillary dominated regime and its particular role in the generation of bubbles. Finally, Section 3.4 summarizes several numerical results of research that attempted to analyze the formation and generation of bubbles.

3.1 Bubble velocity and void fraction models

3.1.1 The homogeneous model

The homogeneous model is based upon the assumption that both phases, gas and liquid, travel at the same true average velocity. By matching Eqs. 2.13 and 2.14, one can obtain the following expression for the homogeneous void fraction:

$$\alpha_H = \left(1 + \left(\frac{1-x}{x}\frac{\rho_G}{\rho_L}\right)\right)^{-1} \tag{3.1}$$

By taking into account Eqs. 2.8 and 2.11, the gas true velocity can be calculated as:

$$U_G = G\left(\frac{x}{\rho_G} + \frac{1-x}{\rho_L}\right) = U_{SG} + U_{SL} \tag{3.2}$$

This model is only reasonably accurate when a dispersed phase travels at nearly the same velocity as the continuous phase, such as in some bubble flows or in the case of droplets dispersed into a flowing gas. Otherwise, gas phase usually travels at higher velocities than liquid phase when flowing in vertical upward and horizontal channels. Therefore, the homogeneous model underpredicts the true average bubble velocity while overpredicting the void fraction. Under those circumstances, a more accurate model is required.

3.1.2 The drift-flux model

The drift-flux model was presented by Zuber and Findlay [93] and it was subsequently developed mainly by Wallis [89] and Ishii [42]. This model is applicable to any two-phase flow and in contrast to previously existing models, it takes into account the radial profile of both the nonuniform flow velocity and the void fraction over the channel cross-section.

Zuber and Findlay derive the model in terms of cross-sectional quantities, being more effective when the flows are axisymmetric, such as gas flowing in vertical tubes or in microgravity conditions. To this end, they define a mean value of any function across the cross-section as:

$$\langle F \rangle = \frac{1}{A} \int_A F \, dA \tag{3.3}$$

where F is a local quantity varying in the radial position and A is the cross-sectional area. In order to calculate the mean value of U_G, the authors use the definition of gas drift velocity provided by Eq. 2.17, obtaining:

$$\langle U_G \rangle = \langle U_M \rangle + \langle U_{DG} \rangle \tag{3.4}$$

Of available data, superficial velocities are often measured with less effort than true average velocities. Considering this fact, Zuber and Findlay introduce the concept of the weighted mean value of a quantity F into the analysis, which is defined as:

$$\bar{F} = \frac{\langle \alpha \, F \rangle}{\langle \alpha \rangle} = \frac{\frac{1}{A} \int_A \alpha \, F \, dA}{\frac{1}{A} \int_A \alpha \, dA} \tag{3.5}$$

The weighted mean gas velocity is then calculated as:

$$\bar{U}_G = \frac{\langle \alpha \, U_G \rangle}{\langle \alpha \rangle} = \frac{\langle U_{SG} \rangle}{\langle \alpha \rangle} = \frac{Q_G \, / \, A}{\langle \alpha \rangle} \tag{3.6}$$

where $\langle \alpha \rangle$ is the average void fraction. By calculating the weighted mean

values of the gas, the mixture and the gas drift velocities, the authors rewrite Eq. 2.17 as:

$$\bar{U}_G = \bar{U}_M + \bar{U}_{DG} = \frac{\langle \alpha\, U_M \rangle}{\langle \alpha \rangle} + \frac{\langle \alpha\, U_{DG} \rangle}{\langle \alpha \rangle} \tag{3.7}$$

Then, by multiplying and dividing the first term of the right-hand side of the equation by $\langle U_M \rangle$, they obtain:

$$\bar{U}_G = \frac{\langle U_{SG} \rangle}{\langle \alpha \rangle} = C_0 \langle U_M \rangle + \frac{\langle \alpha\, U_{DG} \rangle}{\langle \alpha \rangle} = C_0 \langle U_M \rangle + \bar{U}_{DG} \tag{3.8}$$

where C_0, which is known as void fraction distribution coefficient, is defined as:

$$C_0 = \frac{\langle \alpha U_M \rangle}{\langle \alpha \rangle \langle U_M \rangle} = \frac{\frac{1}{A}\int_A \alpha\, U_M\, dA}{\left(\frac{1}{A}\int_A \alpha\, dA\right)\left(\frac{1}{A}\int_A U_M\, dA\right)} \tag{3.9}$$

Therefore, the drift-flux model takes into account both the effects caused by a non-uniform velocity and local void fraction profiles as well as the existence of local relative velocity through C_0 and $\bar{U}_{DG}$, respectively. Eq. 3.8 can be expressed in a dimensionless way by dividing both sides of the equation by $\langle U_M \rangle$

$$\frac{\langle U_{SG} \rangle}{\langle \alpha \rangle \langle U_M \rangle} = \frac{\langle \beta \rangle}{\langle \alpha \rangle} = C_0 + \frac{\langle \alpha\, U_{DG} \rangle}{\langle \alpha \rangle \langle U_M \rangle} \tag{3.10}$$

The drift-flux model becomes useful when working with experimental data. Zuber and Findlay reported that bubble, slug and annular flows displayed a linear dependency when data were plotted in $\bar{U}_G - \langle U_M \rangle$ coordinates. A simple linear regression provides the values of C_0 and the weighted mean velocity $\bar{U}_{DG}$, where the former is equal to the slope of the line and the latter the intercept of it with the $\bar{U}_G$ axis.

Zuber and Findlay proposed expressions for the weighted gas drift velocity for vertical flows, where $\bar{U}_{DG}$ was equated to the terminal velocity of a particle rising in a medium in the presence of buoyancy forces. For the bubble flow, it is expressed as:

$$\frac{\langle \alpha\, U_{DG} \rangle}{\langle \alpha \rangle} = 1.53 \left(\frac{\sigma\, g\, \delta\rho}{{\rho_L}^2} \right)^{\frac{1}{4}} \tag{3.11}$$

and for the slug flow as:

$$\frac{\langle \alpha\, U_{DG} \rangle}{\langle \alpha \rangle} = 0.35 \left(\frac{g\, \delta\rho\, \phi}{\rho_L} \right)^{\frac{1}{2}} \tag{3.12}$$

Other authors such as Wallis [89], Ishii [42], Fernandes [27], Bendiksen [6] and Andreussi *et al.* [1] have also reported empirical correlations of C_0 and $\bar{U}_{DG}$ for vertical, horizontal and inclined tubes. All correlations were proposed for each specific flow pattern, such as bubble, slug and annular flows. Therefore, there is no continuity when passing from one flow pattern to another.

Regarding horizontal channels, several authors such as Gregory and Scott [37] as well as Dukler and Hubbard [23] claim that the drift flux velocity is zero. Furthermore, in microgravity environments or in capillaries, the buoyancy effect becomes neglected as well as $\bar{U}_{DG}$, as shown by the experimental results of Bousman [10] and Dukler *et al.* [22]. In view of these circumstances, Eq. 3.10 becomes

$$\frac{\langle \beta \rangle}{\langle \alpha \rangle} = C_0 \tag{3.13}$$

Note that when $C_0 = 1$ the homogeneous model is recovered:

$$\langle \beta \rangle = \langle \alpha \rangle = \alpha_H \tag{3.14}$$

3.1.3 Void fraction distribution coefficient

3.1.3.1 Dependence with the local velocity and void fraction

Zuber and Findlay [93] developed a theoretical model of C_0, which supposes a good theoretical guide although it does not provide any insight of the physical mechanisms involved in the flow. They assumed both distributions of local velocity and void fraction to be axisymmetric across the cross-section following a potential behavior, as shown by Eqs. 3.15 and 3.16. Therefore, this analysis is only reliable for axisymmetric flows, such as two-phase flows in microgravity.

$$\frac{U}{U_c} = 1 - \left(\frac{r}{R}\right)^m \tag{3.15}$$

$$\frac{\alpha - \alpha_w}{\alpha_c - \alpha_w} = 1 - \left(\frac{r}{R}\right)^n \tag{3.16}$$

In the previous equations, U refers to the local velocity at the radial distance r, R to the tube radius, and the subscripts w and c to the walls and centerline of the channel, respectively. By including the local profiles of Eqs. 3.15 and 3.16 in Eq. 3.9, the authors derive an expression of C_0 in terms of m and n:

$$C_0 = \frac{m+2}{m+n+2}\left(1 + \left(\frac{n}{m+2}\right)\left(\frac{n+2}{n+2\left(\frac{\alpha_w}{\alpha_c}\right)}\right)\right) \tag{3.17}$$

Case 1	Case 2	Case 3
$\alpha_c < \alpha_w$	$\alpha_c = \alpha_w$	$\alpha_c > \alpha_w$
$C_0 < 1$	$C_0 = 1$	$C_0 > 1$

Table 3.1: The effect of α_c and α_w on C_0 [33].

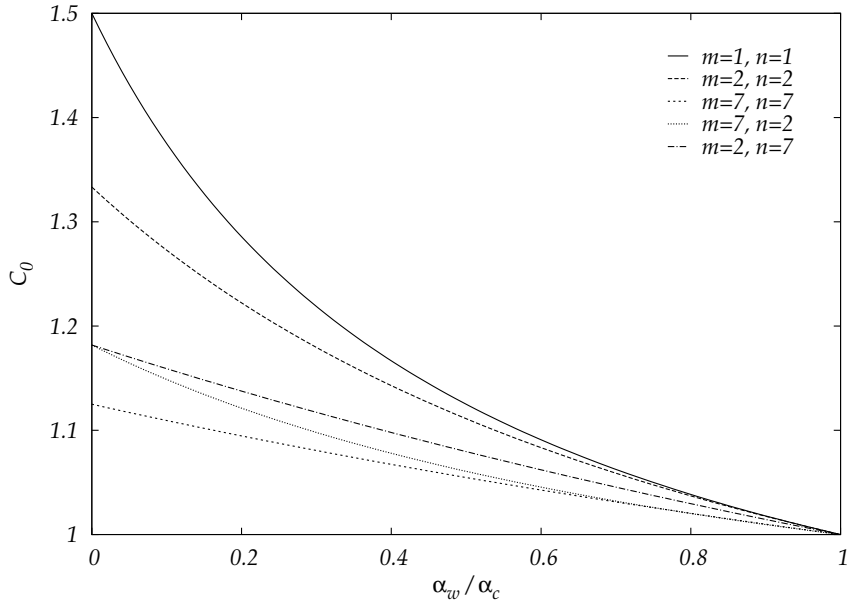

Figure 3.1: Prediction of C_0 in terms of the ratio α_w / α_c (Eq. 3.17) [10].

Fig. 3.1 shows the computed C_0 for several values of m and n. Moderate gradients in velocity and void fraction are obtained when increasing m and n, while both profiles become flatter. For a value of m and n equal to 7, an almost flat profile is acquired. Depending on the local void fraction distribution, C_0 can be greater, equal to or less than 1. The first case occurs when gas concentrates at the centerline, and then $\alpha_c > \alpha_w$. If gas concentrates at the wall, $\alpha_c < \alpha_w$ and thus C_0 become less than 1. When the local void fraction is uniform across the section, C_0 becomes equal to 1, recovering once again the homogeneous model in absence of buoyancy forces. Table 3.1 summarizes these previous conditions.

In most cases in microgravity, there is a continuous gas-free region on the walls. Thus, the ratio α_w / α_c can generally be assumed to be zero. As a consequence, Eq. 3.17 becomes:

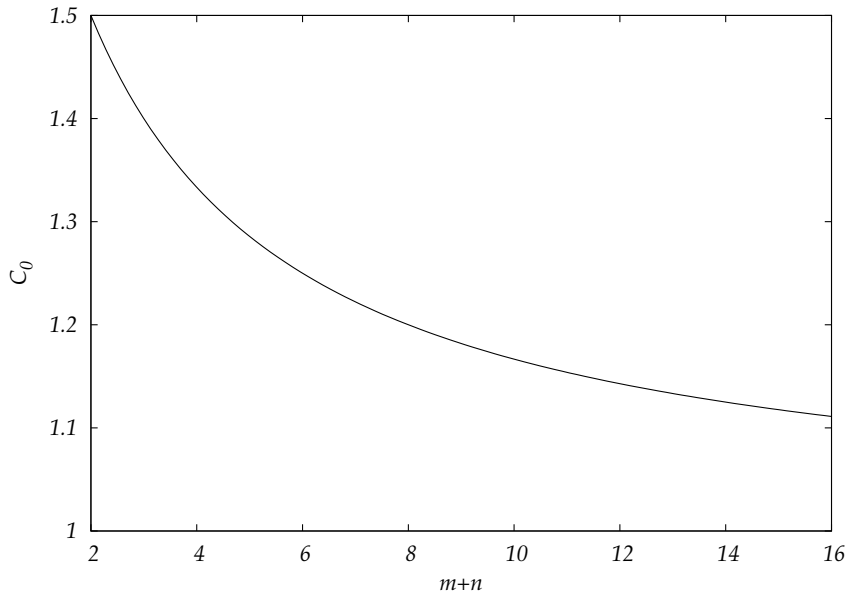

Figure 3.2: Prediction of C_0 in terms of $m + n$ for a ratio $\alpha_w / \alpha_c = 0$ (Eq. 3.18).

$$C_0 = \frac{m+n+4}{m+n+2} \tag{3.18}$$

and the range of C_0 values is expected to be approximately $1.1 < C_0 < 1.5$, as shown in Fig. 3.2.

Recently, Revellin *et al.* [76] have provided an equivalent approach focused on the liquid layer thickness, δ, of elongated bubbles. They integrate Eq. 3.9 at a given instant in time, hence assuming the local void fraction distribution across the cross-section to be a discontinuous function with a value equal to 1 or 0 if gas or liquid are found at that point, respectively. When the bubble outline in a given cross-sectional area is a circle of radio $R - \delta$ concentric with the centerline, the definition provided by Eq. 3.9 can be rewritten as:

$$C_0 = \frac{\frac{1}{A}\left(\int_{A_G} 1\, x\, U_{SG}\, dA + \int_{A_L} 0\, x\, U_{SL}\, dA\right)}{\left(\frac{R-\delta}{R}\right)^2 \frac{1}{A}\left(\int_{A_G} U_{SG} dA + \int_{A_L} U_{SL}\, dA\right)} \tag{3.19}$$

Rearranging this equation results in:

$$C_0 = \frac{\frac{A_G}{A} U_{SG}}{\frac{A_G}{A}\left(\frac{A_G}{A} U_{SG} + \frac{(A-A_G)}{A} U_{SL}\right)} \tag{3.20}$$

which leads to:

$$\frac{1}{C_0} = \left(1 + \frac{\delta\,(2R-\delta)}{R^2}\left(\frac{R}{R-\delta}\right)^2\left(\frac{U_{SL}}{U_{SG}}\right)\left(\frac{R-\delta}{R}\right)^2\right) \tag{3.21}$$

By means of Eq. 2.8 and 2.9, the ratio U_{SL}/U_{SG} can be expressed as,

$$\frac{U_{SL}}{U_{SG}} = \left(\frac{1-x}{x}\right)\frac{\rho_G}{\rho_L} \tag{3.22}$$

and taking into account the assumption of no slip velocity between phases as a consequence of neglected buoyancy forces, the authors derive an expression of the previous ratio in terms of R and δ (see Eqs. 2.13 and 2.14):

$$\left(\frac{1-x}{x}\right)\frac{\rho_G}{\rho_L} = \frac{1-\alpha}{\alpha} = \frac{A_L}{A_G} = \frac{\delta(2R-\delta)}{(R-\delta)^2} \tag{3.23}$$

with which they obtain C_0 only in terms of R and δ:

$$\frac{1}{C_0} = \left(1 - \frac{\delta}{R}\right)^2\left(1 + \frac{(\delta/R)^2(2-\delta/R)^2}{(1-\delta/R)^4}\right) \tag{3.24}$$

Eq. 3.24 is plotted in Fig. 3.3, showing C_0 increasing from 1, which correctly corresponds to δ=0.

3.1.3.2 Dependence with *Re* and *Ca*

C_0 is a dimensionless coefficient that depends on other dimensionless parameters, namely the Reynolds, Capillary and Froude numbers, and the volumetric gas quality [26]:

$$C_0 = f(Re, Ca, Fr, \beta) \tag{3.25}$$

When the buoyancy forces are neglected, the bubble motion is controlled only by the mean flow. Therefore, the Reynolds and Capillary numbers become the relevant parameters for C_0. Collins *et al.* [19] developed an inviscid flow theory, showing that C_0 is sensitive to the flow regime upstream of the bubble. They attain the next equations:

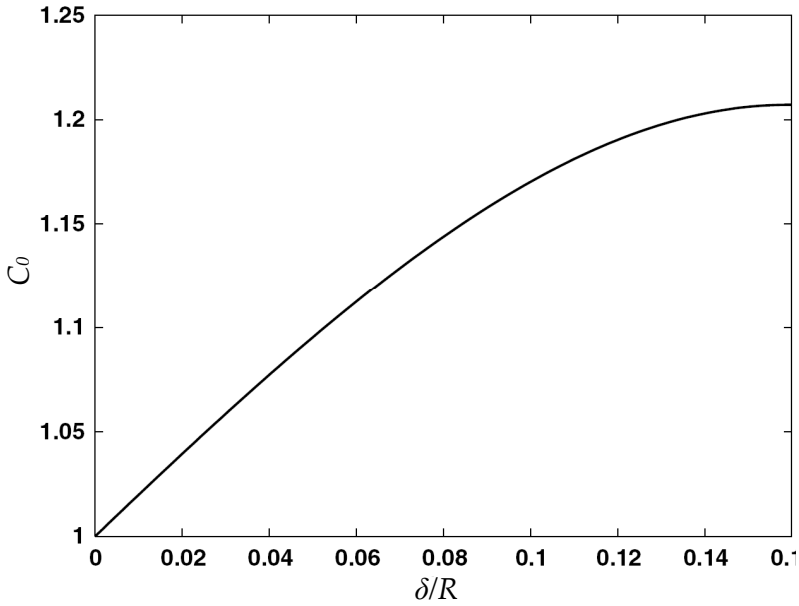

Figure 3.3: C_0 versus the ratio of the liquid layer thickness to the channel diameter radius [76].

$$C_0 = \begin{cases} 2.27 & for\ laminar\ flow \\ \dfrac{log(Re_M) + 0.089}{log(Re_M) - 0.74} & for\ turbulent\ flow \end{cases} \tag{3.26}$$

Fig. 3.4 shows the tendency of Eqs. 3.26 for both laminar and turbulent regimes. A laminar to turbulent transition must exist within the range $Re_L = 200 - 5000$, and although it has been observed under normal gravity conditions [31], further work is still required in low gravity conditions to understand it.

Different values for C_0 can be found in the literature depending on both the geometry and the effects of inertia, viscosity and surface tension. According to Nicklin *et al.* [66], the bubble velocity is close to the axis liquid velocity far upstream so that C_0 is approximately 2 for laminar pipe flow and approximately 1.2 for turbulent pipe flow, agreeing with the model of Collins *et al.*. This is confirmed by both the experiments of Colin *et al.* [18] and Bousman *et al.* [11], where C_0 is found to be close to 1.2 for turbulent pipe flow, as well as by the laminar experiments of Taylor [85] at small Reynolds number where a nearly constant value of $C_0 \sim 2.3$ is observed for Capillary number $Ca_L = \mu_L U_L/\sigma$ larger than 1.5. At the limit of both small Capillary numbers and small Reynolds numbers, the difference between bubble velocity and liquid velocity is found to

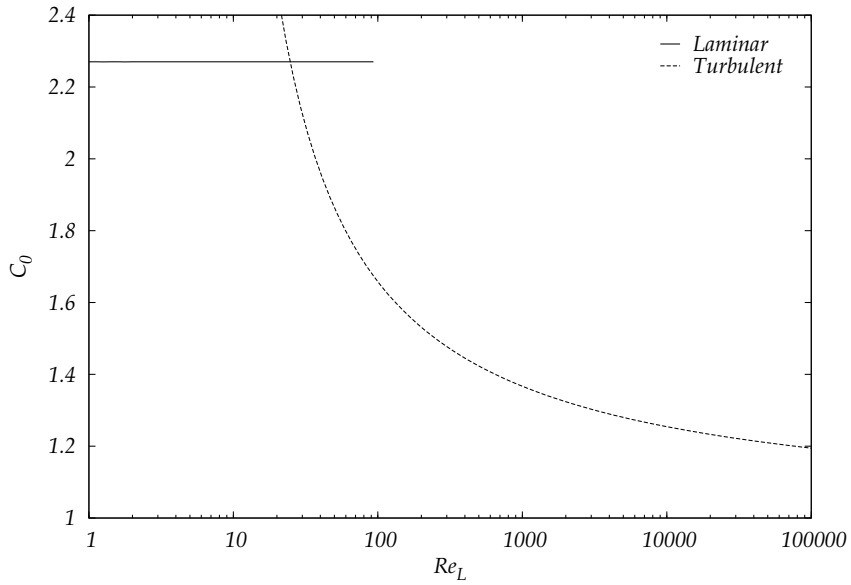

Figure 3.4: Prediction of C_0 in terms of Re_L according to the model of Collins *et al.* (Eq. 3.26).

evolve as $Ca^{2/3}$ [13] so that C_0 tends to unity as confirmed by recent experiments [4, 88].

3.2 Flow pattern maps

The distinguishing feature of two-phase flows in channels is the gas-liquid interface, which depends on some physical properties (density, viscosity, surface tension), flow rates of both fluids, gravity level and the hydraulic diameter of the channel. Even if there are many different interface topologies, two-phase flows can be classified into a limited number of flow patterns. Baker [5] plotted the first flow pattern maps in order to provide a satisfactory classification of flow patterns. Different parameters such as flow rates or superficial velocities were used as coordinates.

New questions were later addressed regarding the flow pattern boundaries, thus triggering interest in the study of flow pattern transitions. Govier and Aziz [36] summarized the early steps carried out in the 1960s, reporting the flow patterns found both in vertical and horizontal tubes as well as results in flow pattern transitions. The concepts of stratified, bubble, slug and annular flows first appeared during this decade.

Interested in the role played by gravity in two-phase pattern formation, Suo and Griffith [83] performed experimental work on air-water flow in minichannels (0.5 up to 0.7 mm internal diameter). They developed a criterion based upon the Eötvös number that determines when gravitational effects become negligible with respect to capillary effects:

$$Eo = \frac{\Delta\rho g \phi^2}{\sigma} = \frac{buoyancy\ force}{surface\ force} < 0.29 \tag{3.27}$$

According to the authors, when this criterion is accomplished, gravitational effects become masked by superficial effects, resulting in the irrelevance of the channel orientation. Under these conditions, the same flow patterns and flow pattern transitions are expected in vertical and horizontal tubes, and two-phase flows can be assumed to be under microgravity-related conditions. In these conditions, stratified flows are not expected because they strongly depend on gravity forces.

More recently, Damianides and Westwater [21] reported experimental data with air-water flow in minitubes (1 up to 5 mm i.d.) and stated that gravitational effects become irrelevant for i.d. between 1 and 2 mm. Experimental data on two-phase-flows in microgravity conditions were first reported by the pioneering work of Heppner *et al.* [38] on board the KC-135 zero gravity aircraft. Data under microgravity became more common in the late 1980s as a consequence of an increase in accessibility for researchers to drop towers and parabolic flights.

Most of the authors agree with the existence of three main flow patterns in microgravity, namely, bubble, slug and annular. Nevertheless, there is still disagreement concerning flow pattern transitions. Eastman *et al.* [25], Karri and Mathur [43] and Crowley *et al.* [20] attempted unsuccessfully to extend transitional models and flow pattern maps existing in $1g$ to the microgravity environment. Lee [47], Zhao and Rezkallah [92], Reinarts [75] and Zaho and Hu [91] approached the subject trying to explain the forces acting on the fluids during the transitions. Zhao and Hu [91] succeeded in describing the slug-annular transition by developing flow pattern maps based on the Weber number. Dukler *et al.* [22], Colin, Fabré and Dukler [17], Colin, Fabré and McQuillen [18] and Bousman [10] developed the so called semi-empirical void fraction model, which explains the flow pattern transitions as a consequence of the coalescence between bubbles. McQuillen, Colin and Fabré [58] and Zhao [91] provided a remarkable summary of the previous studies on flow patterns, flow pattern transitions and other relevant topics concerning two-phase flows.

With respect toward the bubble-slug transition, the semi-empirical void fraction model is the most widely used. By using the drift-flux model and assembling experimental data collected in microgravity (Colin *et al.* [17], Reinarts [74], Bousman [10]) and Colin *et al.* [18] developed a model capable of predicting the bubble-slug transition based upon the Suratman number. Recently, Sen [80] has established that Su is the key dimensionless group in the bubble-slug transition in microgravity, according to the analysis of the forces.

3.2.1 Suratman number based model

According to Colin *et al.* [17], bubble velocity can be reasonably well predicted in microgravity by a drift-flux model and expressed by:

$$U_G = C_0(U_{SL} + U_{SG}) \tag{3.28}$$

In their experiments, the void fraction distribution coefficient ranges between 1.15 and 1.3. Hereafter, we will assume a $C_0 = 1.2$. Dividing by U_{SG}, Eq. 3.28 may be expressed as:

$$U_{SL} = U_{SG}\frac{1 - C_0\,\alpha}{C_0\,\alpha} \tag{3.29}$$

The authors consider the existence of a critical or transitional void fraction value, α_C, that corresponds to the required void fraction at which the bubble-slug transition occurs. Thus, the bubble-slug transition may be expressed in terms of a critical value of the void fraction.

Dukler *et al.* [22] registered a set of experimental data in microgravity in order to clarify the mechanisms that give rise to flow pattern transitions. They predict the bubble-slug transition based on a bubble diameter criterion, assuming the transition occurs when the bubble diameter reaches the value of the tube diameter. The transition is then explained as a consequence of the coalescence phenomena. Coalescence events are related to the number of collisions between bubbles. According to the authors, these events depend on the bubble packing factor, which is not allowed to exceed 0.53. For the bubble-slug transition, an $\alpha_C = 0.45$ is suggested, and Eq. 3.29 becomes:

$$U_{SL} = 1.22\,U_{SG} \tag{3.30}$$

In contrast, experiments reported by Colin *et al.* [17], Bousman [10] with different i.d., and by Reinarts [74] with other fluids than air and water (namely R12) showed that the bubble-slug transition took place for a critical void fraction around 0.2.

Taking into account the previous experimental data, Colin *et al.* [18] propose an approach to predict the bubble-slug transition. According to this approach, the transitional void fraction is related to the Suratman number. Two different regimes were pointed out for the coalescence mechanism, corresponding to two values of the critical void fraction. For low values of Su, the bubble-slug transition is controlled by bubble packing, which is known as the inhibiting coalescence regime. At large Su values, the coalescence phenomenon is promoted due to effective collisions between bubbles along their flow path. The authors conclude that:

$$Su < 1.5 \cdot 10^6 \rightarrow \alpha_C = 0.45 \tag{3.31}$$

$$Su > 1.7 \cdot 10^6 \rightarrow \alpha_C = 0.2$$

This model reconciles both values of the critical void fraction reported in previous experimental work. Nevertheless, as stated by McQuillen *et al.* [58], it does not give any insight into the mechanism of the coalescence or the influence of the specific process used to generate the bubbles.

3.3 Bubble generation in a capillary dominated regime

Following the concept of cross-flow reported by Bhunia *et al.* [7], Pais *et al.* [70] and Nahra *et al.* [63, 64], Carrera *et al.* [15] recently suggested a model for the prediction of bubble size when the bubble generation and detachment occur under capillary dominated conditions. The model is based on a mechanistic approach, which takes into account the force balance during the bubble formation.

There are several forces acting in a two-phase system. Carrera *et al.* consider inertia, buoyancy and surface tension forces to be the most significant of these forces. As stated before, the competition between inertia, buoyancy and surface tension forces can be evaluated by the Bond and Weber numbers, respectively (see Section 2.7).

In microgravity conditions or when working with capillaries, the Bond number is assumed to be small enough and the effects of gravity become negligible in comparison with the surface tension effects, thus the analysis can be considered gravity independent. Under those circumstances, the Weber number becomes a relevant dimensionless group that explains the interaction between the forces in the mixture. When We_{SG} has a value slightly lower than 2 [16, 77], the flow pattern is mainly dominated by the forces involved with surface tension, which

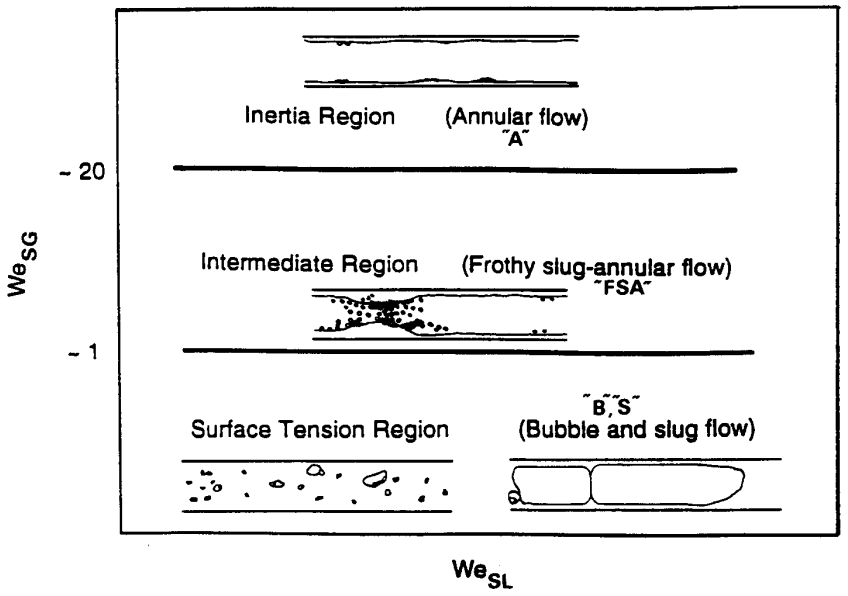

Figure 3.5: Microgravity two-phase flow pattern map based on the superficial Weber numbers [77].

includes bubble and slug flows, as shown in Fig. 3.5.

In the particular case of a T-junction, where gas is injected perpendicularly into a liquid cross-flow capillary, Carrera *et al.* assume that bubble formation and detachment are consequences of the balance between capillary forces and the drag due to liquid cross-flow, taking into account that the drag can be large even in the small flow limit when the forming bubble occupies the available cross-section of the capillary. This force balance determines bubble size and generation frequency and it can be settled by simplifying the component of the capillary force along the liquid flowing direction:

$$F_c = \pi \sigma \phi_c f \tag{3.32}$$

f being a geometric factor. We assume here the simplest case, in which both capillaries have the same circular cross-section. The drag force in the cross-flow direction is given by:

$$F_D = C \rho_L ({U_L}^*)^2 {\phi_B}^2 \left(1 + \mathcal{O}\left(\frac{1}{\sqrt{Re_B}}\right)\right) \tag{3.33}$$

where ϕ_B is the characteristic diameter of a growing bubble, and C a constant to be determined experimentally [55, 62]. The precise values of the geometrical

factors f and C are not required in this analysis. ${U_L}^*$ is the liquid velocity, which is increased due to the effective capillary cross-section reduction at the moment of the bubble formation,

$$ {U_L}^* = \frac{U_{SL}}{1 - (\gamma \bar{\phi}_B)^2} \tag{3.34} $$

where $\bar{\phi}_B$ is the normalized ϕ_B with the capillary diameter and γ is a geometric factor of the order of 1. This factor depends on the bubble size and gas/liquid flow rates but will be considered as a constant for the sake of clarity. Re_B, the bubble Reynolds number, is defined as:

$$ Re_B = \frac{\rho_L \, {U_L}^* \, \phi_B}{\mu_L} \tag{3.35} $$

By balancing both forces, the authors obtain:

$$ \frac{F_D}{F_c} = \frac{C}{\pi f} \bar{\phi}_B \, We^* \tag{3.36} $$

where We^* is the effective Weber number:

$$ We^* = \frac{\rho_L \, {U_L}^{*2} \, \phi_B}{\sigma} = We_{SL} \frac{\bar{\phi}_B}{\left(1 - (\gamma \bar{\phi}_B)^2\right)^2} \tag{3.37} $$

The key point of this model is that even for small flow rates, it is assumed that $\bar{\phi}_B \cdot We^*$ exceeds the value of a critical Weber, We^c, for large values of ${U_L}^*$. When that criteria is fulfilled, bubbles detach. According to the authors, the detachment condition can then be written as:

$$ \sqrt{\frac{We_{SL}}{We^c}} = 1 - \gamma^2 \frac{We_{SL}}{We^c} \tag{3.38} $$

which, for a small flow rate, leads to

$$ \bar{\phi}_B = \frac{1}{\gamma} - \frac{1}{2\gamma^2} \sqrt{\frac{We_{SL}}{We^c}} + \mathcal{O}\left(\frac{We_{SL}}{We^c}\right) \tag{3.39} $$

where γ and We^c must both be determined experimentally (see Subsection 7.3.1.2).

Therefore, bubble size is expected to be basically determined by the capillary diameter, being of the same order of it, and also to have a weak linear dependence on the mean velocity of the liquid cross-flow through the square root of the Weber number.

Additionally, the authors also predict that a small size dispersion is expected and can be controlled by managing the flow rates. Assuming that a range δWe^c of the critical Weber number can produce a bubble size dispersion $\delta\phi_B$ and introducing $We^c + \delta We^c$ and $\phi_B + \delta\phi_B$ in Eq. 3.39, the authors obtain the bubble size dispersion expressed as:

$$\frac{\delta\phi_B}{\phi_c} = \frac{1}{4\gamma^2}\sqrt{\frac{We_{SL}}{We^c}}\frac{\delta We^c}{We^c} + \mathcal{O}\left(\frac{We_{SL}}{We^c}\right) \tag{3.40}$$

that shows how dispersion can be controlled by reducing We, i.e., the liquid superficial velocity.

3.4 Numerical simulation

Different computational fluid dynamics methods have been recently used to study the generation of bubbles and droplets. Qian and Lawal [73] used a commercial CFD package to simulate the bubble formation in the squeezing regime of a T-junction microchannel. Their study was focused on the investigation of the effects of pressure, surface tension and shear stress action on the gas thread. Kashid *et al.* [44] discussed CFD modelling aspects of internal circulations and slug flow generation. The slug flow formation in a 120° Y-junction was simulated and velocity profiles inside the slug were obtained.

More recently, De Menech *et al.* [59] carried out a numerical investigation by means of a phase-field model of the breakup dynamics of streams of immiscible fluids in a microfluidic T-junction. Three regimes of droplet formation (squeezing, dripping and jetting) were identified and studied. In spite of the promising results obtained in these recent studies, many other aspects in the flow characterization such as the bubble generation frequency or the void fraction distribution were left unaddressed.

The numerical code JADIM (see Appendix A), which is used in this work, has been developed at the *Institut de Mécanique des Fluides de Toulouse* (IMFT) and applied to a variety of fluid dynamics problems [8, 9, 24, 48, 49, 50, 51, 52, 56]. The Volume of Fluid (VoF) modulus of JADIM is able to perform local analyses of deformable two phase interfaces by resolving the Navier-Stokes equations for incompressible fluids in non-stationary problems.

CHAPTER 4

Experimental setup

In this chapter we present a brief description of the experimental setup used in this work. Section 4.1 describes all of its components and their respective functions. Section 4.2 details the procedure followed during the realization of the experiments, while also describing the image processing protocol, which has been designed to obtain the experimental data analyzed in the following Chapters.

4.1 Experimental setup

In order to study the generation and behavior of two-phase flows in microgravity conditions, a new experimental setup has been designed. A sketch of it is shown in Fig. 4.1. It is divided into four main parts, namely, the test section, the air/water supply and the data acquisition and control systems.

4.1.1 Test section

A bubble generator, which has been previously reported [2, 3], is used in the experiments reported in this work. It is made of methacrylate and generates the two-phase flow mixture by means of a T-junction formed by two 1mm diameter capillaries, in which water and air are injected axially (x-axis) and radially (y-axis), respectively. Each inlet is fed by the air and water supply systems, respectively. Generation and detachment of bubbles is provided by the liquid

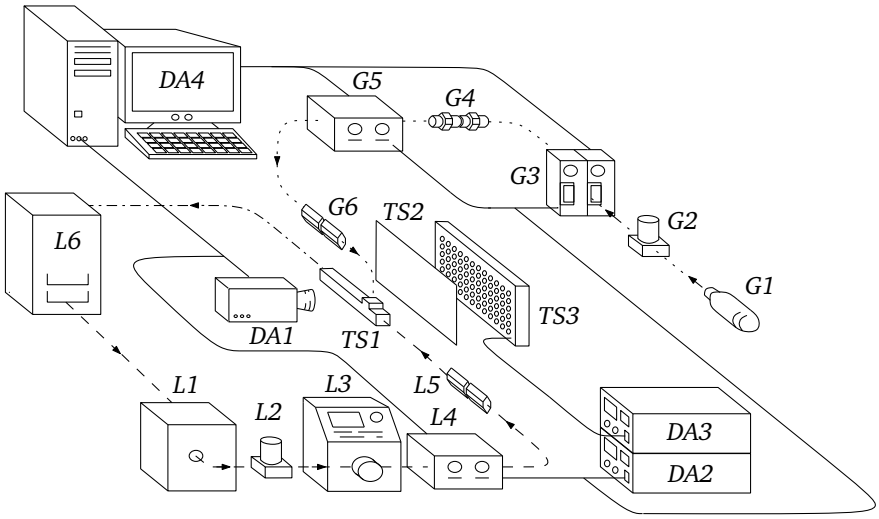

Figure 4.1: Experimental setup: *test section* (TS1: T-junction bubble generator, TS2: diffuser, TS3: light source), *air supply system* (G1: air bottle, G2: filter, G3: pressure controller/meter, G4: choked orifice, G5: air mass flow meter, G6: anti-return valve), *water supply system* (L1: water tank, L2: filter, L3: pump, L4: water mass flow meter, L5: anti-return valve, L6: waste bag), and *data acquisition and control system* (DA1: high speed camera, DA2 and DA3: power supplies, DA4: server,). *Solid lines:* electric connections, *dotted lines:* gas tube, *dashed lines:* liquid tube and *dash dotted line:* gas-liquid mixture.

cross-flow.

The axial capillary has a total length of 90 mm. To perforate the methacrylate one 1 mm i.d. unthreaded drill bit is used. Nevertheless, to make a 90 mm length and 1 mm diameter hole in a methacrylate block is not technically possible, due to the lateral vibration of the bit, which causes the methacrylate to break or to be damaged, causing lack of transparency in the latter case. For a 1 mm drill bit, the maximum reachable depth, avoiding vibrations at its tip, is roughly 15 mm. In order to overcome this problem, three independent sections are mechanized separately, drilled in both opposite faces, and joined together by means of cylindrical connectors in order to assure the right alignment of the axial capillary. These connectors do not interfere with the flow. Fig. 4.2 shows a sketch of the bubble generator, which points out the three independent mechanized parts. The inlets and outlet are also mechanized with a threaded drill bit to allow the screw-in attachment of the metallic connections from the tubing.

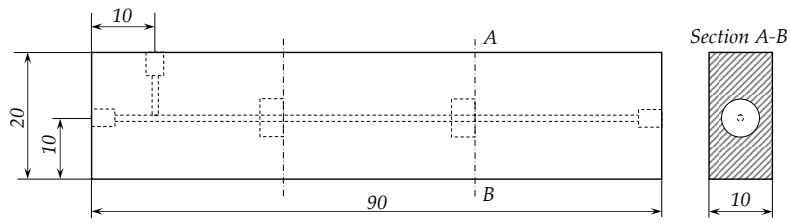

Figure 4.2: Sketch of the bubble generator showing section *A-B*. Units are in mm.

Component	Ref.	Function
T-junction	TS1	Bubbles generation
Diffuser	TS2	Homogenize light from the LEDs
LEDs	TS3	Lighting system

Table 4.1: Test section elements and their function.

The bubble generator has been designed with an outer square cross-section to avoid curved surfaces, which allows for recording the formation and detachment of bubbles without optical distortions. To set the relative distance between injector and camera, an appropriated x-axis stage has been also designed.

Exposure time of the high speed camera ranges from $80\mu s$ up to $120\mu s$, for a mixture superficial velocity of the order of $1m/s$ and $0.1m/s$, respectively. Due to the short exposure time better lighting conditions than provided by natural light are required. To provide adequate illumination, rear lighting is supplied by a light source with 308 ultra bright white Light Emission Diodes (LEDs) of 7000 mcd, which are placed in an hexagonal configuration to increase the ratio of the number of LEDs per area. LEDs are a cold light source, and thus this lighting does not significantly affect the thermal conditions of the experiments. Finally, a 60° holographic diffuser sheet is also used to homogenize light in order to enhance the image at the gas-liquid interface.

Table 4.1 summarizes the test section elements and their function.

4.1.2 Air supply system

Air is driven through the capillary under constant mass flow rate from a pressurized synthetic air bottle, which has a volume of 5 liters and an internal pressure of 200 bars. Although compressors are commonly used as air sources, they

Component	Ref.	Function
Air bottle	G1	Provide synthetic and filtered air
Gas filter	G2	Avoid undesired particles
Pressure controller	G3	Pressure control/measurement
Choked orifice	G4	Control the air flow rate
Gas flow meter	G5	Measure air flow rate
Anti-return valve	G6	Avoid reversal flow

Table 4.2: Air circuit elements and their function.

could also introduce vibrations, whereas air bottles are vibration free and provide a more regular air flow rate. Two steps are followed in order to reduce the pressure from the 200 bars inside the bottle to the required pressure at the bubble generator inlet. First, a manometer reduces the pressure of 200 bars at the bottle outlet. Pressure is thereby regulated manually from 0 up to 10 bars with an uncertainty of less than 0.1 bars. One overpressure release valve is placed at the manometer as a safety measure. To further reduce pressure, an accurate Bronkhorst® Hi-Tec's air mass pressure controller/meter regulates the pressure at the manometer outlet with an uncertainty of less than 0.01 bars. Finally, to obtain an accurate air mass flow rate, a choked orifice is placed after the pressure controller. By knowing the pressure at the chock orifice inlet, it is possible to know the pressure at the outlet and therefore the resulting gas flow rate. Additionally, by maintaining the pressure constant at the chock orifice inlet the gas flow rate stabilizes, avoiding possible fluctuations at the T-junction inlet.

The air volumetric flow rate is measured just before entering the T-junction by a Bronkhorst® Hi-Tec's air mass flow meter (F-201C9 series), which has an operational range up to $80\,ml/min$. The uncertainties in the air flow rate measurements are less than $0.5\ ml/min$. To avoid damages due to undesired particles, a HOKE®'s removable micron filter (6200 series) is placed at the outlet of the manometer. To prevent reversed flow, specially the air-liquid mixture coming from the T-junction, one anti-return valve (6100 series) is used. The tubing selected for both the air and water systems is made of Teflon. This material offers good resistance to internal pressure up to about 20 bars. Flow leakage is avoided with Gyrolok®'s standard fittings.

Table 4.2 summarizes the air circuit elements and their function.

Component	Ref.	Function
Liquid tank	L1	Storage of the distilled water
Liquid filter	L2	Avoid undesired particles
Liquid pump	L3	Control the water flow rate
Liquid flow meter	L4	Measure water flow rate
Anti-return valve	L5	Avoid reversal flow
Residual tank	L6	Storage of the mixture

Table 4.3: Water circuit elements and their function.

4.1.3 Water supply system

A water gear pump, which assures minimum fluctuation and constant flow, is used to manage water inside the liquid circuit. The model selected is an Ismatec® MCP-Z pump, able to inject water flow ranging from about $0.1 ml/min$ up to $100 ml/min$. An uncertainty less than $1\ ml/min$ has been estimated for the liquid pump. Distilled water is stored in a liquid tank from which water is pumped. The tube connecting the water reservoir to the pump is immersed in the tank to avoid air passing into the pump or the liquid flow meter. The water level inside the tank must be checked regularly. A HOKE® 's removable micron filter is located at the pump inlet. Water flow rate is measured at the inlet of the capillary by a Bronkhorst® Hi-Tec's liquid flow mass meter (L30 series), with an operational range up to $100\, ml/min$ and uncertainties less than $0.5\ ml/min$. One reverse valve is placed at the Liquid-flow outlet to protect it from reversal flow. Residual air and water coming from the injector outlet are accumulated in a residual tank that is connected to the main water tank, to which the water is conducted.

Table 4.3 summarizes the water circuit elements and their function.

4.1.4 Data acquisition and control system

One high speed video camera Redlake® MotionXtra HG-SE with a Complementary Metal Oxide Semiconductor (CMOS) sensor is focused at the T-junction to record the detachment and formation of the bubbles. Its recording velocity ranges from 500 (with a maximum resolution of $1280x1024$ pixels) up to 32000 frames-per-second. The power required by the light source is provided by a DC regulated Blausonic® power supply with a maximum output of $30V$ and $5A$. Both air and water mass flow meters as well as the pressure controller/meter

Component	Ref.	Function
CMOS camera	DA1	Record videos
DC supply 1	DA2	Electrical power supply to LEDs
DC supply 2	DA3	Electrical power supply to flow meters and pressure controller
Server	DA4	Data storage and LabView control

Table 4.4: Data acquisition and control elements and their function.

are connected to a second DC regulated Blausonic® power supply.

One data acquisition computer controls and monitors the inputs coming from the pump, both flow meters and the pressure controller/meter, thus allowing the control of both gas and liquid volumetric flow rates. The inputs/outputs of these equipments are shown in a graphical interface and stored by LabView®. The images are transferred into an image-processing computer via an IEEE1394 Firewire-Interface. A standard image software provided by the camera manufacturer is used for the image-processing.

Table 4.4 summarizes the data acquisition and control elements and their function.

4.2 Description of the experiments

Experiments are performed on ground imposing constant liquid volumetric flow rates ranging from 0.2 up to 80 ml/min while varying air volumetric flow rates from 0.25 to 80 ml/min. To this end, the liquid pump has to be regularly calibrated to minimize experimental errors. Once the flows have stabilized, images of the T-junction and the capillary are taken for each chosen pair of values Q_G and Q_L by means of the high speed camera set at 4000 fps and a resolution of $640x512$ pixels. Each video is composed of 1000 frames and hence, each video lasts for 0.25 s. Fig. 4.3 shows an example of recorded data in which pressure at the pressure controller/meter outlet and both gas and liquid flow rates at the T-junction inlets are shown. In this example, Q_L is maintained constant while the value of Q_G is changed for five different experiments. As can be noted, the time during which Q_G and Q_L remain constant (typically of the order of 10 seconds) is longer than the 0.25 s required for recording, in order to ensure stationary flow conditions. Note also the short response time of the gas flow meter when vary-

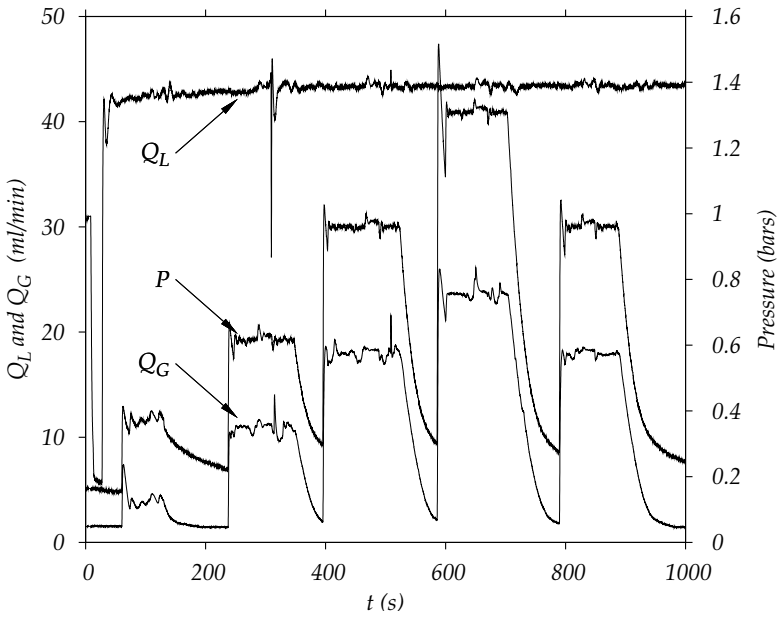

Figure 4.3: Recorded data during experiments: Q_L, Q_G and P.

ing the set point in the pressure controller.

The temperature is maintained at approximately $20°C$ in all experiments. Due to the short duration of the experiments, both the thermal effects of the room temperature fluctuation and the increase in temperature due to the light source provided by the LEDs can be neglected and the experiments are assumed to be adiabatic. The cross-section averaged the air and water velocities, in other words the superficial gas and liquid velocities, are obtained from the volumetric flow rates (see Eqs. 2.8 and 2.9).

4.2.1 Image processing

With the objective of facilitating image analysis, the images are subjected to a process of binarization. As a result, we obtain new images that are easier to analyze, in which only bubbles can be visualized. Firstly, the background is subtracted from the actual image (Fig. 4.4-a), in order to remove the illumination heterogeneities that could have been produced by the lighting system. Additionally, the image contrast is also changed to achieve a more homogenized image (Fig. 4.4-b). Due to the capillary curvature, shadows appear at the capillary upper and bottom parts. Several image filters are used to soften them (Fig. 4.4-

c). Finally, a segmentation tool allows us to choose which range of colors will appear as black, leaving the remaining colors as white (Fig. 4.4-d).

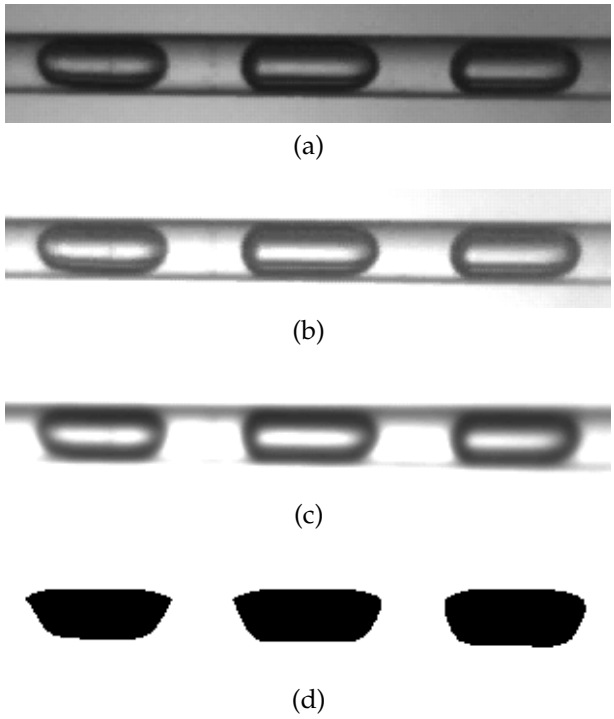

Figure 4.4: Image processing protocol: *(a)* actual image, *(b)* background subtraction and changes in contrast, *(c)* image filtering, *(d)* image segmentation.

Analysis of the videos permits one to identify the flow pattern and classify each experiment into bubble, slug, churn or annular flow regime. This task can be susceptible to the subjectivity of the researcher, especially in the two former flow regimes. Both bubble and slug flow patterns are defined as proposed by Dukler *et al.* [22]. Under this definition, the transition between bubble and slug flow patterns is considered to take place when the bubble diameter reaches the value of the capillary diameter (see Subsection 3.2.1).

Due to the operative limitation of the gas and liquid flow meters, most of the experiments recorded belong to bubble or slug flow patterns. Since gas flow meters with higher operational limits are required for an accurate analysis of churn and annular flow regimes, such analysis were not performed in this study.

Figure 4.5: Bubble being detected by a rectangular AOI with a length of 1 pixel.

In addition, measurement of bubble generation frequency, bubble velocity, as well as bubble, unit cell and liquid slug lengths are carried out by means of the standard image software.

The software enables the user to active an Area of Interest (AOI) on the image, which can have any shape and be placed anywhere. We use a rectangular AOI with a length of 1 pixel, the minimum allowed by the software. Black objects are detected when entering the AOI (see Fig. 4.5) and the software automatically records it on the datafile with a 1. Fig. 4.6 shows an example of several bubbles detected during 100 ms (400 frames). The generation frequency, f, can then be calculated by knowing the total number of tracked objects, the recording speed and the number of frames by means of Eq. 4.1. The larger the number of frames, the more accurate the results will be.

$$f = \frac{\#objects \cdot \#fps}{\#frames} \tag{4.1}$$

The maximum generation frequency registered in our experiments is roughly 1200 bubbles per second (see Appendix B), almost four times smaller than the recording speed. In each case, frequency aliasing is thus avoided, hence this process is correctly resolved by the image acquisition system. 1000 Frames per video results in being an appropriate number to accurately determine the frequency. A macro was programmed to define the procedure from the original images to the final data output. This macro automatically performs the entire process of image processing, enhancement and bubble detection.

The analysis of the recorded images also allows the measurement of the gas velocity. The gas is contained within the bubbles, and thus it is acceptable to assume that the gas velocity is equal to the bubble velocity, which can be measured with the standard image software. To this end, the image must be calibrated, what we do through the capillary diameter. A tracking option permits

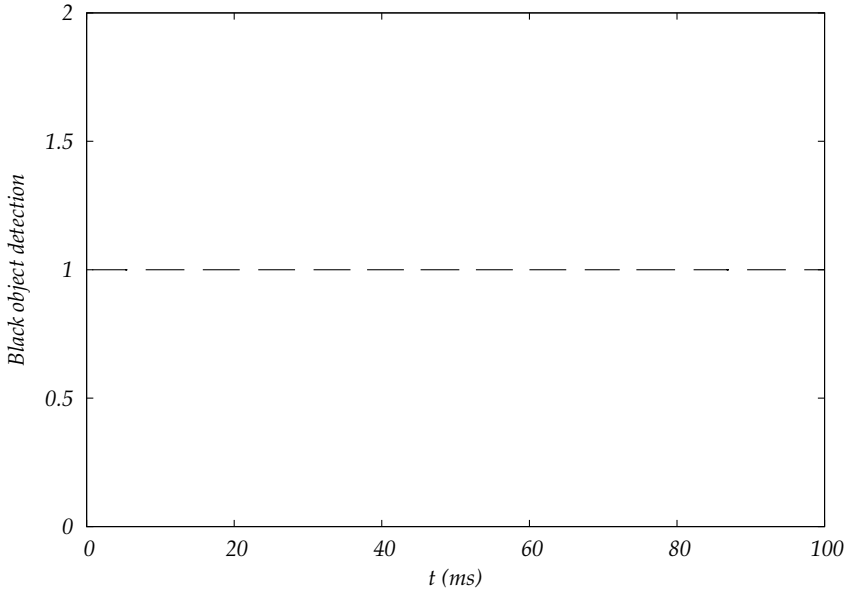

Figure 4.6: Bubble detection by using the standard image software during 100ms (400 frames). U_{SG}=0.242m/s and U_{SL}=0.212m/s.

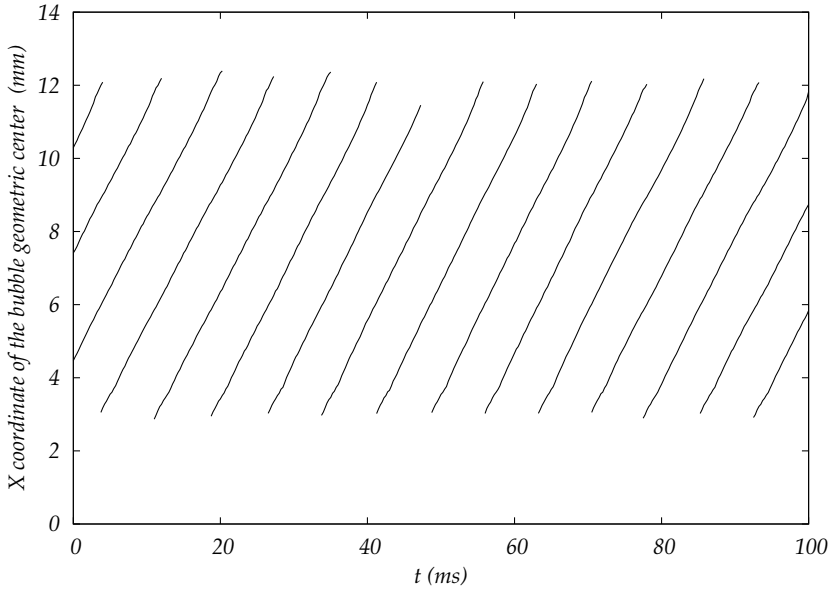

Figure 4.7: Bubbles tracking and gas velocity estimation by using the standard image software during 100ms (400 frames). U_{SG}=0.242m/s and U_{SL}=0.212 m/s.

Element	Uncertainty
Manometer	< 0.1 bars
Pressure controller	< 0.01 bars
Gas flow meter	< 0.5 ml/min
Liquid flow meter	< 0.5 ml/min
Liquid pump	< 1 ml/min
Image processing	< 0.07 mmm

Table 4.5: Uncertainties from the experimental apparatus and the image processing.

user to track all black objects, reporting the x coordinate of their geometrical center. In bubbles longer than the capillary diameter, no movement is observed in the y-axis. In smaller almost spherical bubbles this is the case only just after the detachment until they reach the centerline. Therefore, we assume that the velocity has its main component in the x direction. Fig. 4.7 shows the tracks of several bubbles as an example. Once the bubble velocity is known, we can then estimate the mean void fraction with Eq. 2.11.

Finally, the bubble, unit cell and liquid slug lengths are measured directly from the images as defined in Fig. 2.2. The gas/liquid interface is often blurred and overshadowed, particularly in those cases where the bubble velocity is high (on the order of $1\,m/s$) and thus, some uncertainties appear. An error of approximately $\pm 0.07\,mm$ has been estimated when measuring the bubble interface, which corresponds to an error of two pixels.

4.2.2 Analysis of the measurement errors

A simple analysis of the measurement errors has been performed. The intent of this analysis was not to exhaustively study the measurement errors presented at the time of taking measurements from each experiment, but to establish the maximum error values as an error threshold. Therefore, this analysis can be further improved, and a more exhaustive error analysis could be done for obtaining more accurate results in the analysis of the measurement errors. In any case, the values obtained in this analysis have been found to be of lower order of magnitude than their respective measured experimental data.

The uncertainties from the experimental apparatus, as well as from the image processing, were taken into account in this analysis. Table 4.5 summarizes these uncertainties. Table 4.6 shows the maximum error values estimated for all of the

parameters measured from the experiments, where these errors are expressed in absolute value. Therefore, a more accurate value, p_0, for a given measured parameter p could be expressed as:

$$p_0 = p \pm \epsilon_p \tag{4.2}$$

ϵ_p being the maximum error found for that given parameter. The gas superficial velocity error was estimated by adding the two contributions in uncertainty from the pressure controller and the gas flow meter (less than 0.18 ml/min and 0.5 ml/min, respectively). This addition gave a maximum uncertainty of less than 0.68 ml/min, which corresponds to a superficial velocity of less than $1.4 \cdot 10^{-2}\, m/s$ for a 1 mm i.d. capillary. In the case of the liquid superficial velocity, the liquid pump and the flow meter uncertainties were taken into account (1 ml/min and 0.5 ml/min, respectively). This calculation provided a maximum error of 1.5 ml/min, which corresponds to a maximum superficial velocity of $3.2 \cdot 10^{-2}\, m/s$.

The greater errors were generally found in those experiments with larger bubble velocities. Time used when calculating the gas velocity was smaller in those cases, thus causing the error associated to the gas velocity to increase. For gas velocities of the order of 1 m/s, an uncertainty of typically 1 frame (when tracking a bubble) causes a maximum inaccuracy in time of 0.1. The total gas velocity error could be estimated as $U_G \cdot 0.1 m/s$.

The maximum generation frequency errors were also found in these experiments with larger superficial velocities, especially in those cases where a bubble flow regimen with very small bubble sizes was observed. The interface became harder to detect in these case, and the bubble tracking failed sometimes in detecting very small bubbles. A maximum generation frequency error of 20 Hz was estimated for the generation frequency.

Finally, the inaccuracy associated to the measurement of the lengths was estimated by taking into account the error when measuring the interface (0.07 mm, as stated before). The maximum value could be obtained when this inexactitude was done twice, namely when measuring the front and back part of a bubble. Hence, the maximum error in the unit cell, bubble and slug of liquid length were estimated to be $2x0.07 = 0.14\, mm$

Parameter	Maximum error ϵ_p
U_{SG}	$< 1.4 \cdot 10^{-2}\, m/s$
U_{SL}	$< 3.2 \cdot 10^{-2}\, m/s$
U_G	$< U_G \cdot 0.1 m/s$
f	$< 20\, Hz$
$L_{UC}/L_B/L_{LS}$	$< 0.14\, mm$

Table 4.6: Estimated uncertainties from the experiments.

4.3 Conclusions

A new experimental setup has been designed to perform the experiments reported in this work. The experiments are carried out on ground with air and water in conditions relevant for a microgravity environment. The gas and liquid flow rates are accurately controlled and measured at the T-junction inlets by means of the gas and liquid systems, respectively. Readable data from a pressure controller/meter, gas and liquid flow meters and a liquid pump are monitored. The gas and liquid superficial velocities are estimated from the gas and liquid flow rates.

The data acquisition and control system provides high quality images of the two-phase flow at 4000 fps , which can then be analyzed afterward. A first analysis of the images permits their classification into bubble, slug, churn and annular flow regimes. One standard image software allows to enhance the images, extracting the bubble generation frequency and velocity, as well as the lengths of the bubble, unit cell and liquid slug. The mean void fraction can be estimated from the bubble and gas superficial velocities.

CHAPTER 5

Flow pattern map, bubble velocity and void fraction

In this chapter we present the several flow regimes observed in our experiments, as well as some results regarding bubble velocity, mean void fraction and the bubble-slug transition.

In Section 5.1 the experimental data used in this work are presented. Section 5.2 describes an experimental pattern flow map obtained with our T-junction in conditions relevant for a microgravity environment. We compare our results in bubble velocity and mean void fraction with existing models such as the drift-flux one in Section 5.3 and 5.4, respectively. We address questions regarding the existence of a critical void fraction in order for the bubble-slug transition to occur in Section 5.5. The drift-flux and Suratman models are contrasted with our data in order to determine the bubble-slug transition in our system.

5.1 Experimental data

More than 400 experiments have been performed during this work, of which 301 have been selected for analysis. The rest were discarded due to several errors that occurred during those experiments. A total of roughly 400000 images have been analyzed to obtain the results presented in this study.

FP	U_{SG} $[m/s]$	U_{SL} $[m/s]$	U_G $[m/s]$	α	Bo	We_{SL}	Re_T	Ca_T	St
Bubble	0.005	0.308	0.711	0.016	0.139	1.315	598	0.008	0.023
	0.950	1.698	3.073	0.249	0.139	40.03	2648	0.037	0.555
Slug	0.011	0.042	0.219	0.127	0.139	0.025	155	0.002	0.055
	2.101	1.698	3.469	0.790	0.139	40.03	2950	0.041	0.465
Churn	0.950	0.022	1.156	0.570	0.139	0.007	973	0.014	0.075
	2.101	0.743	3.080	0.794	0.139	7.66	2844	0.039	0.183

Table 5.1: Range of parameter values for each flow pattern.

As expected in microgravity conditions [22], bubble, slug, churn and annular flows have all been observed (see Fig. 5.1). Bubble and slug flow regimes appeared in most of the experiments, with a total number of 105 and 170 cases, respectively. Churn and annular flow regimes were detected in 24 and 2 experiments, respectively. Therefore, this work in primarily focused on the discussion of bubble and slug flow regimes, including the transition between them.

Table 5.1 summarizes the experimental data by showing the minimum and maximum values of several relevant parameters found in the bubble, slug and churn flow regimes. Note that the values of a given row do not correspond to one single experiment. More detailed information on data collected during the experiments can be found in Appendix B.

A Bond number with a value of 0.139 is found in all experiments, fulfilling the criterion of Suo and Griffith [83] (see Eq. 3.27). It can then be assumed that capillary forces dominate over buoyancy forces and in this way conditions relevant for a microgravity environment are fulfilled. This fact is the key point of the performance of the bubble generator in this work, making it gravity independent.

In nominal conditions, the value of We_{SL} ranges from the order of 10^{-3} up to 10 whereas Ca_T ranges between 10^{-3} and 10^{-2} for the air/water mixture flow. Therefore, capillary forces also dominate over inertial and viscous forces. Finally, the Re_T ranges from the order 10^2 up to 10^3, with a maximum value of about 3000. The limits of the laminar to turbulent transition regime are not well delimited in the literature (see Section 3.1.3.2). Hereafter, we assume that the

experiments have been developed into the laminar and/or the laminar to turbulent transition regimes.

5.2 Flow pattern map

Gas flows in the capillary, being periodically distributed in bubble and slug flow regimes. Whereas gas forms discrete bubbles inside the liquid phase in bubble flow (Fig. 5.1-a), bullet-shaped bubbles occupy almost the entire minichannel cross-section in slug flow (Fig. 5.1-b). Contrary to other experiments with different systems of bubble generation as reported by several authors, we have not observed any pattern with mixed characteristics of bubble and slug flows (that is, small bubbles dispersed into the liquid slug of two consecutive longer bubbles). This is a consequence of performance of the bubble generator, which under laminar conditions is characterized by small bubble size dispersion and high regularity in bubble generation for both bubble and slug regimes [2, 3] (see Section 3.3).

On the other hand, the liquid slug between consecutive bubbles becomes highly unstable in churn flows (Fig. 5.1-c). In this case, the gas-liquid interface constantly fluctuates as a consequence of being perturbed by the gas inertia and the nose and tail of successive bubbles collapse in an oscillatory way. In annular flow regime, gas flows at the center of the minichannel, forming a core region (Fig. 5.1-d).

A flow pattern map based on the measured gas/liquid superficial velocities is plotted in Fig. 5.2.

5.3 Bubble velocity

The bubble velocity is known to exceed the average speed of the mixture, and is usually expressed using the drift-flux relationship considering zero-gravity conditions as expressed by Eq. 3.28:

$$U_G = C_0(U_{SL} + U_{SG}) \tag{5.1}$$

The behavior of gas velocity with respect to the mixture velocity is shown in Fig. 5.3. Points correspond to experimental data of bubble, slug and churn flows. The plotted linear fitting corresponds to Eq. 5.1.

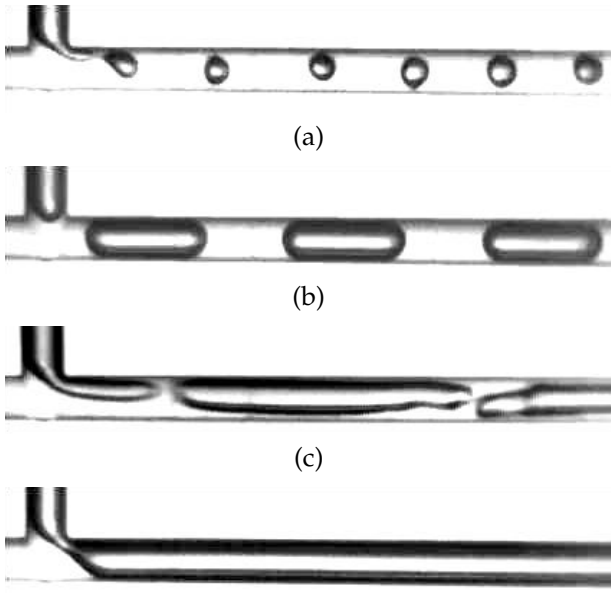

Figure 5.1: Flow generation at the T-junction and examples of gas/liquid flow patterns: *(a)* bubble, *(b)* slug, *(c)* churn, and *(d)* annular flow regimes.

The linear relation and the value of C_0 obtained are the same for both bubble and slug flow regimes and coincide with their behavior in microgravity. As a matter of fact, in microgravity both regimes present similar velocity and void fraction profiles, with gas concentrating at the centerline and not at the wall, therefore causing C_0 to be greater than 1 (see Subsection 3.1.3.1). However, these profiles are different in normal gravity, resulting in different C_0 for each flow pattern.

In churn flow, contrary to in bubble and slug flow regimes, the inertial effects become dominant and mask the superficial effects. The gas-liquid interface deforms and the liquid slug destabilizes. Additionally, the breakup of the gas thread that develops after the T-junction becomes also irregular. As a consequence, regularity in bubble generation and size is lost. Nevertheless, it is interesting to note that in those cases where it was possible to measure it, bubble velocity in churn flows seems to also follow the tendency described by Eq. 5.1. However, these examples are too scattered to reach any definitive conclusions. No velocity was measured for the annular regime in any of the experiments.

The fitting of our experimental data with Eq. 5.1 gives rise to a value of

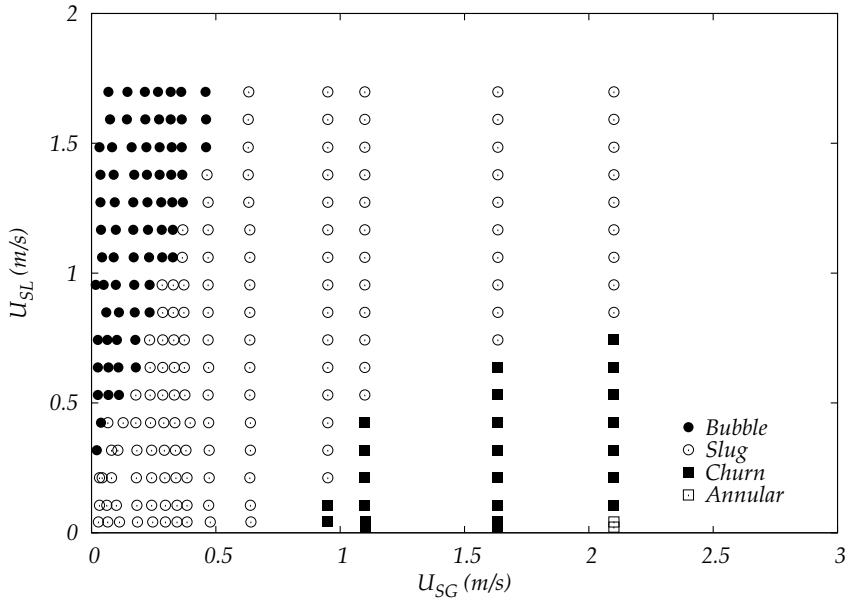

Figure 5.2: Experimental flow pattern map based on the gas/liquid superficial velocities.

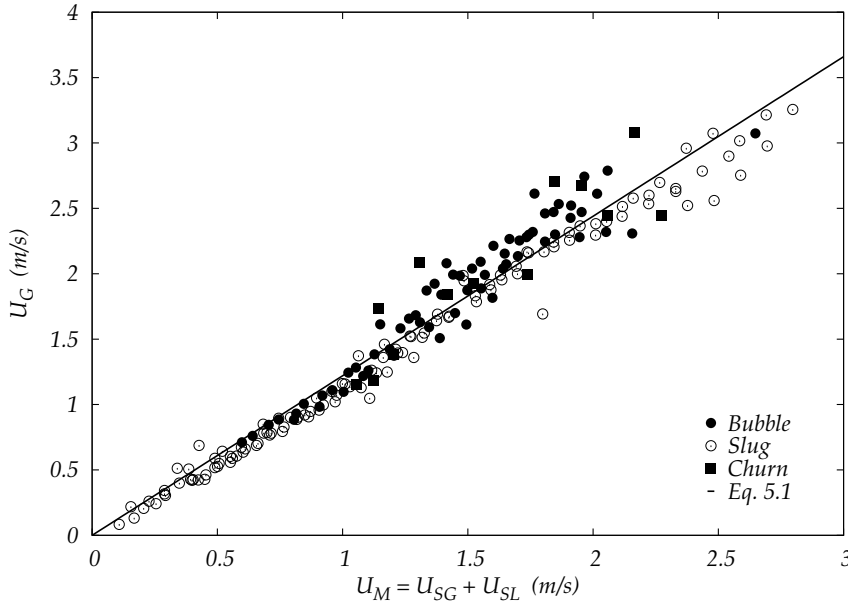

Figure 5.3: Gas velocity as a function of the mixture velocity. *Symbols:* experimental data, *line:* linear fit (Eq. 5.1).

C_0=1.22, which agrees with the typical values found in microgravity conditions (see Subsection 3.1.3.2). The fact that the same C_0 was reached for all three regimes shown in Fig. 5.3 confirms that our experiments were performed in microgravity-related conditions, as expected due to the small Bond number at which the experiments were carried out.

5.4 Void fraction

The mean void fraction has been estimated through the bubble velocity and the gas superficial velocity by taking into account the definition of the true averaged gas velocity described by Eq. 2.11:

$$\alpha = \frac{U_{SG}}{U_G} \tag{5.2}$$

This expression provides a good method to estimate the void fraction from experimental readable data. Rewriting Eq. 5.1 and combining it with Eq. 5.2, a prediction of the mean void fraction as a function of the ratio between the gas and liquid superficial velocities (pseudo void fraction) can be obtained:

$$\alpha = \frac{1}{C_0}\left(1 + \frac{1}{\frac{U_{SG}}{U_{SL}}}\right)^{-1} \tag{5.3}$$

Mean void fraction values calculated with Eq. 5.2 are compared to the prediction proposed by Eq. 5.3 in Fig. 5.4, showing a good agreement. As will be discussed in the next Section, note that the bubble-slug transition seems to occur for $\alpha = 0.2$. The scatter in the churn flows and the upper part of the slug flow regime could be due to measurement uncertainties. The number of experimental data for churn flow is not sufficient to precisely predict the mean void fraction value at which the slug-churn transition occurs. Nevertheless, it is expected to occur for a void fraction ranging from 0.6 up to 0.8 [33].

5.5 Bubble-slug transition

The existence of a critical void fraction separating bubble and slug flow patterns can be observed in Fig. 5.4, as it was predicted by Eq. 3.29 (see Section 3.2.1). Bubble and slug regime data are mostly separated by one void fraction line at $\alpha = 0.2$, verifying the transition between flow regimes at that value. This is confirmed in Fig. 5.5, in which an enlargement of the bubble/slug region shown in Fig. 5.2 is presented. The straight line separating bubble and slug flow regimes

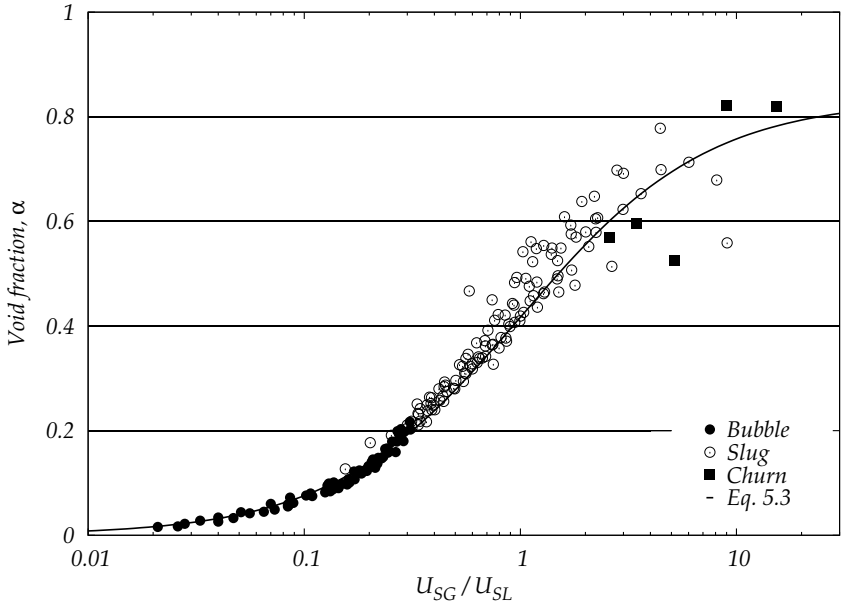

Figure 5.4: Mean void fraction as a function of gas-liquid superficial velocities ratio U_{SG}/U_{SL}. *Symbols:* experimental data, *line:* prediction (Eq. 5.3).

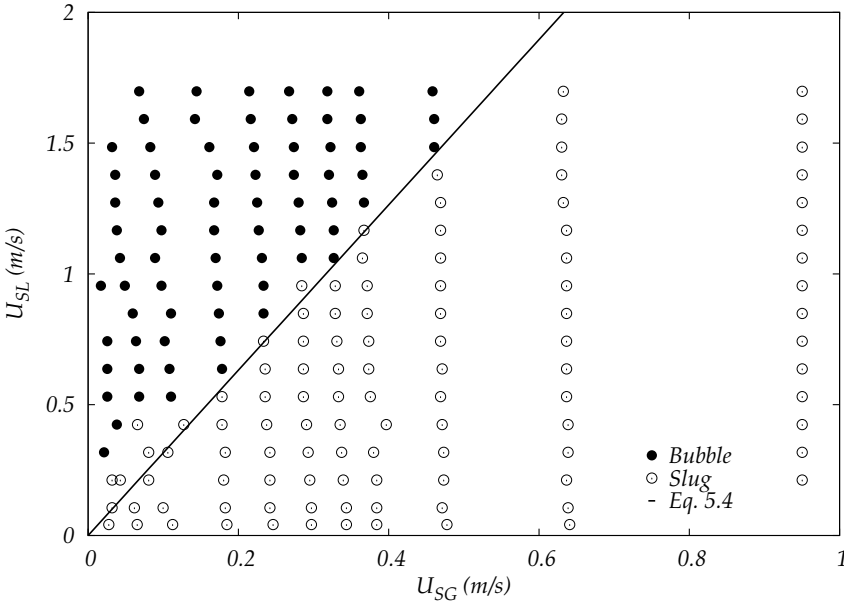

Figure 5.5: Experimental flow pattern map based on the gas/liquid superficial velocities. *Symbols:* experimental results, *line:* bubble-slug transition line corresponding to $\alpha = 0.2$.

corresponds again to a void fraction equal to 0.2, further verifying the transition at that value. By considering $\alpha_C = 0.2$, we thus obtain from Eq. 3.29:

$$U_{SL} = 3.16 \cdot U_{SG} \tag{5.4}$$

Slug flow regime points lying on the left of the transition line are not accurately predicted by Eq. 5.4. This fact can be due to uncertainties in the classification of the regimes as a consequence of some imprecision when applying the Dukler's criterion (see Section 4.2.1).

On the other hand, our experiments are associated to a value of Su equal to $7.1 \cdot 10^4$, which corresponds to the inhibiting-coalescence regime according to the model of Colin *et al.* [17]. This fact would imply a critical void fraction of 0.45 (see Subsection 3.2.1) instead of 0.2, which corresponds to the promoting-coalescence regime. This discrepancy is the reason why the relation expressed in Eq. 5.4 is different from that of Eq. 3.30 predicted by Dukler *et al.* [22]. Thus, apparently no agreement exists between the Su model and our results.

However, the key to understanding these discrepancies is to realize that coalescence does not play any relevant role in the two-phase flow generated in our bubble generator. Bubble and slug flows are generated as a consequence of the entrance effect at the T-junction and not from the collision and packing of previously generated bubbles. The T-junction used in our experiments inhibits coalescence in the direction transversal to the liquid flow (y-axis) because it is not possible to simultaneously generate two bubbles with the geometric center at the same cross section. Thus, coalescence can only take place along the axis parallel to the flow (x-axis). This occurs when a bubble places itself near the centerline and increases its velocity sufficiently to overtake the next one (if this second bubble is placed far from the centerline). This behavior has only been observed in some experiments with high liquid superficial velocities, when the Reynolds number increases and goes beyond the laminar regime, also causing the dispersion in bubble size to increase.

Thus, since the role of coalescence is not relevant in this work, we conclude that the model based upon the Suratman number cannot be applied to our minichannel or any other equivalent tube. In this way, the disagreement with respect to the Su model becomes irrelevant and further studies concerning the mechanisms of bubble generation and detachment are required in order to gain a better understanding of the bubble-slug transition in our system.

The influence of the channel length on the bubble-slug transition remains an

open question. Due to the small length-to-diameter ratio of the observed part of the minichannel (around 30), the influence of the entrance T-junction on the developing flow patterns can be considered significant. Additional experiments with larger length-to-diameter ratios should be performed in order to well establish the influence of the channel length on the bubble-slug transition.

5.6 Conclusions

In this chapter, we have carried out an experimental study on the bubble velocity, mean void fraction and the transition between the bubble and slug flow patterns for a broad range of gas and liquid flow rates. All types of pattern flows (bubble, slug, churn and annular) that can be found in microgravity conditions have been observed. Results in normal gravity and microgravity conditions did not show significant differences due to the small value of the Bond number.

A flow pattern map in terms of the superficial gas and liquid velocities has been obtained. It confirms the existence of a critical void fraction that characterizes the bubble-slug transition.

Bubble velocity has been well predicted by using a drift-flux model under the assumption of no drift velocity of the gas relative to the mean fluid velocity. The experimentally estimated mean void fraction has confirmed the theoretical prediction given by the drift-flux model.

The value of Su in our experiments and its corresponding critical void fraction did not coincide with Colin *et al.*'s predictions. In fact, the large influence of the entrance effects and the small relevance of coalescence in our system make it different from the types of systems where the Su model's predictions are applicable.

CHAPTER 6

Bubble generation frequency

This chapter discusses the phenomenon of bubble generation, focusing on the generation frequency as one of the most relevant parameters of the process. We also focus on the regimes found within a large range of gas and liquid flow rates and, in particular in bubble and slug flow regimes, due to their high regularity. A fitting of the experimental points provides an analytical expression for the frequency generation.

In Section 6.1 an analysis of the bubble generation phenomenon is presented. Some relevant parameters involved in its behavior are also presented. The study of the normalized frequency, by means of the Strouhal number, is presented in Section 6.2.

6.1 Frequency regimes

Under laminar conditions, with flow rates of the order of $1\,ml/min$, the bubble generation is characterized in our bubble generator by small bubble size dispersion for both bubble and slug regimes (see Section 3.3). The bubble detachment is very regular, in such a way that the generation frequency is very well defined [2, 3]. Gas flows periodically distributed in bubble and slug regimes, as stated in Section 5.2. However, in the large flow rates regime, this regularity is sometimes lost according to the irregular behavior inherent to the high gas inertia flow regimes, namely churn and annular flow.

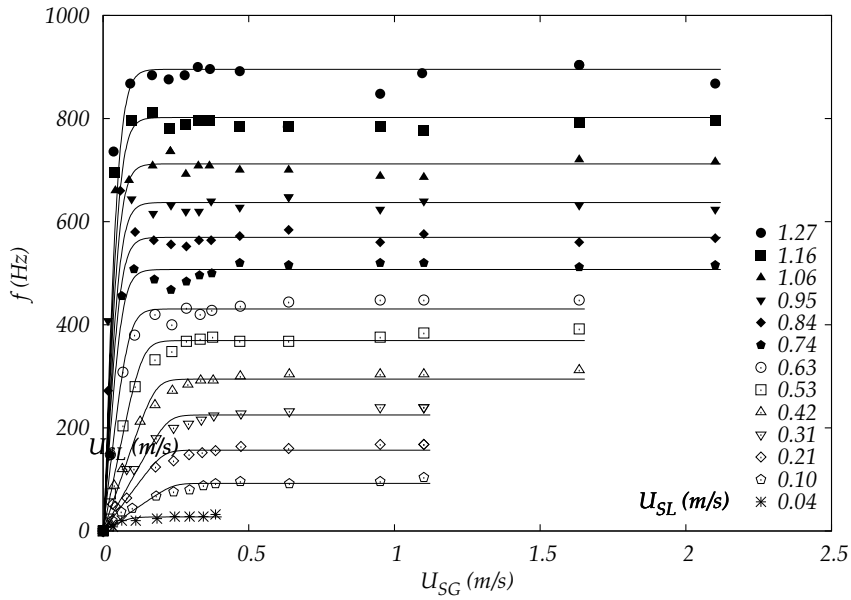

Figure 6.1: Bubble frequency f as a function of the superficial gas velocity U_{SG} for different superficial liquid velocities U_{SL}. *Symbols:* experimental results, *lines:* fit (Eq. 6.4).

Fig. 6.1 shows the dependence of the bubble generation frequency on the superficial gas velocity at different superficial liquid velocities. Points correspond to slug (mainly) and bubble flow regimes, although churn and annular regimes have also been observed at low U_{SL} and high U_{SG}. This parameter region corresponds to the lower right corner of the figure and explains why no frequency was measured there due to the loss of bubble generation regularity in churn and annular regimes.

Regardless of the liquid flow rate, the behavior of the frequency shows two distinguishable regimes: a linear regime at low U_{SG} and a saturation regime at higher U_{SG} values.

We can identify the first regime as the slow flow regime analyzed by Carrera *et al.* [15] and summarized in Section 3.3, where the linear behavior is a consequence of the bubble size being independent from the gas flow rate for small fluxes. The physical idea is that in this regime, the detachment of the forming bubble at the T-junction occurs when the liquid drag F_D is large enough to overcome capillary forces F_c. Moreover, Eq. 3.39 predicts a bubble size independent of U_{SG} in this regime, which corresponds to a generation frequency

proportional to U_{SG} as seen in Fig. 6.1. Therefore, in the linear region, while the liquid flow regulates the bubble size through the liquid drag, the bubble generation frequency is controlled by the gas flow. Hence, increasing the amount of injected gas does not result in bigger sizes but in greater frequencies. More results regarding the bubble length are provided in Section 7.3.2.

An appropriate parameter to quantitatively analyze this region is accordingly the initial slope a, i.e., when U_{SG} tends to zero. This parameter is related to the minimum bubble volume achievable for a given U_{SL}, which in this regime is expected to depend only on the liquid flow, as previously stated. The initial slope must then also be related to the minimum bubble length capable of being generated for a given U_{SL}. Further discussions about this issue are developed in Subsection 7.3.2.3.

By assuming a high regularity in bubble generation and small size dispersion, it is possible to obtain a prediction of the frequency at low gas flow rates as follows:

$$f = \frac{Q_G}{V_B} = a^* \, Q_G = a^* \, A \, U_{SG} = a \, U_{SG} \tag{6.1}$$

where V_B is the average bubble volume, and a^* has been normalized with A, the cross-sectional area. Fig. 6.2 shows an enlargement of the region corresponding to the low values of gas injection. This graph has been plotted by using experimental data focused in this region (see Appendix B). It clearly shows that although the frequency behavior is not perfectly linear, because the slope changes as f approaches its saturation value, the approximation provided by Eq. 6.1 is in good agreement with the actual behavior.

On the other hand, for large superficial gas velocities (above $0.4\,m/s$) there is a limiting scale for the bubble generation, which explains the origin of the saturation regime. This temporal scale is the time needed by the liquid flow to cross a distance of the order of the capillary diameter, Q_L/ϕ_c^3, proportional to U_{SL}/ϕ_c, which hence should mark the minimum time necessary to form a bubble at the T junction and then give the saturation frequency for the generation process [3].

Complementary to Eq. 6.1, one could consider the following expression:

$$f = \frac{Q_L}{V_L} = \frac{Q_L}{A \, L_{LS}} = \frac{U_{SL}}{L_{LS}} \tag{6.2}$$

where V_L is the volume of liquid required for detaching a bubble, and thus L_{LS} being the characteristic length of the liquid slug. When U_{SG} increases, f

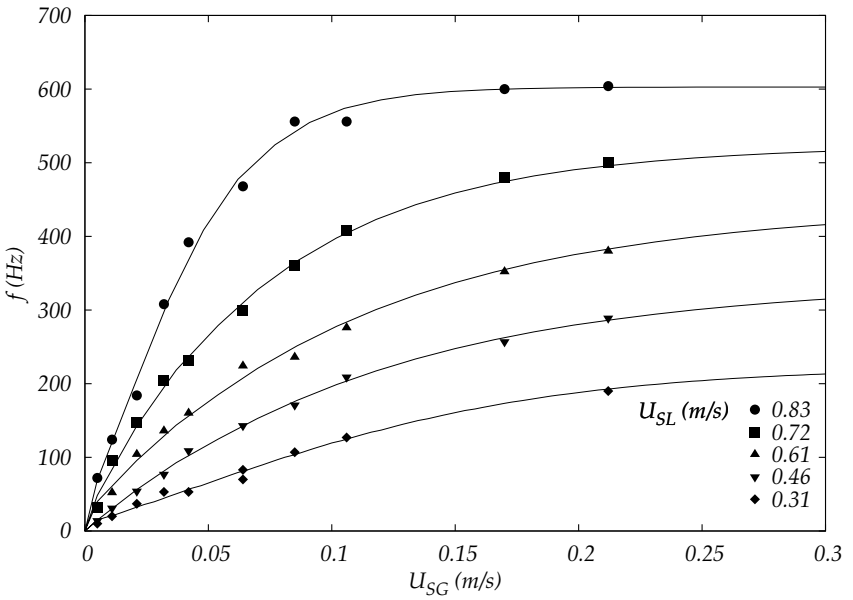

Figure 6.2: Generation frequency as a function of the gas superficial velocity. Detail of the low gas flow regime

also increases up to its saturation value f_{sat}. At that point, the amount of liquid required to generate a bubble is minimizes and therefore, L_{LS} reaches the minimum value L_L. Further increasing of the gas flow rate does not imply larger generation frequencies, but instead larger bubbles. For each value of the superficial liquid velocity:

$$f_{sat} = \frac{U_{SL}}{L_L} \sim \frac{U_{SL}}{\phi_c} \tag{6.3}$$

By knowing the behavior of the frequency at the linear and saturation regime, it is possible to define an analytical prediction of the frequency. Eq. 6.4 is defined in that way as a simple function in order to smoothly connect the two desired behaviors, a linear function and a constant saturation value. Such behavior thus involves four parameters: the initial slope, the value of the saturation frequency, the crossover point U_{SG0}, and the scale of the crossover region ϵ:

$$f(U_{SG}, U_{SL}) = f_{sat} - a \cdot \epsilon \cdot Ln\left(1 + exp\left(\frac{U_{SG0} - U_{SG}}{\epsilon}\right)\right) \tag{6.4}$$

U_{SG0} is defined as the superficial gas velocity at the crossover point between linear and saturation regimes, the point where a line starting at the origin with a slope a intersects the horizontal line of the saturation region, and hence:

$$f_{sat} = a \cdot U_{SG0} \tag{6.5}$$

Note that in case that small and monodispersed bubble sizes were the desired feature of the bubble generator, the crossover to the saturation regime would mark the optimal operation regime, because at that point the maximum number of bubbles with a minimum total surface is achieved.

Of these parameters, two of them the initial slope and the saturation frequency, carry a clear physical meaning and can be related to theoretical considerations, as stated before. The length of the crossover region is of no clear interest as long as it is small enough to allow both regimes to be observable and has a negligible effect on the computed results for the other two, physically more relevant, parameters. For the sake of clarity and due to the fact that ϵ did not give any new physical insight, it has been chosen as the superficial velocity corresponding to the characteristic volumetric flow rate of $Q^* = 1\,ml/min$, thus being $\epsilon = Q^*/A = 1/(15\,\pi)\,m/s$. Results on fitted values of a and f_{sat} did not depend on the precise value chosen for ϵ. Regarding the value of the fitting function at $U_{SG} = U_{SG0}$, note that this precise point is placed in the middle of the crossover region and not in the saturation region. Hence the value there is not expected to be f_{sat}.

Eq. 6.4 thus provides a prediction for the bubble generation frequency at the given values of U_{SL} and U_{SG} which is consistent with the existing theory for the linear regime [15] and saturation regime according to experimental observations [2, 3]. Specifically, for $U_{SG} \gg U_{SG0}$ it approaches exponentially the value f_{sat}, and its value is indistinguishable from f_{sat} (i.e. the difference is exponentially small) when $U_{SG} - U_{SG0} \gg \epsilon$. This is the desired behavior for this function. Summarizing, this fitting curve is designed to match the theory in the following aspects:

- (i) At $U_{SG} \ll U_{SG0}$, $f(U_{SG}) = a \cdot U_{SG}$.
- (ii) At $U_{SG} \gg U_{SG0}$, $f(U_{SG}) = f_{sat}$.
- (iii) For a given U_{SL}, V_B does not vary at low U_{SG} (see Section 7.3.1).

As a final remark for this discussion, we would like to clarify that the linear regime does not exclusively identify the bubble flow regime, just as the saturation regime does not exclusively identify the slug flow regime. Both bubble and slug flow regimes can be found indistinctly in the linear or saturation regime, depending on the ratio U_{SG}/U_{SL}. Regarding the experimental data presented in this work, most of the bubble and slug points have been found in the linear and saturation regime, respectively, although not all of them.

6.1.1 Saturation frequency

The saturation frequency has been computed for every superficial liquid velocity considered, and the asymptotic saturation values are plotted in Fig. 6.3 together with the fitting line. It is interesting to observe that a simple linear relation holds in its dependence on U_{SL}. The linear regression of the experimental data provides the fit:

$$f_{sat}(U_{SL}) = 719.6 \cdot U_{SL} + 14.4 \approx 719.6 \cdot U_{SL} \tag{6.6}$$

The value of the f_{sat}-intercept is due to experimental errors, such as the calibration of the liquid pump, as discussed in Section 4.2. Moreover, one would expect f to tend to zero when U_{SL} also does, instead of a constant value of $14.4Hz$. This value thus will not be taken into account from now on. Under that assumption, Eq. 6.6 can be newly written as:

$$f_{sat}(U_{SL}) = 719.6 \cdot U_{SL} = \frac{U_{SL}}{L_L} \tag{6.7}$$

where L_L must necessarily be the characteristic length of the volume of liquid required to generate a bubble, according with the theoretical prediction of Eq. 6.3. Consistent with the assumption that the liquid volume must be constant inside the saturation regime, L_L is then found to be $1.39 \cdot 10^{-3}\, m$, regardless of the amount of injected gas. This fact represents an interesting peculiarity of the saturation regime. More detailed information about L_L can be found in Subsection 7.4.

6.1.2 Crossover point

The crossover point was computed according to its definition for every superficial liquid velocity considered, as shown in Fig. 6.4. Points were fitted taking into account the following features:

- (i) At large values of U_{SL}, U_{SG0} tends to a finite value different to zero. Otherwise, a would behave in a different way than observed in the experiments.
- (ii) At very low values of U_{SL}, f_{sat} tends to zero and a to a constant value. Thus U_{SG0} tends to zero as well (Eq. 6.5).

The proposed fitting curve for the variation of the crossover point with U_{SL} is:

$$U_{SG0}(U_{SL}) = 3.25 \left(0.01 + (U_{SL} - 0.01) exp\left(-\frac{U_{SL} - 0.01}{0.18}\right)\right) \tag{6.8}$$

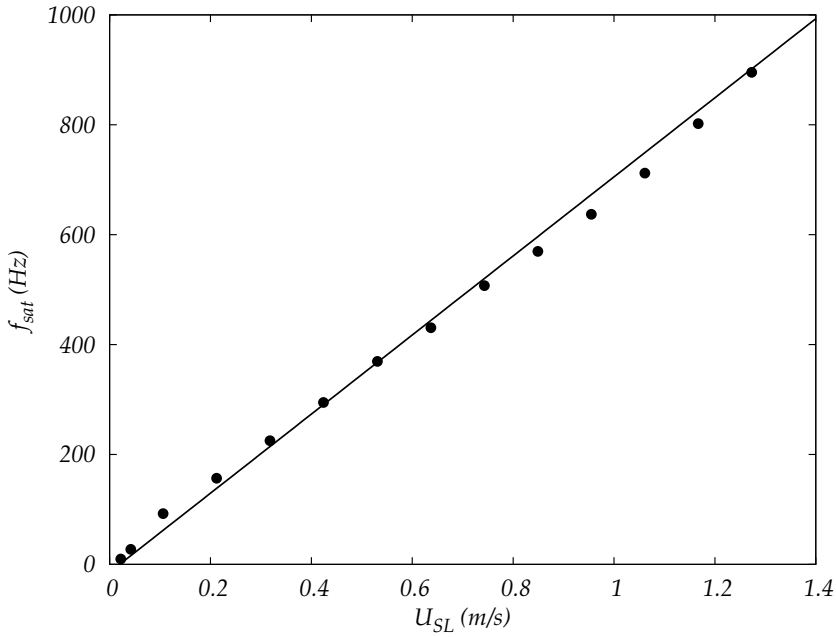

Figure 6.3: Saturation frequency as a function of the superficial liquid velocity. *Symbols:* experimental data, *line:* linear fit (Eq. 6.6).

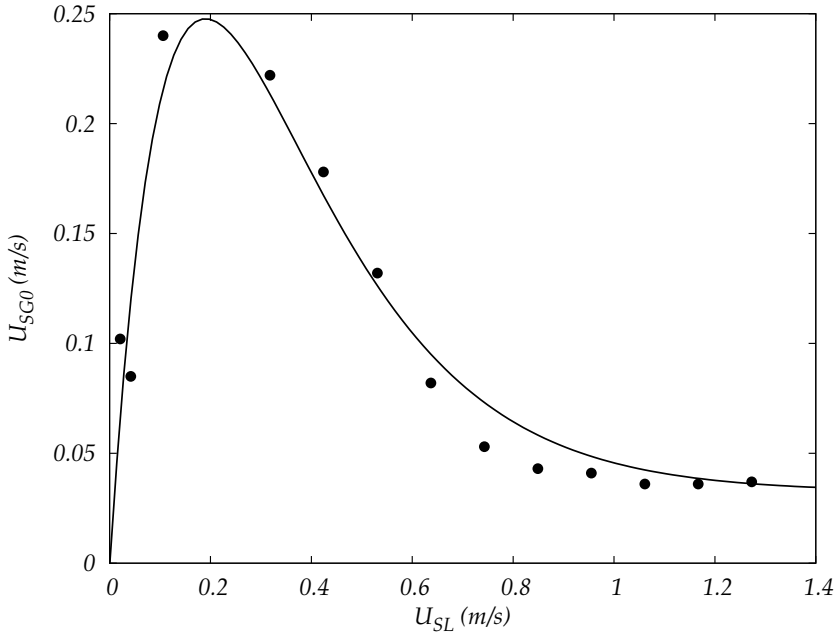

Figure 6.4: Crossover point as a function of the superficial liquid velocity. *Symbols:* experimental data, *line:* fit (Eq. 6.8).

which has also been plotted in Fig. 6.4. This fitting curve tends to a horizontal asymptote $U_{SG0} = 0.0325\,m/s$ at large U_{SL} values. Eq. 6.8 thus provides an estimation of the boundary between linear and saturation regions. As can be seen by comparing Fig. 6.1 and Fig. 6.4, the linear region is smaller than the saturation region, and therefore, most of the experiments performed in this work belong to the latter region. It is interesting to note that when working with values of U_{SG} above the maximum value shown in Fig. 6.4, it would only be necessary to control the value of U_{SL} to accurately obtain the desired bubble generation frequency for a given U_{SG}.

6.1.3 Initial slope of the linear regime

6.1.3.1 Fitting of the initial slope

The initial slope of the linear regime obtained from experimental data in Fig. 6.1 is shown in Fig. 6.5. Combining Eqs. 6.6 and 6.8 with

$$a(U_{SL}) = \frac{f_{sat}(U_{SL})}{U_{SG0}(U_{SL})} \tag{6.9}$$

we obtain the fitting curve shown in that figure. Both the experimental points and the fit show an exponential behavior at low superficial liquid velocities which turns to a linear tendency for higher U_{SL}. This linear asymptotic tendency, which is also shown in the figure, can be expressed by (in the Fig. 6.5 units)

$$a_{asympt}(U_{SL}) = 22141.5 \cdot U_{SL} - 444.4 \approx 22141.5 \cdot U_{SL} \tag{6.10}$$

Again, the value of the ordinate at the origin must be due to inaccuracies of the experimental apparatus, since a negative value of a has no physical meaning.

6.1.3.2 Theoretical considerations

In addition to the fitting, we obtain another expression of a based on theoretical considerations. From previous reasoning, we assume that

$$V_B = \frac{1}{a^*} = \frac{A}{a} \Rightarrow a = \frac{A}{V_B} \tag{6.11}$$

which leads to,

$$a = \frac{\pi(\phi_c)^2/4}{\pi(\phi_B)^3/6} = \frac{3}{2\,\phi_c\,\bar{\phi}_B^3} \Rightarrow \bar{a} = \frac{3}{2}\frac{1}{\bar{\phi}_B^3} \tag{6.12}$$

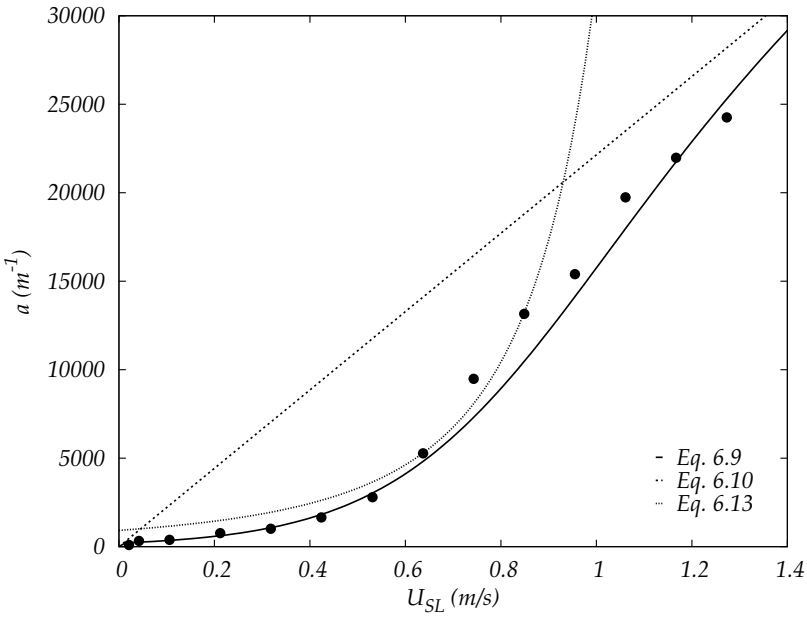

Figure 6.5: Initial slope at the linear region as a function of the superficial liquid velocity. *Symbols:* experimental data, *lines:* fit (Eq. 6.9), asymptotic tendency (Eq. 6.10), and theoretical prediction (Eq. 6.13).

where ϕ_B is the bubble equivalent diameter to a sphere, and both a and ϕ_B are normalized with the capillary diameter. Taking into account the prediction of ϕ_B for low values of U_{SG} provided by Carrera *et al.* (see Eq. 3.39), a prediction of $\bar{a}$ arises in terms of U_{SL}, as well as other parameters, namely the liquid density, the surface tension at the interface, the capillary diameter as well as the experimental fitting values γ and We^c:

$$\bar{a} = \frac{3}{2}\left(\frac{1}{\gamma} - \frac{1}{2\gamma^2}\sqrt{\frac{We_{SL}}{We^c}}\right)^{-3} = \frac{3}{2}\left(\frac{1}{\gamma} - \frac{U_{SL}}{2\gamma^2}\sqrt{\frac{\rho_L \phi_c}{We^c \sigma}}\right)^{-3} \tag{6.13}$$

Eq. 6.13 in its non-normalized form has also been plotted in Fig. 6.5, in order to be compared with the fitting gives by Eq. 6.9. For this purpose, values of $We^c = 10$ and $\gamma = 0.85$ were used, which are in agreement with the experimental values found (see Subsection 7.3.1.2).

The main disagreement with the fitting provided by Eq. 6.9 arises for large values of U_{SL}, so that the prediction of Eq. 6.13 is no longer valid from $U_{SL} \gtrsim 0.9$ m/s. This divergence occurs as a consequence of considering γ as a constant. In a more realistic approach and for larger values of U_{SL}, bubbles do not tend to fill the capillary during the generation process due to the also larger F_D. This

causes γ to decrease, which would also decrease the actual value of a.

This prediction is otherwise very sensitive to its fitting parameters, We^c and γ. This fact explains the discrepancy when U_{SL} tends to zero. In any case, Eq. 6.13 provides a good prediction of a within its range of validity. Additionally, Eq. 6.13 can be combined with Eq. 6.1 in order to provide a new prediction of f for the linear regime, relating it to the superficial liquid velocity, the physical parameters involved and the channel diameter:

$$f(U_{SG}, U_{SL}) = f_{sat} - \frac{3 \cdot \phi_c}{2} \left(\frac{1}{\gamma} - \frac{U_{SL}}{2\gamma^2} \sqrt{\frac{\rho_L \phi_c}{We^c \sigma}} \right)^{-3} \cdot \\ \cdot \epsilon \cdot Ln \left(1 + exp \left(\frac{U_{SG0} - U_{SG}}{\epsilon} \right) \right) \tag{6.14}$$

6.2 Dimensionless generation frequency

A particularly interesting approach is to obtain an expression of f in a dimensionless form by introducing the Strouhal number into the analysis. To this end, St must be defined by using the bubble generation frequency, the capillary diameter, and the actual gas velocity, i.e. $St = f \cdot \phi_c / U_G$.

Introducing Eq. 6.2 and Eq. 5.2 into the definition of the Strouhal number, we obtain:

$$St = \frac{f \cdot \phi_c}{U_G} = \frac{\phi_c}{L_{LS}} \frac{U_{SL}}{U_G} = \frac{\alpha}{\bar{L}_{LS}} \frac{U_{SL}}{U_{SG}} \tag{6.15}$$

where L_{LS} has been normalized in turn with ϕ_c. Taking into account Eq. 5.3 from the drift flux model, a simple dimensionless expression can be achieved to predict the frequency of generation:

$$St = \frac{1 - C_0 \, \alpha}{C_0 \, \bar{L}_{LS}} \tag{6.16}$$

6.2.1 Saturation regime

When introducing L_{LS}=L_L in Eq. 6.16, we impose the conditions that exist inside the saturation regime. In this case Eq. 6.16 can be particularized as follows:

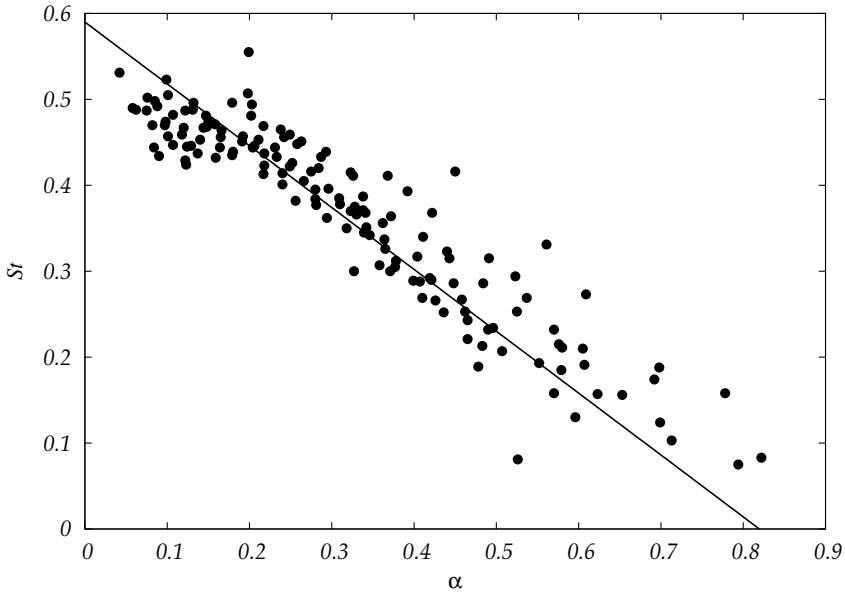

Figure 6.6: Strouhal number vs. the mean void fraction for the saturation regime. *Symbols:* experimental data from the saturation regime, *line:* prediction of Eq. 6.18.

$$St = \frac{1 - C_0\,\alpha}{C_0\,\bar{L}_L} \tag{6.17}$$

Assuming a mean value of the void fraction coefficient distribution of 1.22, accordingly to experimental observations (see Section 5.3), and the value of $\bar{L}_L$=1.39 (see Subsection 6.1.1), we obtain the next expression of St for our experiments:

$$St = 0.59\,(1 - 1.22\,\alpha) \tag{6.18}$$

St as a function of the mean void fraction is plotted in Fig. 6.6. Both St and α have been calculated using the values of f, U_G and U_{SG} measured in the experiments. For the sake of clarity, only points corresponding to the saturation regime have been plotted in that figure, omitting the ones corresponding to the linear region. The line corresponds to Eq. 6.18, which properly predicts the tendency of the experimental points. As previously noted in Subsection 6.1.2, the range occupied by the linear region is smaller than the saturation range, making Eq. 6.18 very suitable for most of the flows studied here, in particular for the slug flow regime.

6.2.2 Linear regime

The linear region provides lower frequencies than its corresponding saturation value for a given U_{SL}. Hence, Eq. 6.18 overpredicts the actual values in such a case. Nevertheless, we can also particularize Eq. 6.16 for the linear regime. Matching Eqs. 6.1 and 6.2, we obtain:

$$f = \frac{U_{SL}}{L_{LS}} = a \cdot U_{SG} \tag{6.19}$$

and including again the relationship between U_{SL}/U_{SG} and α, we obtain the following expression for the normalized liquid slug length in terms of the normalized initial slope, the mean void fraction and the void fraction distribution coefficient:

$$\bar{L}_{LS} = \frac{U_{SL}}{\bar{a} \cdot U_{SG}} = \frac{1}{\bar{a}} \left(\frac{1 - C_0\,\alpha}{C_0\,\alpha} \right) \tag{6.20}$$

Combining this last equation with Eq. 6.16, a new expression of the dimensionless frequency for the linear region arises:

$$St = \bar{a} \cdot \alpha \tag{6.21}$$

Fig. 6.7 shows St as a function of α in the linear regime. For a greater clarity, only the experimental values of U_{SL} corresponding to 0.46 and $0.725\,m/s$ have been plotted. Lines correspond to Eq. 6.21 for both U_{SL} values, where their corresponding experimental initial slope a has been computed by using Eq. 6.9. As can be seen, points corresponding to the linear regime are in good agreement with the prediction of Eq. 6.21.

As a final remark, the intersection point of Eqs. 6.17 and 6.21 must correspond to the crossover point for each given U_{SL}. By matching both equations, we obtain:

$$\alpha = \frac{1}{C_0\,(1 + \bar{a}\,\bar{L}_L)} \tag{6.22}$$

By including the value of $\bar{a}$ for a given U_{SL}, it is possible to obtain the mean void fraction at which the crossover point is reached. Finally, by knowing U_{SG0} by means of Eq. 6.8 for a given U_{SL}, the actual bubble velocity U_G at that exact point can also be estimated with Eq. 5.2:

$$\alpha,\ U_{SG0} \Rightarrow U_G = \frac{U_{SG0}}{\alpha} \tag{6.23}$$

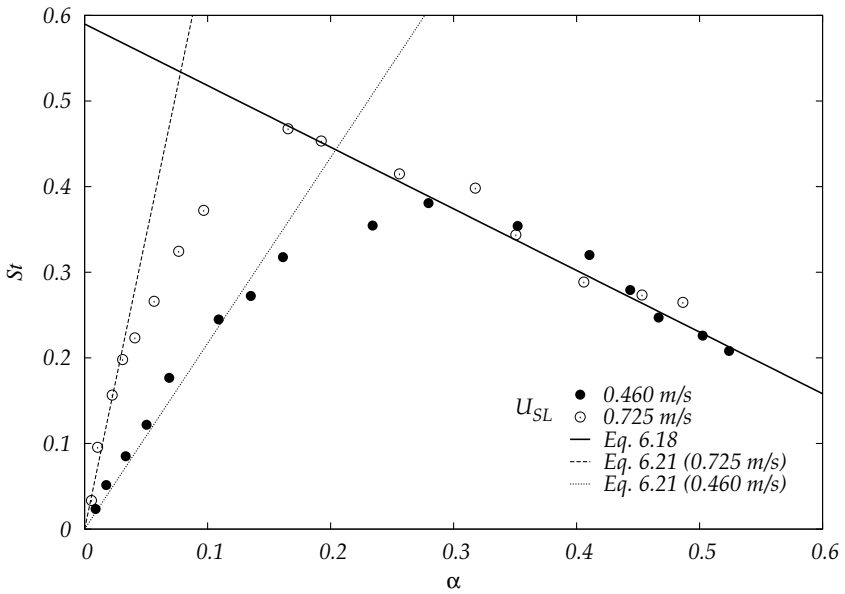

Figure 6.7: Strouhal number vs. the mean void fraction for the linear regime. *Symbols:* experimental data for U_{SL} values of 0.46 and 0.725 m/s, *lines:* predictions of Eqs. 6.18 and 6.21.

6.3 Conclusions

In this chapter we have performed an analysis of the bubble generation frequency. At different superficial gas velocities f presents a linear behavior followed by a saturation state [2, 3], showing a good agreement with existing theoretical [15].

A new expression for the bubble generation frequency at given values of U_{SL} and U_{SG} has been proposed. Fitting experimental data to this expression has allowed for the obtaining of empirical predictions for the initial slope and the saturation frequency while being consistent with the previously mentioned theoretical considerations. Results obtained confirm the linear behavior of the saturation frequency with the superficial liquid velocity. Additionally, another expression of the initial slope has been obtained using the theoretical prediction of the bubble diameter for low gas fluxes of Carrera *et al* [15]. Both expressions of a are in good agreement for liquid superficial velocities smaller than approximately 0.9 m/s. Some discrepancies arise when increasing the liquid flow rate as a consequence of considering γ as a constant through the entire analysis.

A new expression has been proposed for the crossover point between linear and saturation regimes at different superficial liquid velocities. The variation of the crossover point and the slope of the linear regime with the superficial liquid velocity has been found to present a linear asymptotic tendency. For applications in which it is important to generate a large number of small bubbles (to maximize the contact area between both phases), the optimum operation has been observed to correspond to the region of crossover to saturation.

A new dimensionless expression of the frequency based on the Strouhal number has been derived. This expression can be particularized for both the linear and saturation regions.

CHAPTER 7

Characteristic Lengths

In this chapter we analyze the geometry of the continuous and discontinuous phases in both bubble and slug flow regimes. We have focused particularly on these flow patterns due to their regular generation and small dispersion in bubble size, as previously discussed.

The classical concept of unit cell, as defined in Section 2.8, is used to identify some relevant lengths of the two-phase flow. The unit cell length is studied in Section 7.2, whereas the bubble and liquid slug lengths are analyzed in Section 7.3 and 7.4, respectively. In order to gain a better understanding, the relationships between these characteristic lengths and several parameters (such as the gas and liquid superficial velocities, bubble generation frequency and mean void fraction) are analyzed. We conclude that the unit cell and the bubble lengths can be predicted on the basis of a single relevant parameter, i.e. the mean void fraction or the Strouhal number.

7.1 Introduction

Under the hypothesis of gas flowing and filling the whole capillary cross-section, gas would occupy a cylindrical shape with no liquid film between it and the walls (see Fig. 7.1-a). With this flow structure, gas would flow without being dispersed into liquid. Assuming an uniform velocity and void fraction profiles, C_0 should be consistently equal to 1, according to Eq. 3.9, and the same velocity $U_G = U_{SL} + U_{SG}$ should appear at any radial point of each cross-section.

Figure 7.1: Bubble length when (*left*) filling the whole cross-section, and (*right*) real situation.

Following a more realistic approach, bubbles are longitudinally deformed by the liquid drag and entirely surrounded by liquid, not being in contact with the walls (see Fig. 7.1-b). In order to model the liquid film, the bubble can be approximated by a cylinder of length L_B with a cross section A_G. The actual gas-liquid interaction causes a change in the radial velocity profile. Roughly, one could approximate the radial velocity profile as constant with a value $C_0(U_{SL} + U_{SG})$ in the section occupied by gas, while tending rapidly to zero when one approaches the walls. According to this second approach, liquid velocities are significantly smaller when the liquid is close to the wall than gas or liquid velocities when flowing at the central section of area A_G. The gas volumetric quality (see Eq. 2.19) remains the same between the two cases, since the conditions of gas and liquid injection are the same.

When analyzing lengths during this Chapter, sometimes it will be desirable to analyze the simpler first case as a reference for the actual one. Henceforth, an asterisk will be used as a superscript to refer to the first case.

7.2 Unit cell

7.2.1 Dependence of the unit cell length with the generation frequency

The concept of unit cell is typically only used in slug flow. However, due to the high regularity of the bubble flow generated in the T-junction, we can define the unit cell in this regime as well. Therefore, we assume that each train of bubbles can be represented, in both bubble and slug flow regime, by a unit cell composed of one bubble and one liquid slug. Neither churn nor annular flows are suitable for applying the unit cell definition in any case.

The time spent to form a unit cell is the time between a bubble detachment and the moment in which the following bubble arises. Therefore, the bubble time formation is the inverse of the generation frequency. During this time the unit cell moves a distance L_{UC} at average velocity U_G. It has been experimentally observed that bubbles rapidly gain this velocity just after being generated, maintaining it constantly thereafter. Therefore, the transient behavior between the first steps of the bubble generation (gas entering the capillary with a velocity U_{SG}) and the bubble detachment (with a velocity U_G) can be considered negligible. The dimensionless unit cell length is then expected to be,

$$\bar{L}_{UC} = \frac{U_G}{f\,\phi_c} \tag{7.1}$$

where L_{UC} has been normalized with the capillary diameter. Assuming that both previous cases (gas filling the whole cross-section and the actual one) have the same bubble generation frequency, we deduce from Eq. 7.1 the following relationship between $\bar{L}_{UC}$ and $\bar{L}^*_{UC}$:

$$\bar{L}_{UC} = C_0\,\frac{(U_{SL}+U_{SG})}{f\,\phi_c} = C_0\,\bar{L}^*_{UC} \tag{7.2}$$

where it has been taken into account that the unit cell moves at a velocity $U_{SL}+U_{SG}$ in the first case. Being C_0 greater than 1 in conditions relevant to microgravity, as stated in Section 3.1.3, the equation above shows that the unit cell is longer in the real situation. Due to the changes in the velocity radial profile, liquid close to the capillary walls is in a quasi stagnant situation. This causes an effect equivalent to a reduction in capillary diameter, inducing larger velocities and thus larger unit cell lengths than expected in the non actual approach.

Fig. 7.2 shows the measured $\bar{L}_{UC}$ (see Subsection 2.8) as a function of $U_G/f\,\phi_c$, as well as the prediction given by Eq. 7.1. Note that $U_G/f\,\phi_c$ is the inverse of the Strouhal number, as discussed in Subsection 6.2. The unit cell length L_{UC} was calculated as the distance between the tip of two consecutive bubbles. The values of U_G and f are also extracted from the experiments. A good agreement is observed between experimental data and prediction, being valid for both bubble and slug flow regimes.

7.2.2 Dependence of the unit cell length with the mean void fraction

Taking into account Eq. 6.2, it is possible to deduce $\bar{L}_{UC}$ as a function of the gas velocity and the liquid superficial velocity as:

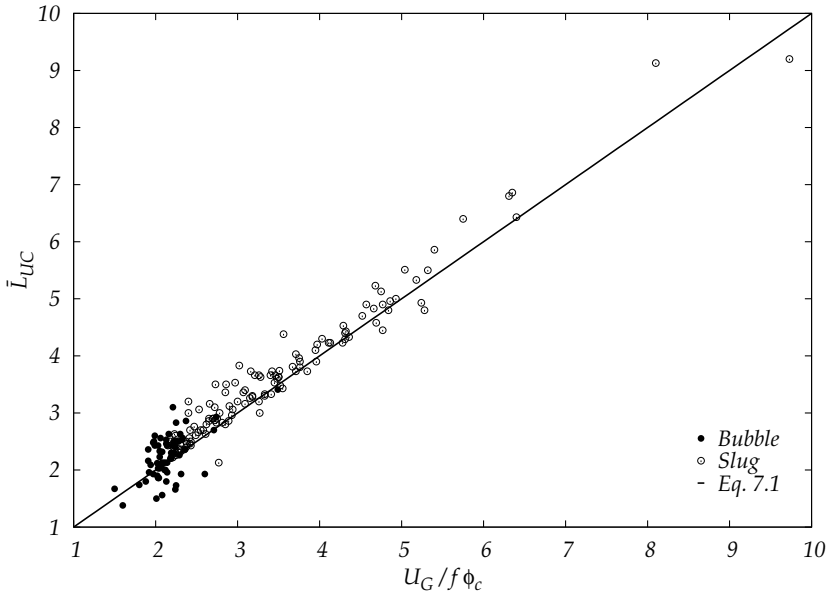

Figure 7.2: Normalized unit cell length $\bar{L}_{UC}$ as a function of $U_G / f\,\phi_c$. *Symbols:* experimental data, *line:* prediction given by Eq. 7.1

$$\bar{L}_{UC} = \frac{U_G}{f\,\phi_c} = \frac{L_{LS}}{U_{SL}} \frac{U_G}{\phi_c} = \bar{L}_{LS} \frac{U_G}{U_{SL}} \tag{7.3}$$

where L_{LS} has been normalized with the capillary diameter. Finally, by using Eq. 5.2 and Eq. 5.3, $\bar{L}_{UC}$ can be expressed in terms of just one single variable, the mean void fraction:

$$\bar{L}_{UC} = \bar{L}_{LS} \frac{C_0\,(U_{SL} + U_{SG})}{U_{SL}} = \frac{C_0\,\bar{L}_{LS}}{1 - C_0\,\alpha} \tag{7.4}$$

As can be observed from Eq. 7.4, $\bar{L}_{LS}$ and C_0 strongly determine the unit cell lengths that can be generated with our bubble generator. Eq. 7.4 offers some interesting analytical results. $\bar{L}_{UC}$ can theoretically reach an infinite value when α tends to $1/C_0$, which corresponds to the churn-annular transition [33]. Nevertheless, this last prediction could not be tested experimentally due to limitations of the experimental setup, as discussed previously in Subsection 4.2.1. Moreover, when α tends to zero, the unit cell reaches a minimum value equal to $C_0 \cdot \bar{L}_{LS}$. On the other hand, L_{LS} reaches a minimum value L_L in the saturation regime, as discussed in Section 6.1.1. For that regime, Eq. 7.4 becomes:

$$\bar{L}_{UC} = \frac{C_0\,\bar{L}_L}{1 - C_0\,\alpha} = \frac{1.7}{1 - 1.22\,\alpha} \tag{7.5}$$

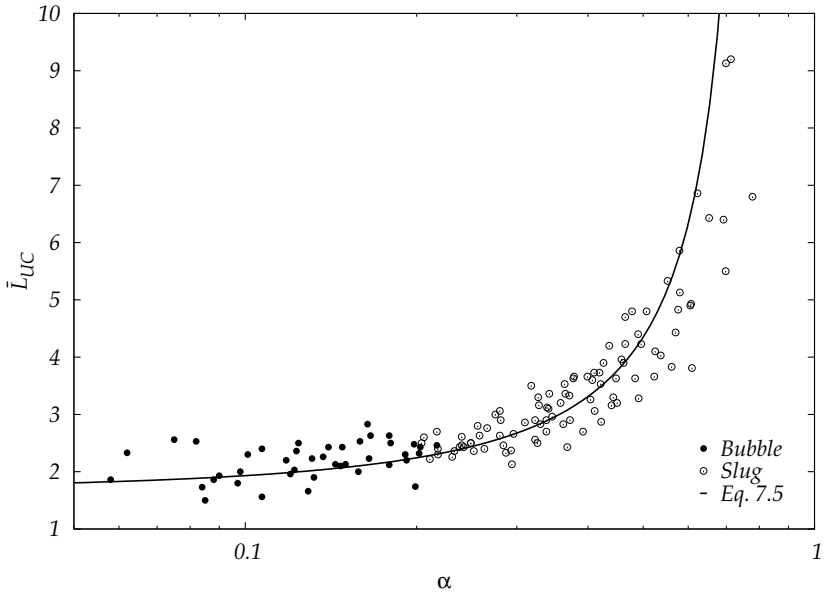

Figure 7.3: Normalized unit cell length $\bar{L}_{UC}$ as a function of the mean void fraction α. *Symbols:* experimental data, *line:* prediction given by Eq. 7.5.

where C_0 and $\bar{L}_L$ have been taken as 1.22 and 1.39, respectively, according to results in previous Chapters. Therefore, $\bar{L}_{UC}$ reaches a minimum possible value of 1.7 when the mean void fraction tends to zero.

Fig. 7.3 shows the measured values of $\bar{L}_{UC}$ as a function of the mean void fraction. According to the assumption of $L_{LS} = L_L$, only experimental data corresponding to the saturation regime are plotted in the figure. $\bar{L}_{UC}$ behavior is well predicted by Eq. 7.5. The data scattering can be justified on the basis of experimental errors associated to the experimental apparatus and the measurement of the lengths.

7.3 Bubble

7.3.1 Equivalent diameter

When bubbles grow reaching a size close to the capillary diameter, they deform longitudinally as a consequence of the increasing interaction with the capillary wall, acquiring an elongated shape within the tube. When the bubble length achieves a size several times the diameter of the capillary, bubbles acquire a cylindrical main body with a bullet-shaped nose. These bubbles are frequently

referred to as Taylor or Dimitrescu bubbles. In the case that the new boundary conditions allow it, when bubbles leave the capillary, they try to readjust to a spherical shape as a result of the surface tension action. Such a situation occurs when a train of bubbles generated in a T-junction is injected into a large enough cavity filled with quiescent fluid. Other additional phenomena can also arise. For example, given that pressure is generally lower at the capillary exit than inside the capillary, gas also tends to expand and increase in volume.

In any case, taking into account the previous assumptions of high regularity and consequently small size dispersion during the bubble generation, an equivalent bubble diameter ϕ_B can be defined for each bubble. This diameter can be estimated by means of the diameter of an equivalent sphere with the same volume:

$$Q_G = V_B\, f = \frac{\pi\, {\phi_B}^3}{6} f \Rightarrow \phi_B = \left(\frac{6}{\pi}\frac{Q_G}{f}\right)^{1/3} \tag{7.6}$$

7.3.1.1 Dependence with the gas and liquid superficial velocities

Scaling the equivalent diameter with the capillary diameter and turning Q_G to U_{SG}, a normalized expression of ϕ_B in terms of the gas superficial velocity and the generation frequency can be obtained from Eq. 7.6:

$$\phi_B = \left(\frac{6}{\pi}\frac{A\, U_{SG}}{f}\right)^{1/3} = \left(\frac{6\,\pi}{4\,\pi}\frac{{\phi_c}^3\, U_{SG}}{\phi_c\, f}\right)^{1/3} \Rightarrow \bar{\phi}_B = \left(\frac{3}{2}\frac{U_{SG}}{f\,\phi_c}\right)^{1/3} \tag{7.7}$$

$\bar{\phi}_B$ is plotted in Fig. 7.4 as a function of the superficial gas velocity. Eq. 6.4 has been used in combination with Eq. 7.7 as a prediction of the experimental data shown in this figure. The fitting of U_{SG0} (see Eq. 6.8) has also been superimposed in this figure in order to distinguish the separation between the linear and saturation regions. It is shown in this figure that bubble size increases as a function of $U_{SG}^{1/3}$, as expected. It can also be noted that bubble size reduces when increasing U_{SL}. It can be explained since increasing U_{SL} also increases drag, making easier the bubble detachment. Dimensionless sizes close to 1 are obtained, which proves that it is possible to control the bubble size accurately, getting bubbles of the order of the capillary diameter (see Section 3.3). Bubble and slug flow regimes can then be distinguished in this figure by the value $\bar{\phi}_B = 1$.

Moreover, one would expect a constant bubble size for small U_{SG} and given U_{SL}. For U_{SG} tending to zero and using Eq. 6.1, Eq. 7.7 becomes:

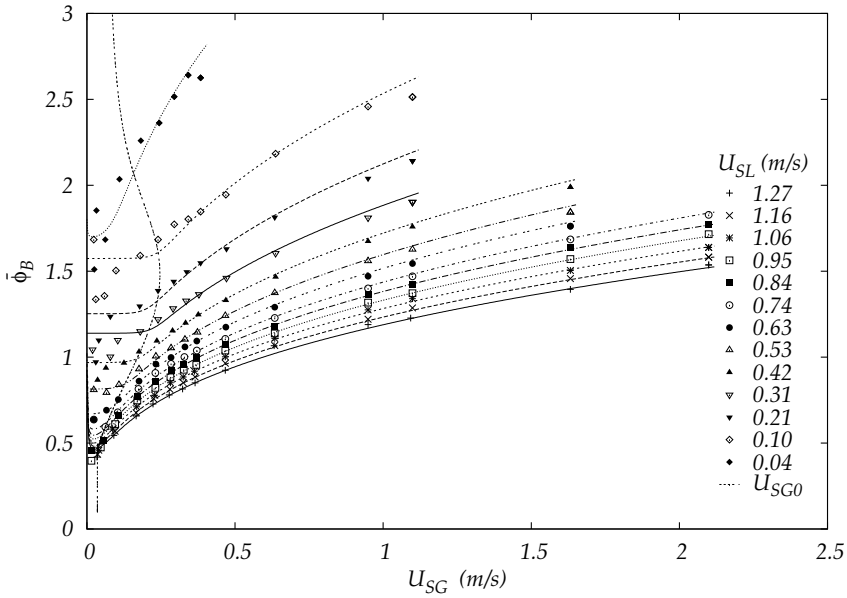

Figure 7.4: Normalized equivalent diameter $\bar{\phi}_B$ as a function of the gas superficial velocity U_{SG} for given U_{SL}. *Symbols:* experimental data, *lines:* prediction of Eq. 7.7 by using Eq. 6.4, as well as U_{SG0} from fitting of Eq. 6.8.

$$\bar{\phi}_B = \left(\frac{3}{2\bar{a}}\right)^{1/3} \tag{7.8}$$

where a is normalized with ϕ_c. The initial slope being constant for a given U_{SL}, as discussed in Subsection 6.1.3, indicates that $\bar{\phi}_B$ should also be constant. However, this tendency is not clearly observed in Fig. 7.4 due to experimental uncertainties, which are amplified in estimating $\bar{\phi}_B$ when both U_{SG} and f tend to zero.

In order to express $\bar{\phi}_B$ in terms of gas and liquid superficial velocities, Eq. 7.7 can be rewritten by using Eq. 6.2 as:

$$\bar{\phi}_B = \left(\frac{3 \cdot \bar{L}_{LS}}{2} \frac{U_{SG}}{U_{SL}}\right)^{1/3} \tag{7.9}$$

As long as most of the experimental points are inside the saturation regime as shown in Fig. 7.4, and in order to simplify what is essentially a more complex analysis, we assume the following approximation $L_{LS} \approx L_L = 1.39 \cdot 10^{-3}\, m$, which is equivalent to imposing $f \approx f_{sat}$. Under this assumption, Eq. 7.7 can be rewritten as:

$$\bar{\phi}_B \approx \left(\frac{3 \cdot \bar{L}_L}{2}\frac{U_{SG}}{U_{SL}}\right)^{1/3} = 1.28\left(\frac{U_{SG}}{U_{SL}}\right)^{1/3} \tag{7.10}$$

Fig. 7.5 shows the normalized equivalent diameter calculated with Eq. 7.7, by using the actual f measured from the experiments, as a function of the ratio of superficial velocities U_{SG}/U_{SL}. As expected, slight dispersion appears over the straight line (Eq. 7.10), corresponding these scattered data to the linear region, in which f differs from f_{sat}. Since f is lower than its corresponding f_{sat} for these points, their equivalent diameters are expected to be greater than the estimation provided by 7.10.

We show in Fig. 7.6 the normalized equivalent diameter obtained using f_{sat} (Eq. 6.6) instead of the actual f. Experimental data fit well to Eq. 7.10 in this second situation. Although Eq. 7.10 describes the behavior of $\bar{\phi}_B$ only in the saturation region, the number of experimental data in the linear region is lower than in the saturation region. In addition, the quantitative variations with data of the linear region are small. Therefore, Eq. 7.10 turn out to be a simple enough prediction for most of the flows studied in this work and is used as a general prediction hereafter for these flows.

7.3.1.2 Dependence with the Weber number

In order to check the theoretical prediction available for the slow gas flow rate regime (see Section 3.3), the normalized equivalent bubble diameter has been plotted in Fig. 7.7 as a function of the square root of the nominal Weber number of the liquid cross-flow based on the superficial velocity. It can be observed that bubble size depends linearly on ${We_{SL}}^{1/2}$, as expected. Points corresponding to the smaller gas flow rates (roughly up to 0.106 m/s) tend to superpose in the figure, which is consistent with the theoretical prediction that in this regime sizes are independent of U_{SG} and depend on ${We_{SL}}^{1/2}$ just through U_{SL}.

From the fitting of these small gas flow rate data with Eq. 3.39 we can obtain a value for the parameters of the theory, namely γ and We^c. Nevertheless, calculation of bubble sizes for small U_{SG} are again subject to larger uncertainties, and the superposition of the points is not perfect. For this reason parameter values range as follows: $\gamma = 0.86 \pm 0.06$ and $We^c = 8.64 \pm 2.2$. Line in Fig.7.7, which has been plotted as a guide to the eye, corresponds to γ=0.85 and We^c=10. Again, it is shown in Fig. 7.7 that sizes generated are values close to 1.

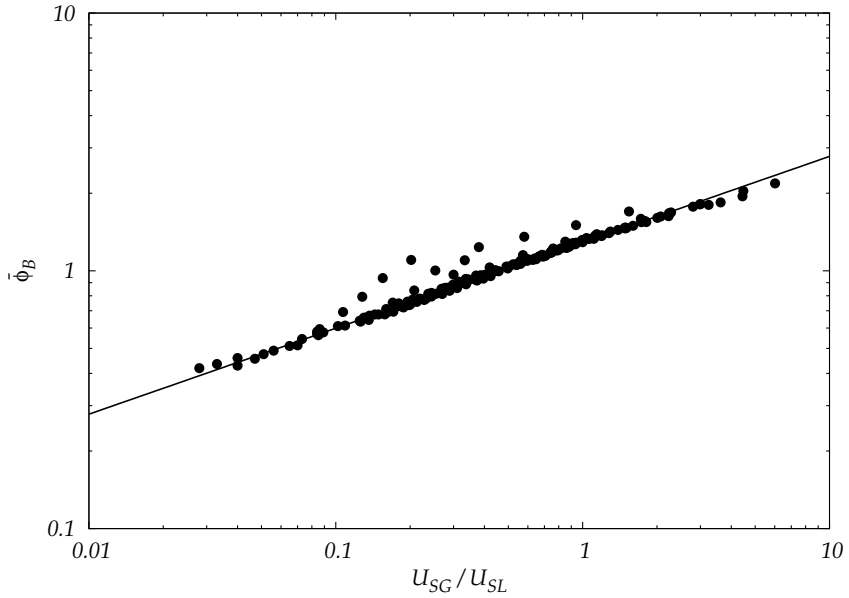

Figure 7.5: Normalized equivalent diameter $\bar{\phi}_B$ as a function of the ratio of the superficial gas/liquid velocities. *Symbols:* experimental data, *line:* prediction of Eq. 7.10.

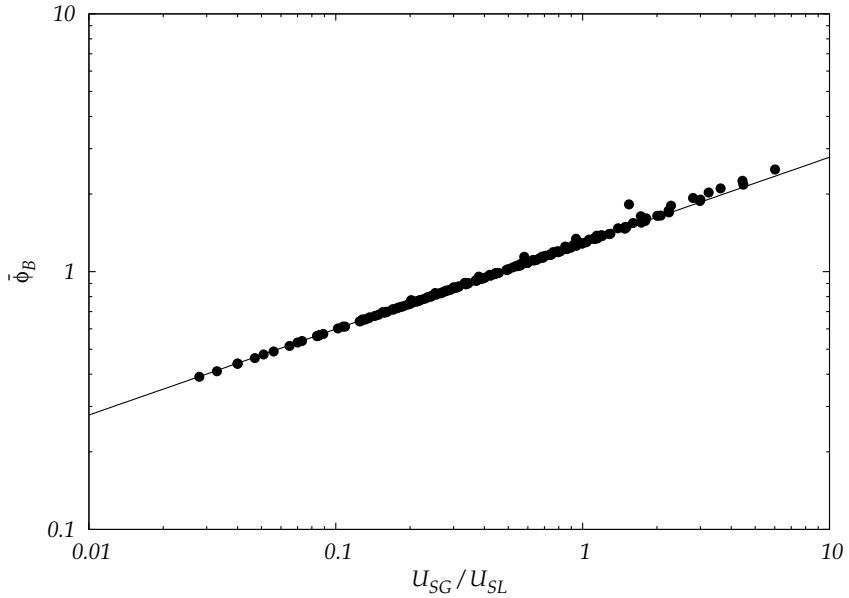

Figure 7.6: Normalized equivalent diameter $\bar{\phi}_B$ as a function of the ratio of the superficial gas/liquid velocities. *Symbols:* experimental data, *line:* prediction of Eq. 7.10.

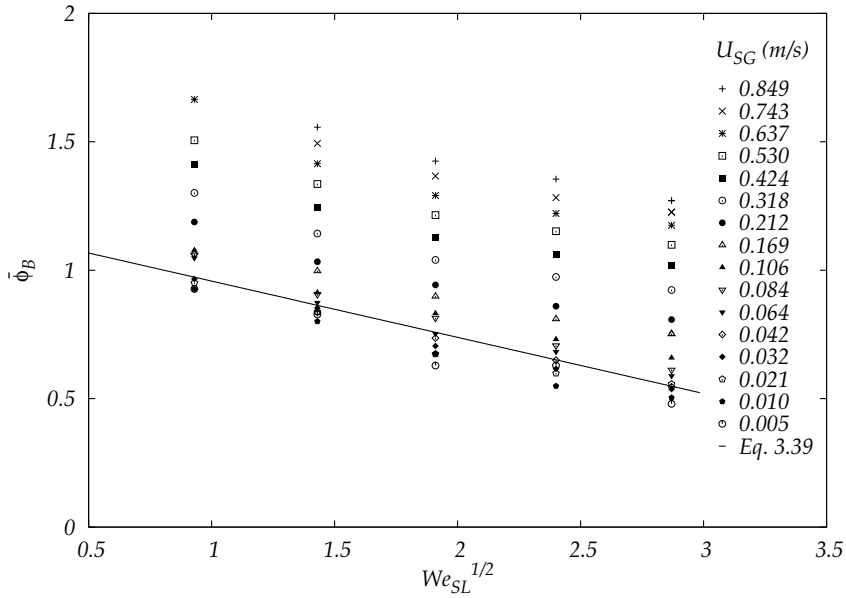

Figure 7.7: Normalized equivalent diameter $\bar{\phi}_B$ as a function of the square root of the Weber number. *Symbols:* experimental data for different U_{SG}, *line:* prediction of Eq. 3.39, with γ=0.85 and We^c=10.

7.3.2 Bubble length

7.3.2.1 Dependence with the gas and liquid superficial velocities

Once the relationship between the equivalent bubble diameter and the gas and liquid superficial velocities is known, we can look for a prediction of the actual bubble length, L_B. In order to do this, two cases must be distinguished.

In the first one, the injected gas flow rate is smaller than the liquid one, $U_{SG}/U_{SL} \ll 1$, and bubbles with an equivalent diameter smaller than the capillary diameter, $\bar{\phi}_B < 1$, are expected as shown in Fig. 7.6. This condition corresponds to the bubble flow regime. Consequently, these bubble are dispersed inside the continuous liquid, being less affected by the boundary conditions imposed by the capillary walls. It has also been observed that bubbles may be strongly deformed when the liquid drag is large enough, even for U_{SL} close to zero. As a first approximation, we assume their shape as spherical, and the hypothesis $L_B \approx \phi_B$ is adopted.

In the second case, when $U_{SG}/U_{SL} \gg 1$ bubble sizes are such that $\bar{\phi}_B > 1$ (see Fig. 7.6), their shape being strongly affected by the capillary boundary con-

ditions. We focus this second case on the slug flow regime. A crude assumption that bubbles adopt a cylindrical shape can be made, thus assuming $V_B = A\,{L_B}^*$ (see Fig. 7.1-a). Again, this scenario differs from reality, and does not take into account the liquid film around the bubble, the bubble longitudinal deformation due to the liquid drag and the local superficial distortions in its front and back parts due to the gas inertia.

Adopting the simplistic approach above in any case, and by using Eq. 7.10, we approximate the bubble length of the bubble and slug flow regimes with the following expressions, respectively:

$$\bar{\phi}_B < 1 \Rightarrow \bar{L}_B \approx \bar{\phi}_B = 1.28 \left(\frac{U_{SG}}{U_{SL}} \right)^{1/3} \tag{7.11}$$

$$\bar{\phi}_B > 1 \Rightarrow L_B^* \frac{\pi\,{\phi_c}^2}{4} = \frac{\pi\,{\phi_B}^3}{6} \Rightarrow \bar{L}_B^* = \frac{2}{3}\bar{\phi}_B^3 = 1.39 \left(\frac{U_{SG}}{U_{SL}} \right) \tag{7.12}$$

where L_B has been normalized with the capillary diameter.

For the slug flow regime, a more accurate prediction than offered by Eq. 7.12 can be obtained when considering the liquid film around the bubble. In a more realistic approach, when the bubbles are longitudinally deformed, we assume them to have a cylindrical shape as before, but with a length $L_B > L_B^*$ and a cross-section area $A_G < A$, rather than a cylinder filling the whole cross-section.

Assuming that the bubble volume remains constant in both cases, we obtain the equivalency between L_B and L_B^*:

$$L_B^*\,A = L_B\,A_G \Rightarrow \bar{L}_B^* = \bar{L}_B\,\frac{A_G}{A} = \alpha_B\,\bar{L}_B \tag{7.13}$$

where α_B is the cross-sectional void fraction in the capillary part occupied by the bubble, and both L_B and L_B^* have been normalized with the capillary diameter.

Moreover, Eq. 3.20, which is developed by Revellin *et al.* [76] for the void fraction distribution coefficient, can be rewritten as:

$$C_0 = \frac{\alpha_B\,U_{SG}}{\alpha_B\,(\alpha_B\,U_{SG} + (1-\alpha_B)\,U_{SL})} \tag{7.14}$$

which leads to,

$$C_0 = \frac{1}{\alpha_B + (1-\alpha_B)\left(\frac{U_{SL}}{U_{SG}}\right)} \tag{7.15}$$

In the slug flow regime, bubbles occupy almost entirely the cross-sectional area, being $\alpha_B \gg (1-\alpha_B)$. In addition, U_{SG}/U_{SL} is greater than 1 when the bubble length is also at least 1 or 2 times larger than the diameter of the capillary. These assumptions lead to $\alpha_B \gg (1-\alpha_S)\, U_{SL/U_{SG}}$, and therefore we assume for the slug flow regime:

$$C_0 \approx \frac{1}{\alpha_B} \tag{7.16}$$

Taking into account Eqs. 7.13 and 7.16, a more realistic prediction than Eq. 7.12 is provided by Eq. 7.17 for the slug flow regime. Again, a value of C_0=1.22 has been adopted. As was observed in the unit cell analysis (see Eq. 7.2), the modification in the velocity profile also changes the geometry of the discontinuous phase, with C_0 in charge of making the move from the hypothetical situation in which the gas fills the whole cross-section to the real one, as can be seen in the following Eq.:

$$\bar{L}_B = C_0 \cdot \bar{L}_B^* = 1.7\left(\frac{U_{SG}}{U_{SL}}\right) \tag{7.17}$$

Fig. 7.8 shows the experimentally measured lengths versus the ratio U_{SG}/U_{SG}. The three theoretical predictions of Eqs. 7.11, 7.12 and 7.17 are plotted as well.

When $U_{SG}/U_{SL} \lesssim 0.3$, bubble lengths adjust well to the prediction of spherical shapes corresponding to the bubble flow regime. The value $U_{SG}/U_{SL} = 0.3$ corresponds to bubble sizes smaller than the diameter of the capillary, which suggests that bubbles start to deform longitudinally even before reaching the size of the capillary, avoiding contact with the walls. Thus, Eq. 7.11 is not longer valid.

Moreover, for $U_{SG}/U_{SL} \gg 1$ lengths coincide with the prediction of elongated bubbles, more accurately for $\bar{L}_B$ (Eq. 7.17) than for $\bar{L}_B^*$ (Eq. 7.12). Eq. 7.17 fits the experimental values well for $U_{SG}/U_{SL} \gtrsim 2$. We observe a large region where a transition between bubbles smaller and larger than the capillary diameter arises. The actual length of the bubbles are observed to be greater than those estimated by Eq. 7.12 which underpredicts them, as expected. Eq. 7.17 also underpredicts the experimental values because neither the deformation at the front and back parts of the bubble nor the change of A_G along it were considered. In spite of that, Eq. 7.17 provides an improvement with respect to Eq. 7.12.

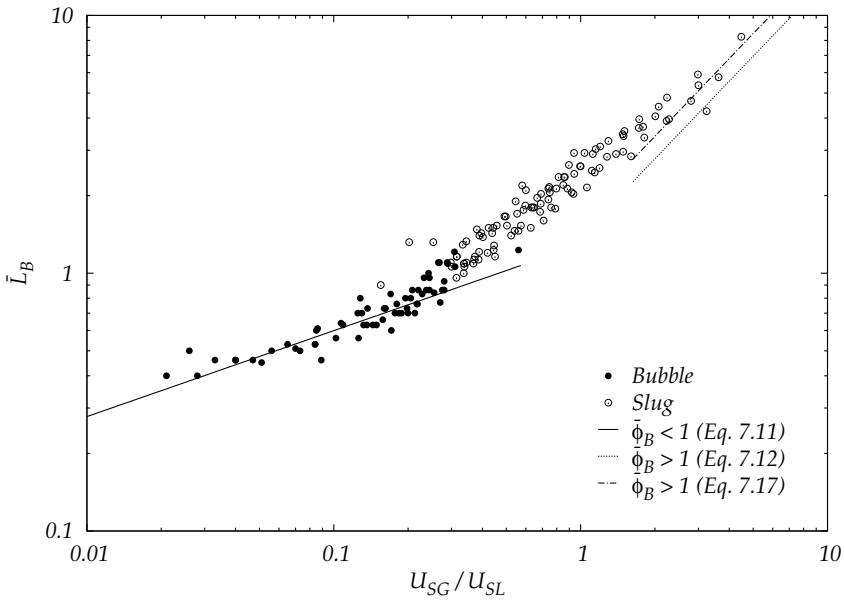

Figure 7.8: Normalized bubble length $\bar{L}_B$ as a function of the ratio U_{SG}/U_{SL}. *Symbols:* experimental data, *lines:* predictions of Eqs. 7.11, 7.12 and 7.17.

7.3.2.2 Dependence with the mean void fraction

Bubble length can be expressed in terms of only one parameter, such as the mean void fraction or the Strouhal number. Rearranging Eqs. 7.11 and 7.17 by using Eq. 3.29, we obtain a new expression for $\bar{L}_B$ for the bubble and slug flow regimes, respectively:

$$\bar{\phi}_B < 1 \Rightarrow \bar{L}_B \approx \bar{\phi}_B = 1.28 \left(\frac{C_O\, \alpha}{1 - C_O\, \alpha} \right)^{1/3} \tag{7.18}$$

$$\bar{\phi}_B > 1 \Rightarrow \bar{L}_B = C_0\, \bar{L}_B^* = 1.7 \left(\frac{C_O\, \alpha}{1 - C_O\, \alpha} \right) \tag{7.19}$$

In Fig. 7.9 the normalized bubble length is plotted versus the mean void fraction. Predictions of Eqs. 7.18 and 7.19 fit well with the experimental data, more accurately for the bubble flow regime due to the scattering of data for slug flow. This dispersion is again assumed to be a consequence of inaccuracies during the experimental data measurement.

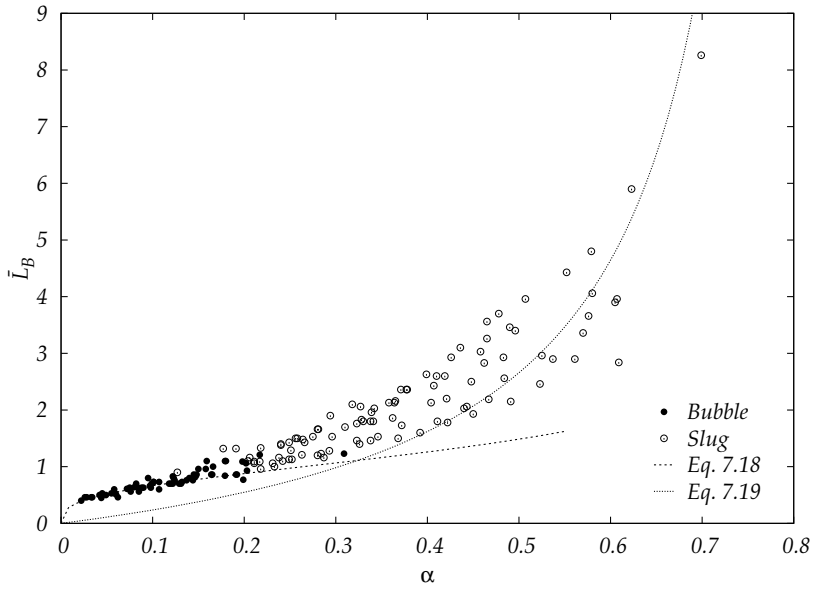

Figure 7.9: Normalized bubble length $\bar{L}_B$ as a function of the mean void fraction α. *Symbols:* experimental data, *lines:* theoretical predictions by 7.18 and 7.19.

On the other hand, taking into account the relationship between α and St expressed by Eq. 6.16, the dependence of $\bar{L}_B$ with respect to St arises:

$$\bar{\phi}_B < 1 \Rightarrow \bar{L}_B = 1.28 \left(\frac{1 - C_0 \, \bar{L}_{LS} \, St}{C_0 \, \bar{L}_{LS} \, St} \right)^{1/3} \tag{7.20}$$

$$\bar{\phi}_B > 1 \Rightarrow \bar{L}_B = 1.7 \left(\frac{1 - C_0 \, \bar{L}_{LS} \, St}{C_0 \, \bar{L}_{LS} \, St} \right) \tag{7.21}$$

7.3.2.3 Dependence with the generation frequency

When the injected gas flows filling the whole cross-section a distance L_B^* at a velocity U_{SG}, the relationship with the time required for the formation of a single bubble results:

$$\bar{L}_B^* = \frac{U_{SG}}{f \, \phi_c} \tag{7.22}$$

Again, it is crucial to include a distinction between bubbles smaller and larger than the capillary diameter. Eq. 7.17 gives the relation between $\bar{L}_B^*$ and $\bar{L}_B$ for the slug flow regime. For the bubble regime, an equivalent relationship

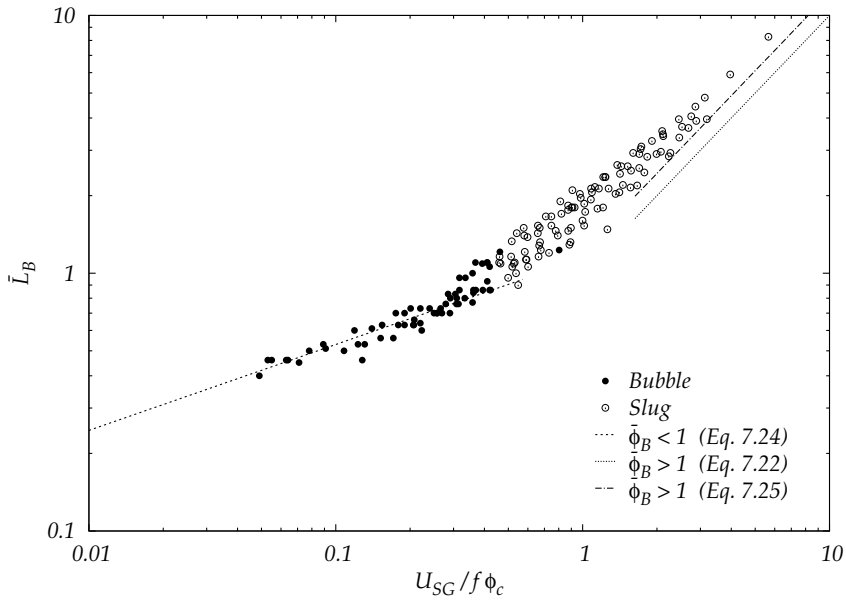

Figure 7.10: Normalized bubble length $\bar{L}_B$ as a function of the ratio $U_{SG}/f\,\phi_c$. *Symbols:* experimental data, *lines:* predictions of Eqs. 7.22, 7.24 and 7.25.

can be obtained from matching the volumes of a spherical bubble and a cylinder with volume $A \cdot L_B^*$:

$$\frac{\pi\,{\phi_B}^3}{6} = L_B^* \frac{\pi\,{\phi_c}^2}{4} \Rightarrow \bar{L}_B \approx \bar{\phi}_B = \left(\frac{3}{2}\right)^{1/3} {\bar{L}_B^*}^{1/3} \tag{7.23}$$

where the assumption $\bar{L}_B \approx \bar{\phi}_B$ has been taken into account again as discussed in Subsection 7.3.2.1. Eq. 7.22 then becomes for the bubble flow:

$$\bar{\phi}_B < 1 \Rightarrow \bar{L}_B = \left(\frac{3}{2}\right)^{1/3} \left(\frac{U_{SG}}{f\,\phi_c}\right)^{1/3} \tag{7.24}$$

On the oder hand, considering again the assumption $\bar{L}_B = C_0 \cdot \bar{L}_B^*$ discussed in Subsection 7.3.2.1, Eq. 7.22 then becomes for the slug flow:

$$\bar{\phi}_B > 1 \Rightarrow \bar{L}_B = C_0 \left(\frac{U_{SG}}{f\,\phi_c}\right) \tag{7.25}$$

In Fig. 7.10, the normalized actual bubble lengths are plotted as a function of $U_{SG}/f\,\phi_c$, where both U_{SG} and f were measured from the experiments. Predictions of Eqs. 7.22, 7.24 and 7.25 are plotted as well. Eq. 7.25 provides a better prediction than Eq. 7.22, as expected. A transition between predictions given by

Eqs. 7.24 and 7.25 is observed for values of about $0.4 \lesssim U_{SG}/f\,\phi_c \lesssim 3$.

Furthermore, an interesting result relating the initial slope in the linear regime a and $\bar{L}_B^*$ can be derived from Eq. 7.22. Taking into account the assumption of linear region for low gas fluxes provided by Eq. 6.1, Eq. 7.22 can be rewritten as:

$$\bar{L}_B^* = \frac{1}{\bar{a}} \tag{7.26}$$

Once again, distinguishing between bubble and slug flow regime and using their respective equivalences between $\bar{L}_B^*$ and $\bar{L}_B$, Eq. 7.26 can be expressed for both cases as, respectively:

$$\bar{L}_B = \left(\frac{3}{2}\right)^{1/3} \left(\frac{1}{\bar{a}}\right)^{1/3} \tag{7.27}$$

$$\bar{L}_B = C_0 \frac{1}{\bar{a}} \tag{7.28}$$

Together with the fitting of a given by Eq. 6.9, Eqs. 7.27 and 7.28 provide a prediction of the minimum L_B reachable for a given U_{SL}.

7.3.2.4 Liquid film thickness

In order to complete the analysis of the geometry of bubbles, we also propose here a rough estimation of the liquid film thickness δ for the slug flow regime. Since

$$\alpha_B = \frac{A_G}{A} = \frac{{\phi_B}^2}{{\phi_c}^2} \Rightarrow \bar{\phi}_B = \sqrt{\alpha_B} \tag{7.29}$$

the next expression can be achieved:

$$2\,\delta = \phi_c - \phi_B = \phi_c\,(1 - \sqrt{\alpha_B}) \Rightarrow \bar{\delta} = \frac{1 - \sqrt{\alpha_B}}{2} \tag{7.30}$$

where both ϕ_B as well as δ have been normalized with ϕ_c. Unfortunately it was not possible to measure the thickness in our experiments. Being a circular channel, the lighting system produced shadowed areas right at the top and bottom part of the capillary, preventing the thickness measurements as discussed in Section 4.2.1. However, through an average $C_0 = 1.22$, α_B can be estimated to be approximatively equal to 0.82, leading to a δ value of about 47 μm. This value agrees with available experimental values found in the literature [76].

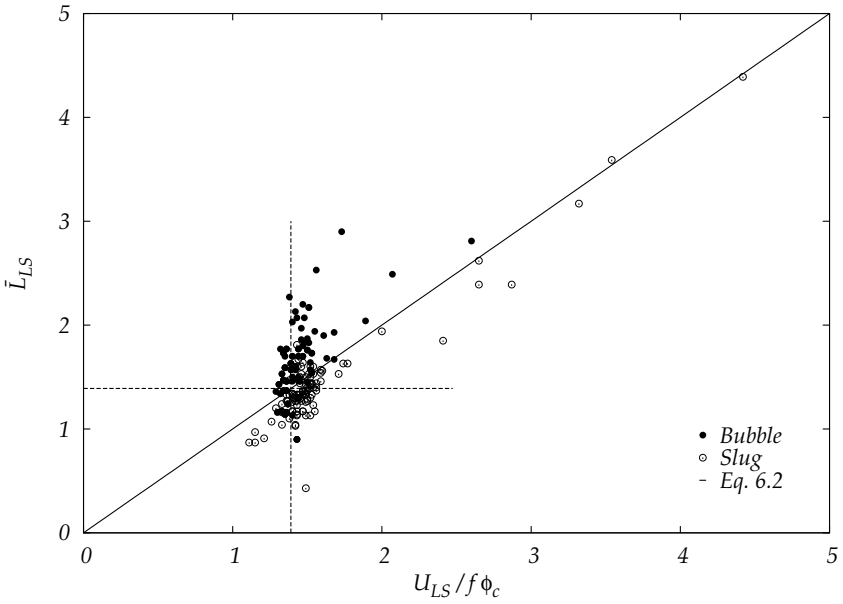

Figure 7.11: Normalized slug liquid length $\bar{L}_{LS}$ as a function of $U_{SL}/f\phi_c$. *Symbols:* experimental results, *lines:* prediction of Eq. 6.2; $\bar{L}_L = 1.39$ is also marked.

7.4 Slug of liquid

7.4.1 Dependence of the length with the generation frequency

In Fig. 7.11 the slug of liquid length (normalized with the capillary diameter) is plotted as a function of $U_{SL}/f\phi_c$. L_{LS}, U_{SL} and f have been extracted from the experiments. Two distinct behaviors can be observed: a linear tendency and a clustering around $\bar{L}_{LS} = 1.39$. When f increases from zero up to the saturation value f_{sat}, L_{LS} decreases until reaching its minimum value L_L, as discussed in Section 6.1.1. The linear tendency in Fig. 7.11 can then be identified as the linear regime shown in Section 6.1, where $L_{LS} > L_L$, and follows the behavior predicted by Eq. 6.2. The clustering must correspond to the saturation region, where $\bar{L}_{LS}$ reaches a value of $\bar{L}_L = 1.39$. This fact shows how inside this region the volume of liquid required for the formation of bubbles remains constant and equal to $A \cdot L_L$, regardless of the gas and liquid superficial velocities.

As stated before, bubble and slug flow patterns can be found in both the linear and saturation regime. Most of the fluxes observed belong to the slug flow type, explaining why there is also a greater presence of those points in the

straight line of Fig. 7.11. The observed scattering around 1.39 can be assumed to be a consequence of the difficulty when measuring the length of the liquid slug, which is sometimes strongly distorted by both the nose and the deformation of the rear part of the bubbles.

7.5 Conclusions

In this chapter, the geometry of the continuous and discontinuous phases has been studied. Along the analysis, two different situations for the bubble and slug flow patterns have been distinguished. The simplest hypothetical case in which both phases fill the whole cross-section has been studied and compared with the real case, in which the gas is dispersed into the liquid.

This study has focused on the analysis of the unit cell, bubble and liquid slug lengths, as well as on the equivalent diameter of a bubble and the liquid film thickness surrounding bubbles. The void fraction distribution coefficient, which includes the effects of both non-uniform cross-sectional velocity and void fraction distribution profiles, has been found to be the relevant parameter to understand the change from the hypothetical first case to the more realistic one.

The bubble equivalent diameter has been found to decrease linearly with the Weber number based upon the liquid superficial velocity. Furthermore, results are consistent with the prediction of independence of bubble size from gas flow rate for small fluxes. Controllable bubble equivalent diameter of the order of the capillary and reduced bubble size dispersion have been obtained. Minimum values of $C_O \cdot L_{LS}$ and $1.39 \cdot 10^{-3}\, m$ have been found for the unit cell and liquid slug, respectively.

When possible, these characteristic lengths have been related to the gas and liquid superficial velocities, the bubble generation frequency, the mean void fraction and the Strouhal number, with the intent of gaining a better understanding of their physical behavior. Finally, it has been concluded that the unit cell and bubble lengths can be expressed in terms of a single relevant parameter, such as the mean void fraction.

CHAPTER 8

Numerical simulation

In order to explore the behavior of the T-junction bubble generator in a wide range of parameters, a reliable numerical code which can complement experimental results is required. To achieve this, in this chapter we present a numerical study of the formation of mini-bubbles in a 2D T-junction by means of the fluid dynamics numerical code JADIM (see Appendix A). Numerical simulations are carried out for different flow conditions, giving rise to results on the behavior of bubble velocity, void fraction, bubble generation frequency and characteristic lengths.

In Section 8.1 a dimensional analysis of the bubble generation phenomenon is presented. The modelling of the T-junction is presented in Section 8.2. Numerical results on the characteristics of the generated flows are presented and compared to experimental data from previous chapters in Section 8.3.

8.1 Dimensional analysis of the phenomenon

The Buckingham's π theorem is used here to identify the characteristic dimensionless numbers that control bubble generation and have to be satisfied in the numerical simulations. Ten independent parameters are considered in this analysis: the gas and liquid densities (ρ_G and ρ_L, respectively) and viscosities (μ_G and μ_L, respectively), surface tension σ, capillary diameter ϕ_c (the T-junction being formed by the connection of equal size capillaries), contact angle between the capillaries and the gas-liquid interface θ (measured on the internal part of the liquid), gravitational constant g, and gas and liquid superficial velocities (U_{SG}

U_{SL}	U_{SG}	Re_{SL}	Re_{SG}	We_{SL}	We_{SG}	FP
0.106	0.242	106	24	0.16	0.81	S
0.106	0.344	106	34	0.16	1.64	S
0.318	0.081	318	8	1.40	0.09	S
0.318	0.242	318	24	1.40	0.81	S
0.318	0.337	318	34	1.40	1.58	S
0.531	0.068	531	7	3.92	0.06	B
0.531	0.236	531	24	3.92	0.77	B

Table 8.1: Superficial velocities [m/s], dimensionless numbers and flow patterns observed in each experiment.

and U_{SL}, respectively). Experiments are conducted at a constant temperature around $20°C$ as explained in Section 4.2 and the system can be assumed adiabatic. Therefore, the numerical simulation does not take into account thermal effect either.

According to the π theorem there must be seven dimensionless parameters since there are three independent physical quantities in the problem. We have selected $(\rho_L - \rho_G)/\rho_L$, θ, Bo, Re_{SL}, Re_{SG}, We_{SL} and We_{SG} as appropriate dimensionless numbers in our study, according to the definitions proposed in Section 2.7. Any other dimensionless number should be obtained from the combination of the previous ones. Typically, the Capillary number $Ca = We/Re$ is used to compare viscosity and surface tension effects at the interface.

Experiments presented in Chapters 5-7 are used as reference data for the comparison with the simulations reported here. The superficial velocities selected for the comparison with numerical simulations ranged from 0.106 to $0.531\,m/s$ for water and from 0.081 to $0.344\,m/s$ for air. We considered the following values of the physical properties: $\rho_L \simeq 10^3\ kg/m^3$, $\rho_G \simeq 1.2\,kg/m^3$, $\mu_L \simeq 10^{-3}\ Pa \cdot s$, $\mu_G \simeq 10^{-5}\ Pa \cdot s$ and $\sigma \simeq 0.072, N/m$. According to these values, we obtain $\Delta\rho/\rho \approx 1$ and $Bo = 0.13$. Shown in Table 8.1 are the values of U_{SL}, U_{SG},Re_{SL}, Re_{SG}, We_{SL}, We_{SG}, and the flow pattern observed in each experiment.

In order to carry out the numerical simulations, some changes in the values of two dimensionless parameters (Re_{SL} and Re_{SG}) had to be considered. If the values that are used are the same as those in the experiments, the method used for the calculation of the surface tension contribution in the momentum equation, the Continuum Surface Force [12], generates the appearance of spurious currents (see next Section for detailed information). These currents induce

U_{SL}	U_{SG}	Re_{SL}	Re_{SG}	We_{SL}	We_{SG}	FP
0.106	0.242	11	2	0.16	0.81	S
0.106	0.344	11	3	0.16	1.64	S
0.318	0.081	32	1	1.40	0.09	S
0.318	0.242	32	2	1.40	0.81	S
0.318	0.337	32	3	1.40	1.58	S
0.531	0.068	53	1	3.92	0.06	B
0.531	0.236	53	2	3.92	0.77	B

Table 8.2: Superficial velocities [m/s], dimensionless numbers and flow patterns observed in each numerical simulation.

vortices at the interface without any physical meaning, destabilizing the simulations and strongly distorting the interface, as reported by Dupont *et al.* [24]. Numerical instabilities produced by the spurious currents depend linearly on the ratio σ/μ. For the flow conditions considered here, gas and liquid viscosities have to be increased one order of magnitude in the simulations in order to avoid the spurious currents. Consequently, Re_{SL} and Re_{SG} have been decreased one order of magnitude for the simulated flows and both experiments and simulations correspond to Reynolds numbers in the laminar regime.

In the simulations we consider $g = 0$ (thus, $Bo = 0$), while the values of We_{SL} and We_{SG} are the same as in the experiments. We also use the same geometry of the capillaries as well as the same gas and liquid surface velocities as in the experiments. The latter was possible since the width of the capillary in the 2D simulations corresponds to the hydraulic diameter of the experimental T-junction. Under this assumption, the dimensionless analysis remains valid and the two-phase flow behavior in the simulations is expected to be similar to that which is observed in the experiments. The surface velocities and the values of Re and We, as well as the regime observed in each simulation, are shown in Table 8.2. The corresponding range of the Capillary number is Ca_{SL} =0.015 $-$ 0.074. With regard to the contact angle used in the simulations, its value is chosen in agreement with the observations of the experimental videos (See section 8.2.1).

8.2 Modelling of the T-junction

8.2.1 Mesh

Simulations are performed in a 2D domain with a 10 mm x 2 mm regular mesh. The width of the gas and liquid capillaries is 1 mm. The mesh contains 600x180

cells (see details in Fig. 8.1a-c), and a vertical diminishing is applied in order to refine the mesh around the capillaries' intersection area. The normalized size with ϕ_c in HxW of the largest and smallest cells is $1.67 \cdot 10^{-2}$ x 10^{-2} and $2.45 \cdot 10^{-5}$ x 10^{-5}, respectively.

A less refined mesh with $300x90$ cells (twice the size of those in the larger mesh) has been also tested. In this case, results did not show any significant change for most of the gas and liquid surface velocities. Differences between results obtained with each mesh are less than 0.5% in the bubble length and less than 2.3% in the bubble generation frequency. Thus, both meshes provide bubbles with similar regularity and shape. In spite of these similarities, the least refined mesh showed some numerical instabilities for the higher gas and liquid velocities studied here. On the other hand, several tests performed with meshes containing a number of cells larger than $600x180$ did not show any changes in the results.

Therefore, in this chapter we present the results obtained with the $600x180$ cells mesh. The grid convergence discussion concerning the gas thread generation at the T-junction is presented in Section 8.2.3. The simulations are performed with a time step $\Delta t = 10^{-5}$. Values of Δt in the range 10^{-4} and 10^{-6} step have been tested in oder to assure the convergence of the results since unsteady simulations are presented.

8.2.2 Boundary conditions

Results have been found to be very sensitive to the conditions imposed on the boundaries of the computational domain. These conditions are summarized in Table 8.3 for each boundary defined in Fig. 8.2.

The successful generation of bubbles relies especially on a good selection of boundary conditions associated to wall 1, since they determine the curvature of the rear interface and therefore the bubble shape. In the case of wall 1, the contact angle determines the attachment of the gas to the vertical capillary and in turn the bubble shape and size (see Fig. 8.3). Fixing a 0° contact angle results in a condition that is too restrictive, forcing the gas to remain attached at the upper side of the wall and the rear interface of the bubble to tilt back excessively in comparison with experiments. On the other hand, imposing a 90° contact angle quickly stabilizes the gas at the lower corner of the wall resulting in unrealistic interfaces.

We have used images obtained from the experiments in order to determine

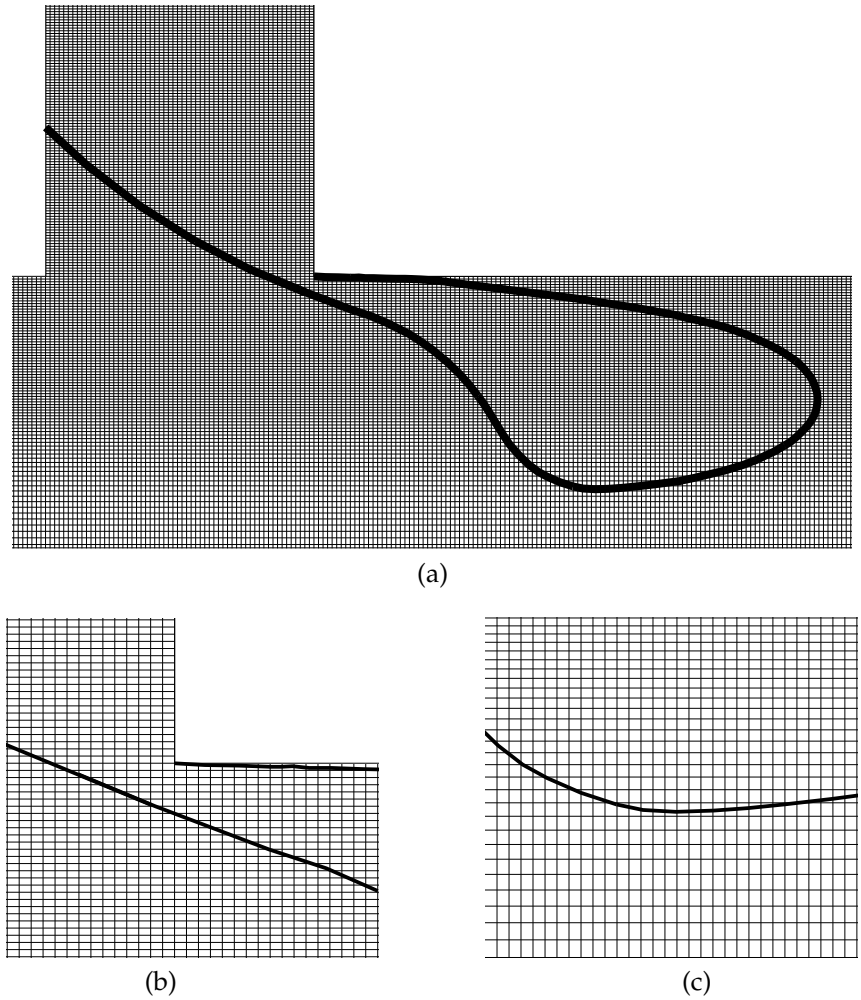

Figure 8.1: Mesh used in the simulations. Details of the mesh at *(a)* the T-junction zone, *(b)* the gas thread formation zone, and *(c)* zone at the bottom of the bubble, where the vertical diminishing can be observed. The boundary of the bubble is also plotted as a guideline to the eyes. It does not correspond to the actual thickness of the interface (of about 3 grid cells)

the appropriate contact angle to impose on wall 1 (see Fig. 8.4). The capillary curvature and the insufficient illumination at the triple point are disadvantages for the quality of the measurements, as was discussed in Subsection 4.2.1. In addition, liquid drag and gas fluctuations after the breakup of the bubble caused the contact angle to be dynamic. However, selecting a fixed value of θ=25°, we obtain a generation of bubbles whose shape is in good agreement with exper-

Wall	Boundary conditions
1	$\theta = 25°$
2	Gas inlet: imposed U_{SG}; hydrophobic: θ=180°
3	$\theta = 45°$
4	Hydrophilic $\theta = 0°$ and wettability
5	Outlet
6	Hydrophilic $\theta = 0°$ and wettability
7	Liquid inlet: imposed U_{SL}
8	Hydrophilic $\theta = 0°$ and wettability

Table 8.3: Boundary conditions imposed on the system.

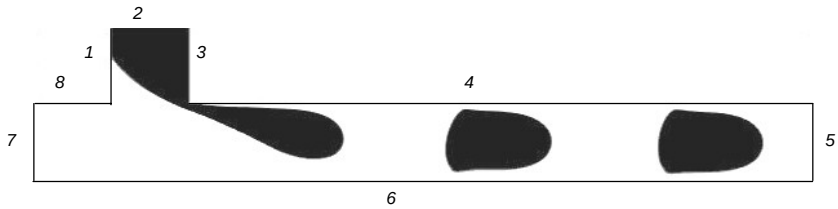

Figure 8.2: Boundaries of the system.

imental observations. We have also observed that small variations of ($\pm$15°) around the taken value do not seem to affect the results noticeably. One can observe in Fig. 8.3 the different interfaces obtained with θ=0, 25 and 90°, where the case with an intermediate value shows a more realistic shape.

Whit regards to wall 6, in order to prevent bubbles from attaching to it, hydrophilic (θ=0°) and wet boundary conditions are imposed, as well as on walls 4 and 8. Walls 2 and 7 are defined as fluid inlets and wall 5 is defined as the fluid outlet. The corresponding gas and liquid superficial velocities are thus imposed on walls 2 and 7. In addition, wall 2 is considered hydrophobic in order to avoid liquid rise 1 *mm* above the T-junction, in agreement with experimental observations. A 45° contact angle is imposed on wall 3 to force the forward inclination of the frontal interface. Nevertheless, boundary conditions on this wall did not show an impact in the results.

8.2.3 Gas squeezing

According to the experimental observations, bubble generation results from the breakup of a gas thread that develops after the T-junction. The explanation for

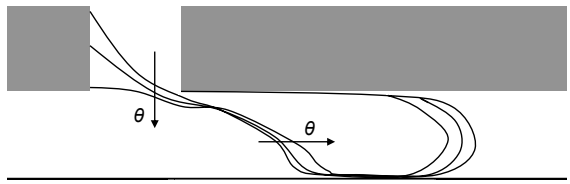

Figure 8.3: Influence of the contact angle imposed on wall 1 on the interface shape, for U_{SL}=0.318 m/s and U_{SG}=0.182 m/s. Lines correspond to the bubble contour for θ= 0, 25 and 90°.

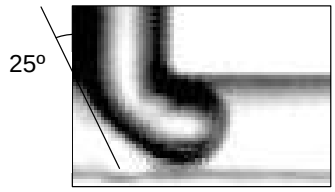

Figure 8.4: Contact angle at wall 1 measured from experimental images.

the breakup is supported by different theories. Its cause can be explained by the Plateau-Rayleigh instability [60] or by the effects of the flowing liquid from the tip of the thread to the neck where pinch-off occurs [82].

In 2D, the surface tension has a stabilizing effect and opposes any deformation of the interface tending to create a bubble. This is in agreement with our simulations since no natural pinch-off has been observed for the range of parameters covered by our study. An example is shown in Fig. 8.5 where a long thread of gas generated after the T junction is clearly observed. It is found to be very stable and remains after the bubble exits the computational domain. In addition, the thread width has also been found to be grid independent when refining the grid.

In order to be able to generate bubbles in 2D geometry, an artificial gas squeezing mechanism has been introduced in JADIM. It consists of the removal of the gas cells in the zone where the gas thread reaches a minimum thickness,

Figure 8.5: Thread generation without squeezing. U_{SL} = 0.318 m/s and U_{SG} = 0.182 m/s.

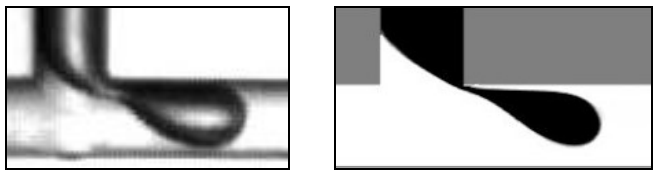

Figure 8.6: Comparison of the thread just before being squeezed in *(a)* experiments and *(b)* numerical simulations.

at a time when the sign of the interface curvature changes. This is in agreement with experimental observations which show that at this point the 3D instability squeezes the thread. The bubble thread before squeezing in experiments *(a)* and numerical simulations *(b)* is shown in Fig. 8.6. The gas volume lost under the application of the artificial squeezing mechanism in the simulations is about a few grid cells and is considered to be negligible compared to the bubble volume.

After squeezing, the geometry of the injected gas jet is naturally adjusted as a result of the action of surface tension, generating the appropriate initial conditions for the following bubble. Although the initial geometry of the gas jet in the simulations have a strong influence on the first generated bubble, it does not seem to have any influence on successive bubbles. The second generated bubble has the same size as the following ones, fixing the periodicity of the process. Thus, we can conclude that the initial geometry of the gas jet does not play any significant role in the generation of a train of bubbles. This turns out to be an essential feature of the numerical simulations, since no theoretical predictions or experimental data on the initial geometry are available.

8.3 Results and discussion

A set of seven numerical simulations have been performed by means of JADIM. We have used the same injection conditions (liquid and gas superficial velocities) as in the experiments. Tables 8.1 and 8.2 show the injection conditions as well as the observed flow patterns in the experiments and simulations, respectively. Simulations successfully reproduce different trains of bubbles (see comparison with experiments in Figs. 8.7-8.9, in which the process of generation of a single bubble is shown in each case), obtaining a regular periodicity in the bubble generation and regularity in bubble size, as is discussed in Sections 8.3.2 and 8.3.3, respectively. As can be observed, the time required for the formation of a bubble is shorter in the numerical simulations than in the experiments, which is discussed in Section 8.3.2.

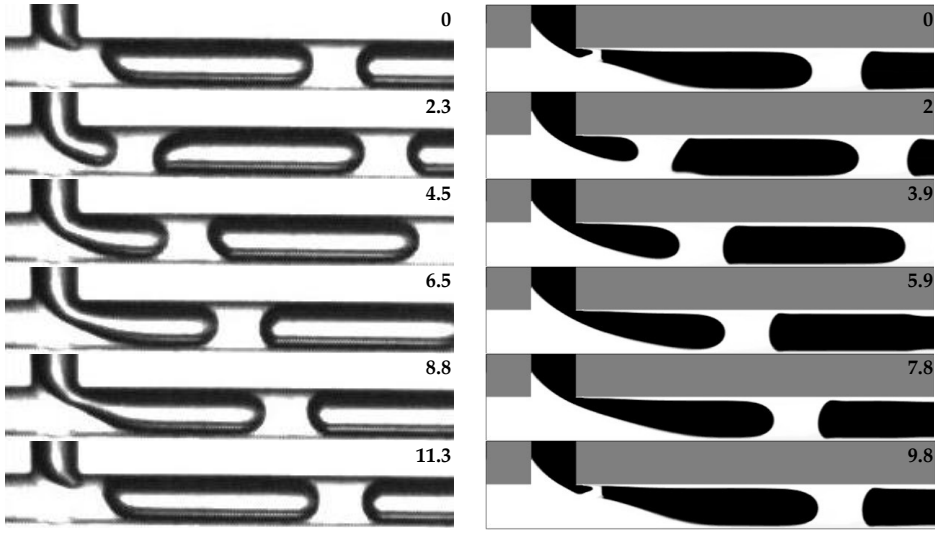

Figure 8.7: Slug flow close to the slug-churn transition in (*left*) experiments and (*right*) numerical simulations. $U_{SL} = 0.106\ m/s$ and $U_{SG} = 0.344\ m/s$. Time (ms) is indicated in the upper right corner.

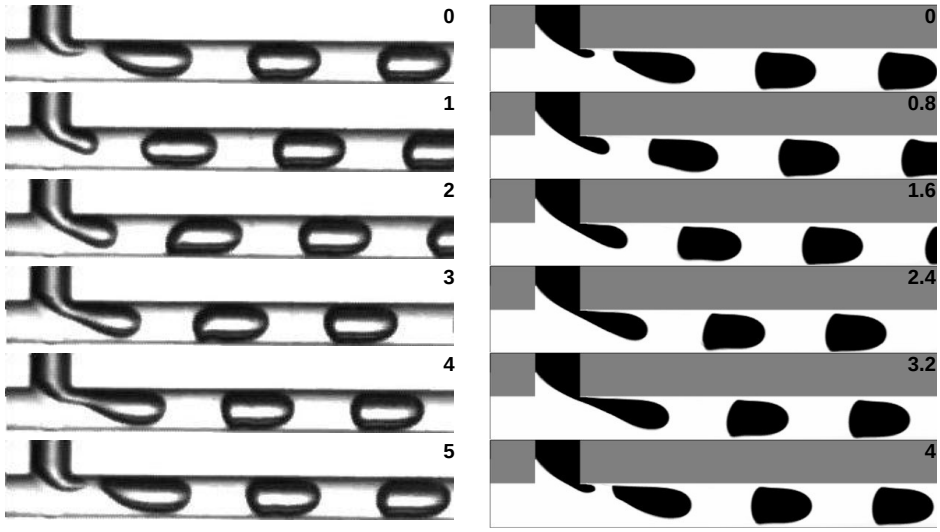

Figure 8.8: Slug flow in (*left*) experiments and (*right*) numerical simulations. $U_{SL} = 0.318\ m/s$ and $U_{SG} = 0.242\ m/s$. Time (ms) is indicated in the upper right corner.

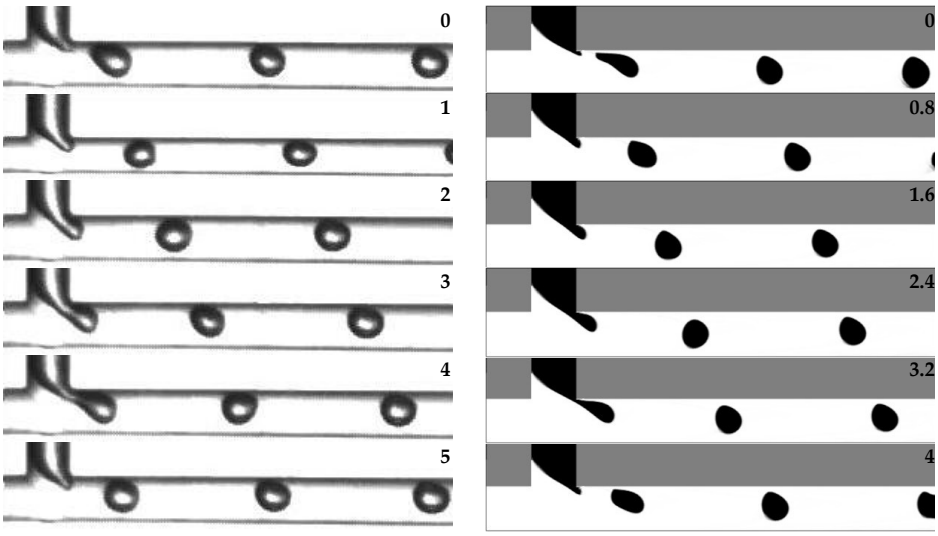

Figure 8.9: Bubble flow in (*left*) experiments and (*right*) numerical simulations. $U_{SL} = 0.531\ m/s$ and $U_{SG} = 0.068\ m/s$. Time (ms) is indicated in the upper right corner.

Both bubble and slug flow patterns, defined as explained in Subsection 4.2.1, are observed in the simulations. For a given U_{SG} and small values of U_{SL} such as those proposed here, a marginal churn pattern has also been observed in the experiments (see Section 5.2), but it is not considered in this numerical study. We did not expect to observe annular or stratified flow patterns, due to the small values of U_{SG} and the capillary diameter (see Eq. 3.27), respectively.

Fig. 8.7 shows a slug flow obtained with U_{SL}=0.106 m/s and U_{SG}=0.344 m/s. Slightly increasing the value of U_{SG} would cause the flow to enter into the slug-churn transition region. Figs. 8.8 and 8.9 show examples of slug and bubble flows obtained with U_{SL}=0.318 m/s and U_{SG}=0.242 m/s, and U_{SL}=0.531 m/s and U_{SG}=0.068 m/s, respectively. Clear similarities in the bubble shape in both patterns in experiments and numerical simulations can be observed. Bullet-shaped bubbles rounded at the front and flattened at the rear are simulated in the slug flow. Bubbles generated in the bubble flow regime are deformed as a consequence of being longitudinally dragged by the continuous phase. Experimentally observed fluctuations at the back of the bubbles are reproduced, following the breakup of the gas thread and the subsequent action of surface tension to reduce the interface. It has been also observed that the bubbles have the tendency to stay at the capillary centerline, which confirms that buoyancy

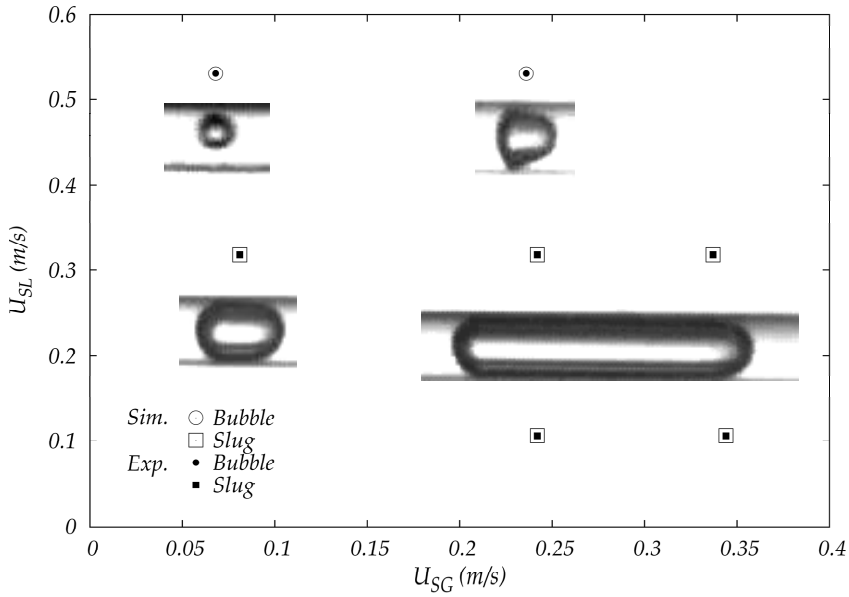

Figure 8.10: Flow pattern map obtained from experimental and numerical data.

does not play any role in our numerical simulations.

A flow pattern map obtained from the experimental and numerical data is shown in Fig. 8.10. The same flow regimes are obtained in experiments and numerical simulations when the same superficial velocities are used.

8.3.1 Bubble velocity and void fraction

We estimate the bubble velocity in simulations, as well as in experiments as explained in Subsection 4.2.1, from the measurement of the displacement of the front part of the bubble and the time employed in this displacement.

Fig. 8.11 shows the bubble velocity as a function of the mixture superficial velocity. A linear behavior can be observed in both the experiments and the numerical simulations, according to the drift-flux model (see Eq. 5.1).

Concerning 2D channel flows, the same trends as explained in Section 3.1.3.2 are expected for C_0. For laminar flows, the inviscid numerical solution reveals that C_0=1.4 [65] and Navier Stokes simulations for laminar flow but in the limit of both large Reynolds and Capillary numbers gives C_0=1.37 [29]. This is in

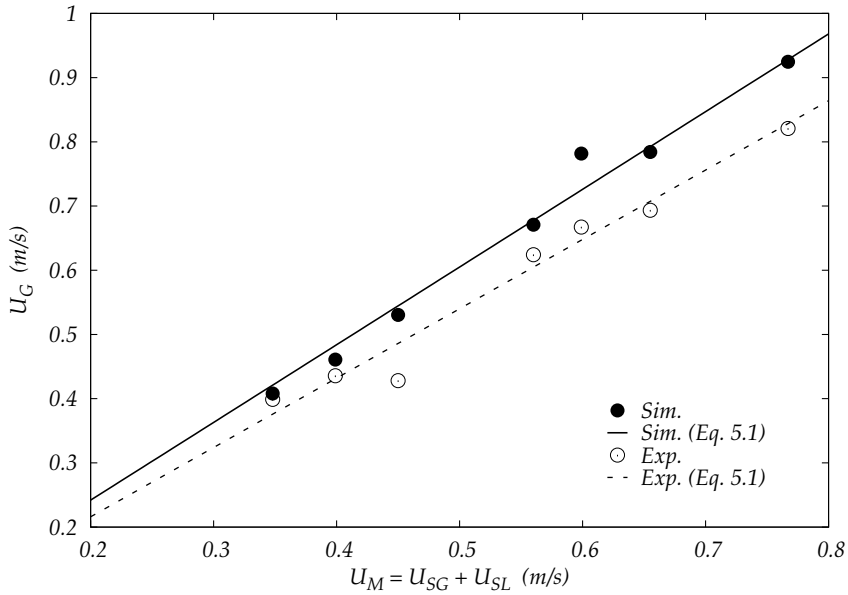

Figure 8.11: Bubble velocity as a function of the mixture superficial velocity. *Symbols:* experimental and numerical data. *Lines:* linear fittings of experimental and numerical data (Eq. 5.1).

agreement with the consideration of Nicklin *et al.* [66] that predicts C_0=1.5 for the laminar channel flow. The opposite limit for small Reynolds and Capillary numbers is C_0=1.

Fitting the simulation data gives a slope C_0=1.21, which agrees with the value reported in the literature since C_0 is expected to range from 1 to 1.4 in 2D. The fitting of the experimental data shown here gives a slope C_0=1.08 which is also in agreement with previously reported results in channels.

Figure 8.12 shows the mean void fraction as a function of the ratio between gas and liquid superficial velocities. The mean void fraction is estimated as in the experiments by means of Eq. 5.2. The theoretical prediction given by Eq. 5.3 is plotted for both experimental and numerical simulations data by using their respective C_0. The behavior of the void fraction obtained in the simulations reproduces the experimental behavior and coincides with the theoretical prediction. In agreement with the slightly larger U_G observed in simulations in comparison with experiments in Fig. 8.11, one can observe smaller void fraction values in the simulations than in the experiments in Fig. 8.12.

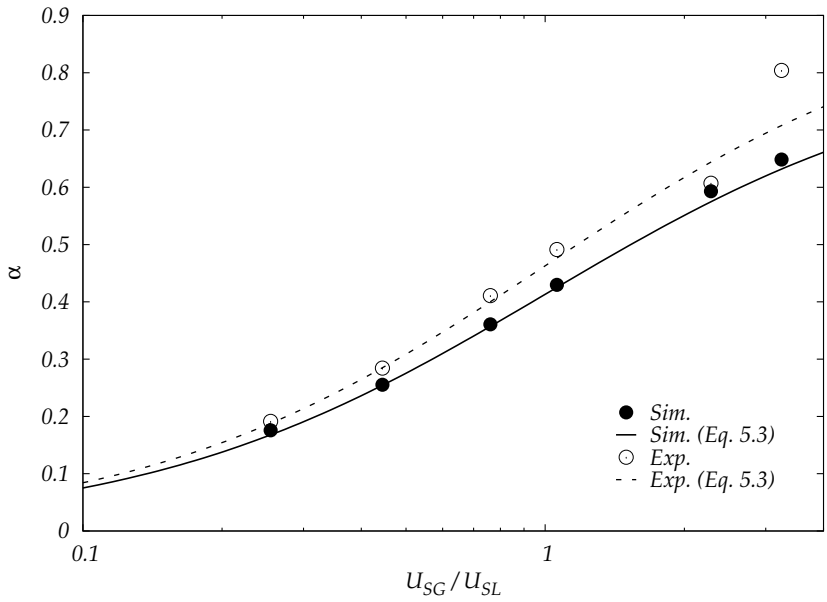

Figure 8.12: Void fraction as a function of the ratio between gas and liquid superficial velocities. *Symbols:* experimental and numerical data. *Lines:* theoretical prediction given by Eq. 5.3.

8.3.2 Bubble generation frequency

In order to ensure regularity in the formation of bubbles, we have generated trains of bubbles containing at least four of them. The generation frequency has been estimated by measuring the time required to generate these bubbles. The first bubble of each train, which is strongly dependent on the initial geometry as previously remarked, is not considered.

Fig. 8.13 shows the bubble frequency as a function of the superficial gas velocity at U_{SL}=0.106, 0.318 and 0.531 m/s for both experimental and numerical simulation data. Lines correspond to the fitting of the experimental data, shown in Section 6.1. It can be observed that frequency increases with the superficial liquid velocity. For each U_{SL} the simulations reproduced the behavior observed in the experiments when U_{SG} was changed: a nearly linear regime at small U_{SG}, and a zone with constant frequency at large U_{SG}.

Although the simulation data are qualitatively very similar to the experimental results, it can be observed that frequency values are always slightly larger in the simulations. This is associated to the observation of smaller bubbles in the simulations. This discrepancy could be explained by the fact that simulations

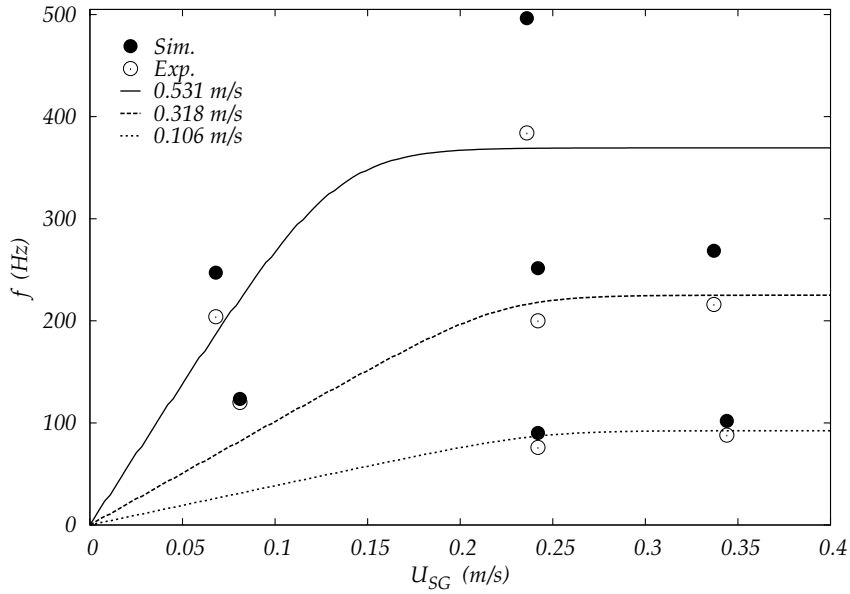

Figure 8.13: Bubble frequency as a function of the superficial gas velocity for different superficial liquid velocities. *Symbols:* experimental and simulation results. *Lines:* fitting of the experimental data (Eq. 6.4).

were run in 2D and with liquid viscosities different than the experimental ones. However, there is no clear evidence of which of these two effects plays a more important role in this case.

Fig. 8.14 shows the saturation frequencies for both experiments and numerical simulations. To achieve this, the maximum frequencies observed in the simulations for each given U_{SL} in Fig. 8.13 have been assumed to correspond to the saturation regime. The same values and fitting as plotted in Fig. 6.3 have been used for the experimental data. A linear fit also hold for the simulation data, providing the following expression:

$$f_{sat}(U_{SL}) = 912.5 \cdot U_{SL} \tag{8.1}$$

Assuming that numerical simulations behave similarly to the experiments, one would expect that the volume of liquid required to generate and detach a bubble in the simulations would remain constant inside the saturation regime as observed in the experiments. Under that assumption, from Eq. 8.1 we obtain a value of L_L equal to $1.09 \cdot 10^{-3}\, m$ for the simulations, analogous to the value $1.39 \cdot 10^{-3}\, m$ found in Subsection 6.1.1 for the experiments.

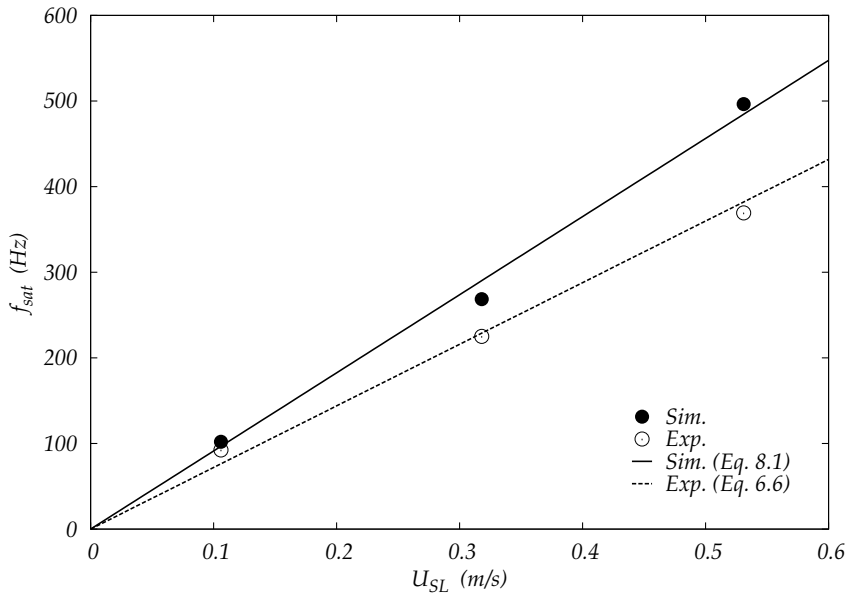

Figure 8.14: Saturation frequency as a function of the superficial liquid velocity. *Symbols:* experimental and numerical simulation data, *solid line:* linear fitting of the experimental data (Eq. 6.6), *dotted line:* linear fitting of the numerical simulation data (Eq. 8.1).

The dimensionless frequency, or Strouhal number, is represented in Fig. 8.15 as a function of the void fraction for both experiments and numerical simulations. Lines represent the theoretical approximation for St in both saturation and linear regimes, as expressed by Eqs. 6.17 and 6.21, respectively. Taking into account the different values of C_0 and L_L found in this analysis for both experiments and simulations (1.08 and $1.39 \cdot 10^{-3}\, m$, 1.21 and $1.09 \cdot 10^{-3}\, m$, respectively), Eq. 6.17 can be rewritten in each case as follows: for the experiments,

$$St = 0.67\,(1 - 1.08\,\alpha) \tag{8.2}$$

and for the numerical simulations

$$St = 0.75\,(1 - 1.21\,\alpha) \tag{8.3}$$

For $\alpha > 0.2$ experimental and numerical data show a linear behavior in accordance with Eq. 8.2 and 8.3, respectively. Points with $\alpha < 0.2$ correspond to the linear regime. In the absence of more simulation data concerning the frequency in the linear regime, we consider the initial slope to be the same in experiments and numerical simulations as an approximation. In fact, accordingly to Fig. 8.13 one would expect no large differences between the experimental and simulation

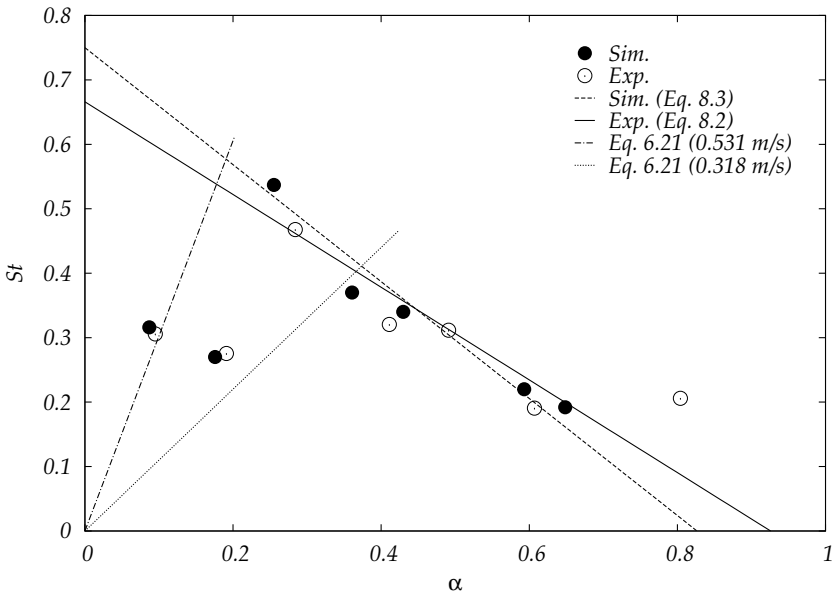

Figure 8.15: Strouhal number as a function of the void fraction. *Symbols:* experimental and simulation data. *Solid line:* prediction for the experiments in the saturation regime (Eq. 8.2), *dotted line:* prediction for the simulations in the saturation regime (Eq. 8.3), *dash dotted line:* prediction of Eq. 6.21 for $U_{SL} = 0.531\,m/s$, and *dash line:* prediction of Eq. 6.21 for $U_{SL} = 0.318\,m/s$.

initial slopes for the values of U_{SL} used in this work. Therefore, same predictions provided by Eq. 6.21 are plotted in Fig. 8.15 for experiments and simulations, corresponding to a value of 0.531 and $0.318\,m/s$ for the superficial liquid velocity. Once again the similarity is noticeable between the experimental and simulation data despite the differences between 3D and 2D cases. Discrepancies with the predictions can be explained in terms of errors occurred during the measurement of f, U_{SG}, U_{SL} and U_G. In any case, both experimental and numerical simulations tendencies are well reproduced.

8.3.3 Bubble and unit cell lengths

The bubble length has been directly measured from simulations and compared to the experimental data. Bubble length, normalized with the capillary diameter and considered as the gas displacement during the time required to generate one bubble $1/f$, can be estimated as a first approximation from Eq. 7.22.

Fig. 8.16 shows the dimensionless measured bubble length in simulations

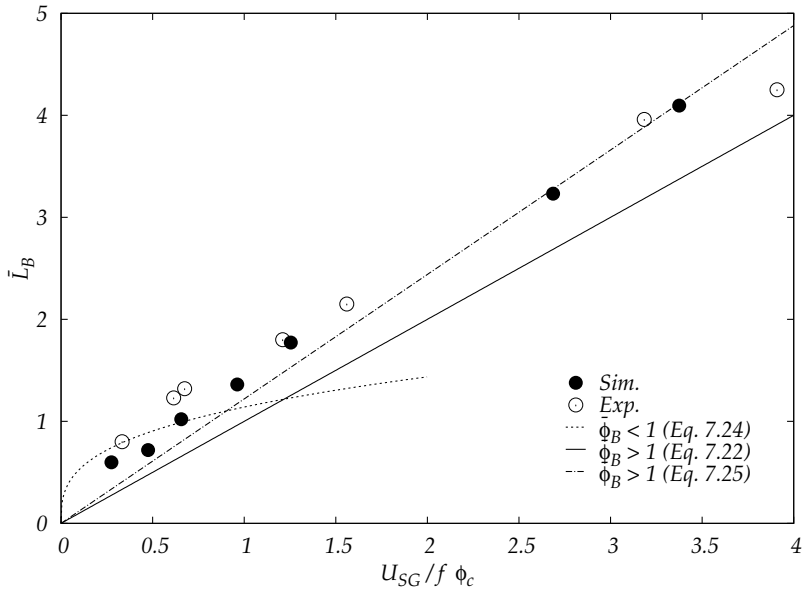

Figure 8.16: Normalized bubble length as a function of $U_{SG}/f\,\phi_c$. *Symbols:* experimental and numerical data. *Solid line:* prediction given by Eq. 7.22, *dotted line:* prediction given by Eq. 7.24, and *dash dotted line:* prediction given by 7.25.

and experiments as a function of $U_{SG}/f\,\phi_c$. Although the values of C_0 and L_L are different for both experimental and numerical simulations, predictions provided by Eqs. 7.22, 7.24 and 7.25 are also plotted as a reference in order to analyze the tendency of $\bar{L}_B$. As expected, it can be observed that bubble lengths are underpredicted by Eq. 7.22 in both cases. This disagreement can be explained again by the fact that Eq. 7.22 corresponds to the length that bubbles would have in case they were to fill the whole capillary cross-section and were not longitudinally deformed by the liquid drag. Fig. 7.1 shows the distinction between the bubble length given by Eq. 7.22 and the actual bubble length which was measured in the simulations and experiments.

Data fits better to the tendency offered by Eqs. 7.24 and 7.25, agreeing with the experimental results of Section 7.3.2.3. Nevertheless, more data from simulations are again required for a more accurate verification of these predictions. It can also be observed that the experimental bubble lengths are slightly greater than the ones in the 2D simulations, which supports the fact that the generation frequencies are smaller in the experiments.

According to Chapter 6, the bubble generation frequency is basically con-

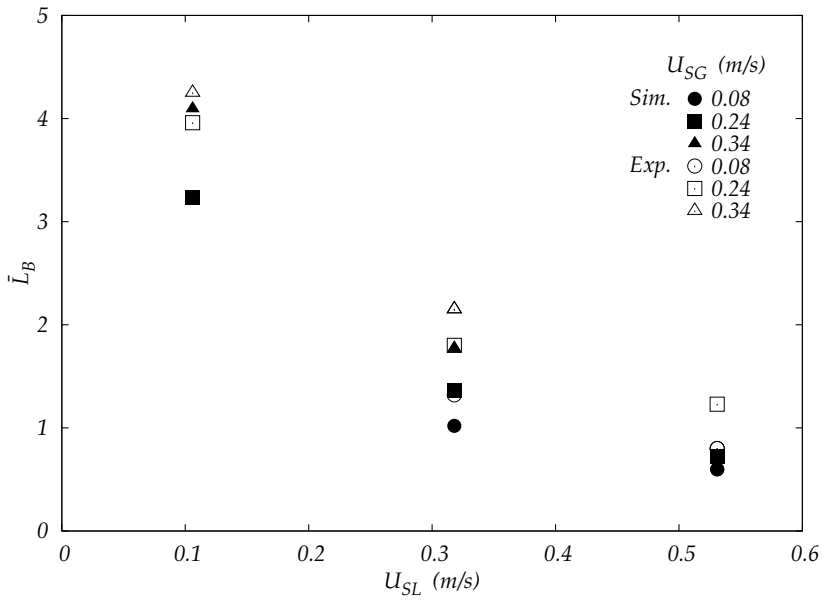

Figure 8.17: Normalized bubble length as a function of the liquid superficial velocity. *Symbols:* experimental and numerical data.

trolled by the gas and liquid flow rates, and hence must be L_B. Fig. 8.17 shows the dimensionless bubble length as a function of the liquid superficial velocity. An increase in bubble size can be observed when increasing U_{SG}, and a decrease in bubbles size when U_{SL} is increased. The behavior shown in Fig. 8.17 is in agreement with recently reported results by Fu *et al.* [32].

A high regularity in the generation of bubbles and in the bubble size has been observed in the simulations. The standard deviation obtained was smaller than 0.1, two orders of magnitude smaller than the mean bubble length. Therefore, we assumed that each train of bubbles could be represented by a unit cell composed of one bubble and the liquid slug between two bubbles. The unit cell length was calculated as the distance between the tip of two consecutive bubbles, as in the experiments, again expressed by Eq.7.1.

Fig. 8.18 shows the dimensionless measured unit cell length in simulations and experiments as a function of $U_G / f\,\phi$ and the expected behavior given by Eq. 7.1. In this case, both experiments and simulations coincide with the prediction. When compared to those from the experiments, the smaller $\bar{L}_{UC}$ are consistent with the larger bubble generation frequencies and both the smaller bubble and minimum liquid slug lengths given by the simulations.

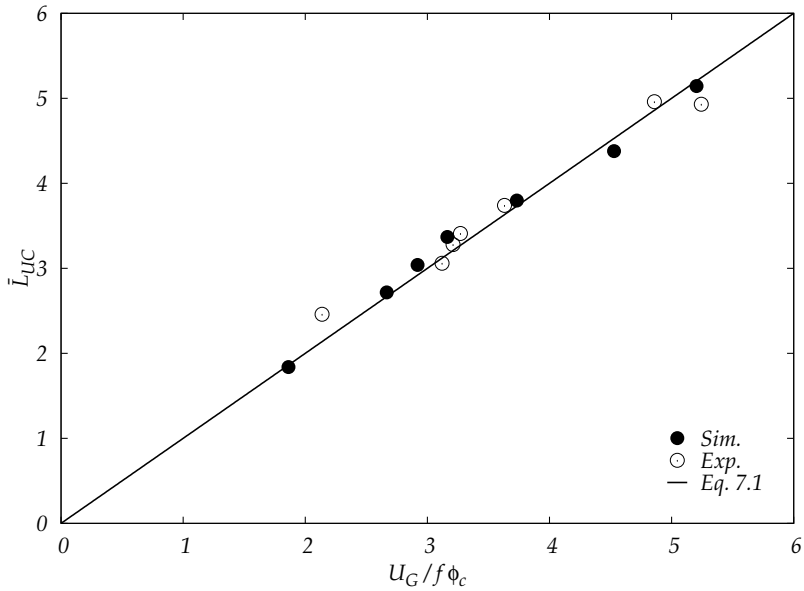

Figure 8.18: Dimensionless unit cell length as a function of $U_G / f \phi_c$. *Symbols:* experimental and numerical data. *Line:* theoretical prediction given by Eq. 7.1.

8.4 Conclusions

We have presented a study of the formation of minibubbles in a T-junction by means of the fluid dynamics numerical code JADIM. Numerical simulation results have been compared with previous experimental work.

A dimensional analysis based on the Buckingham's π theorem has been carried out in order to determine the dimensionless numbers dominating the generation and detachment of bubbles in the system. Simulations have been carried out with the values of the gas and liquid superficial velocities used in the experiments. Only viscosity had to be changed in simulations from the experimental values in order to avoid the development of numerical spurious currents.

The numerical modelling of the T-junction requires an accurate selection of boundary conditions and, in particular, of the contact angle between the gas-liquid interface and the walls of the system. Considering that we aimed at reproducing by means of numerical simulations in 2D the existing 3D experimen-

tal results, we have focused on the squeezing process of the gas thread in the T-junction. Since forces acting on the gas thread depend on the dimensionality, an artificial squeezing mechanism based on the observation of the thread orientation from the experimental images has been implemented in the numerical code in order to eliminate the 2D effects.

The numerical generation of a train of bubbles in a mini-channel in conditions relevant to microgravity has been satisfactorily obtained. In particular, numerical simulations reproduce the bubble and slug flow patterns observed experimentally.

We have obtained results on the behavior of bubble velocity, void fraction, bubble generation frequency and bubble, minimum liquid slug and unit cell lengths. A stable periodicity during the bubble generation and regularity in bubble size have been observed. A linear and a saturation regime in the bubble frequency as observed in the experiments have also been reproduced. Bubble shape and bubble position in the capillary centerline agree with the behavior observed in experiments.

Thus, since 2D simulations and 3D experimental results are very similar, we can conclude that the squeezing process and, in particular, the orientation of the gas thread in time, fully determine the characteristics of the generated flows. In fact, we have shown that 2D numerical simulations can reproduce 3D flow characteristics in other regimes of the T-junction, provided that an adequate squeezing mechanism is implemented. In addition, when no artificial squeezing mechanism is applied in our simulations, one would expect to generate flows similar to those which would be observed in 2D or quasi-2D experiments.

We conclude in this Chapter that JADIM is an appropriate tool for the numerical study of two-phase flows generated in a T-junction.

CHAPTER 9

Conclusions and future work

In this last chapter we present a general overview of this work, outlining the main conclusions achieved (Section 9.1) as well as describing necessary research to be carried out in the future (Section 9.2).

9.1 Conclusions

This work has been a step in the direction of understanding the behavior of two-phase flows in conditions relevant for a microgravity environment. We have presented an extensive study of the bubble and slug flow regimes generated in a 1 *mm* capillary T-junction for a broad range of gas and liquid flow rates. Experiments have been carried out on ground with an air-water mixture. Adiabatic conditions have been assumed for all of the experiments, and therefore thermal exchange between phases or phase changes have been not considered. The T-junction has been mainly operated in the capillary and laminar regimes.

The key conclusions for this work are:

- **Experimental setup.** A new experimental setup has been designed in order to perform the experiments reported in this work, in which gas and liquid flow rates at the T-junction inlets are accurately controlled, measured and monitored. The data acquisition system provides high quality images, from which we have extracted the bubble generation frequency and velocity, as well as the bubble, unit cell and liquid slug lengths. The gas and liquid superficial velocities and the mean void fraction have also

been estimated.

- **Flow patterns.** Bubble, slug, churn and annular flow patterns have been observed in our experiments. A flow pattern map in terms of the superficial gas and liquid velocities has been plotted. The bubble-slug transition has been analyzed, confirming the existence of a critical void fraction equal to 0.2, which disagrees with the Suratman number model's predictions. The large influence of the entrance effects and the small relevance of coalescence phenomena in our system has been concluded to be the cause of this disagreement.

- **Bubble velocity and void fraction.** An experimental study on bubble velocity and mean void fraction has been carried out. Both of them have been well predicted by using the drift-flux model under the assumption of no drift velocity of the gas relative to the mean fluid velocity. A value of 1.22 has been found for the void fraction distribution coefficient for most of the experimental data.

- **Bubble generation frequency.** The bubble generation phenomenon has been analyzed, focusing on the bubble and slug flow regimes. High bubble generation frequencies up to about 1200 Hz with small size dispersion have been achieved. The generation frequency presents a linear behavior at small gas fluxes followed by a saturation state. Bubble and slug flow regimes have been found to show both linear and saturation tendencies, depending on the gas and liquid superficial velocities. A new expression for the bubble generation frequency as a function of gas and liquid superficial velocities has been proposed.

- **Linear and saturation regime.** The fitting of experimental results has allowed for the obtaining of empirical predictions for the initial slope, the crossover point and the saturation frequency, while being consistent with previous theoretical considerations regarding the bubble generation under surface tension dominated conditions. The variation of the initial slope and the crossover point with the superficial liquid velocity have both been found to present a linear asymptotic tendency. In addition, results obtained have confirmed the linear behavior of the saturation frequency with the superficial liquid velocity.

- **Dimensionless generation frequency.** A new dimensionless expression of the generation frequency based on the Strouhal number has been derived. This expression has been particularized in both the linear and saturation regimes. The Strouhal number has been found to depend in turn on the mean void fraction as a single relevant parameter.

- **Characteristic lengths.** The geometry of the continuous and discontinuous phases has been studied, distinguishing again between the bubble and slug flow regimes. This study has focused on the analysis of the bubble, unit cell and liquid slug lengths, as well as on the bubble equivalent diameter and the liquid film thickness. These parameters have been related to the gas and liquid superficial velocities, the bubble generation frequency, the mean void fraction and the Strouhal number.

  Bubble equivalent diameter decreases linearly with the Weber number based upon the superficial liquid velocity. Furthermore, results are consistent with the prediction of independence of the bubble size on gas flow rate for small fluxes. Controllable bubble equivalent diameter of the order of the capillary and reduced bubble size dispersion have been obtained. Minimum values of $C_O \cdot L_{LS}$ and $1.39 \cdot 10^{-3}\, m$ have been found for the unit cell and liquid slug, respectively. Finally, it has been concluded that these characteristic lengths can be expressed in terms of a single relevant parameter, such as the mean void fraction or the Strouhal number.

- **Numerical simulations.** The formation of minibubbles in a T-junction by means of the fluid dynamics numerical code JADIM has been studied. Numerical simulations results have been compared with our experimental work. An artificial squeezing mechanism based on the comparison with the experimental images has been implemented in the numerical code in order to rid the simulations of 2D effects. The numerical generation of a train of bubbles in a mini-channel in conditions relevant to microgravity has been satisfactorily obtained. In particular, numerical simulations reproduce well the bubble and slug flow patterns observed experimentally. We have obtained results on the behavior of bubble velocity, void fraction, bubble generation frequency and bubble, minimum liquid slug and unit cell lengths.

  A stable periodicity during the bubble generation and regularity in bubble size have been observed in the numerical simulation. A linear and a saturation regime in the bubble frequency as observed in the experiments have been also reproduced. Bubble shape and bubble position in the capillary centerline agree with the behavior observed in experiments. Bubble and unit cell lengths have also shown the same tendencies as have been observed in the experimental data. We have concluded that JADIM is an appropriate tool for the numerical study of two-phase flows generated in a T-junction.

- **Gravity independence.** As a final remark, we would like to note that experiments carried out on the ground with small enough values for the

Bond number can satisfactorily reproduce the conditions of a microgravity relevant environment. By operating in the capillary regime, these on ground experiments and numerical simulations could provide valuable information on the performance of two-phase flows for in-space systems for both designers and researchers.

9.2 Future work

Further studies are still required in order to gain a more detailed understanding on the behavior of two-phase flows in a low gravity environment. Some remaining open questions are summarized below:

- In order to characterize the churn and annular flow patterns, other parameters regimes with larger gas and liquid flow rates must be explored. More experiments are required to assess further issues concerning the slug-churn transition as well as the churn-annular transition. For these reasons, the design of a new experimental setup based on pressure controller/measures as well as both gas and liquid mass flow meters with operational limits larger than those used in this work must be achieved.

- Changes in fluids and the capillary geometry are needed in order to check the effects of the gas and liquid physical properties as well as the capillary hydraulic diameter in the parameters studied in this work.

- Although the mixture seems to be in steady conditions after the formation in the T-junction, additional experiments with a large length-to-diameter ratio should be performed in order to well establish the influence of the channel length on the developing flow patterns and the bubble-slug transition.

- Different gas and liquid injection strategies, such as the exchange between the gas and liquid inlets, must be analyzed and compared with the one studied here. Further analyses are required regarding the effects of moving from a T-junction to a Y-junction or a flow focusing strategy.

- Future numerical simulations focused on full 3D simulations are required in order to make a direct comparison with experiments possible, especially concerning the pinch-off mechanism. This may allow for a future exploration of parameter regimes for this system which are difficult to achieve experimentally.

- Finally, it would be highly desirable to check the validity of the results of our experiments in real microgravity conditions, such as drop towers, parabolic flights or sounding rockets.

APPENDIX $\mathcal{A}$

Numerical Code JADIM

The implemented VoF method in JADIM consists of an Eulerian description of each phase on a fixed grid, the interface between the two phases being calculated using the transport equation of the local volume fraction of one of the phases. The two fluids are assumed to be Newtonian and incompressible with no phase change. Under isothermal conditions and in the absence of any surfactant the surface tension is constant and uniform at the interface between the two fluids. In such conditions, the velocity field **U** and the pressure P satisfy the classical one-fluid formulation of the Navier-Stokes equations:

$$\nabla \cdot U = 0 \tag{A.1}$$

$$\frac{\partial U}{\partial t} + U.\nabla U = -\frac{1}{\rho}\nabla P + \frac{1}{\rho}\nabla.\Sigma + g + F_\sigma \tag{A.2}$$

where Σ is the viscous stress tensor, and F_σ is the capillary contribution:

$$F_\sigma = -\frac{\sigma}{\rho}\left(\nabla.\mathbf{n}\right)\mathbf{n}\delta_I \tag{A.3}$$

where **n** denotes by arbitrary choice the unit normal to the interface going out from phase 1 and δ_I is the Dirac distribution associated to the interface. The location of each phase is given by a scalar C (called volume fraction or color function) which obeys the transport equation:

$$\frac{\partial C}{\partial t} + U.\nabla C = 0 \tag{A.4}$$

This volume fraction is $C = 1$ (resp. $C = 0$) in cells filled with liquid (resp.

gas) and $0 < C < 1$ in cells cut by the interface. Local density and dynamic viscosity are deduced from the value of C by a linear interpolation:

$$\rho = C\rho_L + (1 - C)\rho_G \tag{A.5}$$

$$\mu = C\mu_L + (1 - C)\mu_G \tag{A.6}$$

Compared to the classical VoF or Level Set methods [79, 81, 84], the specific aspect of this approach concerns the technique used to control the stiffness of the interface. In this approach no interface reconstruction or redistancing algorithm are introduced. Interface location and stiffness are both controlled by an accurate transport algorithm based on FCT (Flux-Corrected-Transport) schemes [90]. This method leads to an interface thickness of about three grid cells through the implementation of a specific procedure for the velocity used to transport C in a flow region of strong strain and shear [9].

The numerical description of the surface tension is one of the crucial points for the study of systems where capillary effects control the interface shape. This interfacial force is solved using the classical CSF (Continuum Surface Force) model [12] and is distributed over grid points neighboring the interface:

$$F_\sigma = -\frac{\sigma}{\rho}\nabla.\left(\frac{\nabla C}{\|\nabla C\|}\right)\nabla C \tag{A.7}$$

The volumetric expression of the capillary term is composed of two terms: one representing the curvature, $\nabla.(\nabla C/\|\nabla C\|)$, and the other representing the location/orientation, ∇C, of the capillary forcing. A classical problem with this formulation is the generation of spurious currents [46, 72] due to a sharp variation of C throughout the transition region between the two phases. In order to decrease the intensity of spurious currents, a classical solution introduced by Brackbill *et al.* [12] consists of the calculation of the surface curvature from a smoothed density gradient while the discretization of the delta function uses a non-smoothed density. In this code the spurious currents were characterized by Dupont and Legendre [24] and their maximum magnitude was found to evolve as $\approx 0.004\sigma/\mu$, in agreement with other codes using the Brackbill formulation.

The volume fraction C and the pressure P are volume-centered and the velocity components are face-centered. Time advancement is achieved through a third-order Runge-Kutta method for viscous stresses. Incompressibility is satisfied at the end of each time step through a projection method. The overall algorithm is second-order accurate in both time and space. For a detailed description see [9, 24].

The Volume of Fluid (VoF) modulus of JADIM has been previously validated and used for studies dealing with bubble dynamics in unbounded situations [8, 9], droplets in rectangular mini-channels [78] and sliding drops on inclined walls and in mini-channels [24]. The code is used in this study to simulate the generation of mini-bubbles in a T-junction.

APPENDIX $\mathcal{B}$

Experimental data

Ref.	U_{SG} $[m/s]$	U_{SL} $[m/s]$	U_G $[m/s]$	α	f $[Hz]$	L_B $[mm]$	L_{LS} $[mm]$	L_{UC} $[mm]$	FP
S1-013	0.005	0.460	0.597	0.009	14	-	-	-	B
S1-014	0.011	0.460	0.603	0.018	31	-	-	-	B
S1-015	0.021	0.460	0.635	0.033	54	-	-	-	B
S1-016	0.032	0.460	0.632	0.050	77	-	-	-	B
S1-017	0.042	0.460	0.617	0.069	109	-	-	-	B
S1-018	0.064	0.460	0.584	0.109	143	-	-	-	B
S1-019	0.085	0.460	0.628	0.135	171	-	-	-	S
S1-020	0.106	0.460	0.658	0.161	209	-	-	-	S
S1-021	0.170	0.460	0.725	0.234	257	-	-	-	S
S1-022	0.212	0.460	0.759	0.280	289	-	-	-	S
S1-023	0.318	0.460	0.904	0.352	320	-	-	-	S
S1-024	0.424	0.460	1.034	0.410	331	-	-	-	S
S1-025	0.531	0.460	1.196	0.444	334	-	-	-	S
S1-026	0.637	0.460	1.364	0.467	337	-	-	-	S
S1-027	0.743	0.460	1.478	0.503	334	-	-	-	S
S1-028	0.849	0.460	1.620	0.524	337	-	-	-	S
S1-046	0.005	0.725	0.957	0.006	32	-	-	-	B
S1-047	0.011	0.725	1.005	0.011	96	-	-	-	B
S1-048	0.021	0.725	0.946	0.022	148	-	-	-	B

(Continued)

Ref.	U_{SG} $[m/s]$	U_{SL} $[m/s]$	U_G $[m/s]$	α	f $[Hz]$	L_B $[mm]$	L_{LS} $[mm]$	L_{UC} $[mm]$	FP
S1-049	0.032	0.725	1.031	0.031	204	-	-	-	B
S1-050	0.042	0.725	1.039	0.041	232	-	-	-	B
S1-051	0.064	0.725	1.127	0.056	300	-	-	-	B
S1-052	0.085	0.725	1.109	0.077	360	-	-	-	B
S1-053	0.106	0.725	1.096	0.097	408	-	-	-	B
S1-054	0.170	0.725	1.027	0.165	480	-	-	-	B
S1-055	0.212	0.725	1.103	0.192	500	-	-	-	B
S1-056	0.318	0.725	1.244	0.256	516	-	-	-	S
S1-057	0.424	0.725	1.336	0.318	532	-	-	-	S
S1-058	0.531	0.725	1.513	0.351	520	-	-	-	S
S1-059	0.637	0.725	1.151	0.553	524	-	-	-	S
S1-060	0.743	0.725	1.830	0.406	528	-	-	-	S
S1-061	0.849	0.725	1.873	0.453	512	-	-	-	S
S1-062	0.955	0.725	1.963	0.486	520	-	-	-	S
S2-003	0.043	0.212	0.242	0.177	48	1.32	4.19	5.51	S
S2-004	0.081	0.318	0.421	0.191	120	1.32	2.42	3.74	S
S2-005	0.066	0.424	0.518	0.127	120	0.90	3.39	4.29	S
S2-006	0.068	0.531	0.711	0.095	204	0.80	2.61	3.41	B
S2-007	0.068	0.637	0.845	0.080	308	0.64	2.29	2.93	B
S2-008	0.064	0.743	0.884	0.072	456	0.61	1.48	2.09	B
S2-009	0.059	0.849	0.983	0.060	656	0.51	1.16	1.67	B
S2-010	0.049	0.955	1.097	0.044	684	0.45	0.93	1.38	B
S2-011	0.042	1.061	1.260	0.034	660	0.46	1.70	2.16	B
S2-012	0.038	1.167	1.373	0.028	696	0.46	1.47	1.93	B
S2-013	0.036	1.273	1.629	0.022	736	0.40	2.70	3.10	B
S2-014	0.036	1.379	2.080	0.017	-	0.50	1.23	1.73	B
S2-015	0.032	1.485	2.040	0.016	-	0.40	3.23	3.63	B
S2-018	0.081	0.212	0.305	0.264	64	1.48	2.97	4.45	S
S2-019	0.106	0.318	0.423	0.251	120	1.29	2.19	3.48	S
S2-020	0.127	0.424	0.604	0.211	212	1.06	1.74	2.80	S
S2-021	0.110	0.531	0.760	0.145	280	0.86	1.84	2.70	B
S2-022	0.108	0.637	0.885	0.122	380	0.83	1.73	2.56	B
S2-023	0.102	0.743	1.005	0.101	508	0.73	1.77	2.50	B
S2-024	0.110	0.849	1.110	0.099	580	0.70	1.66	2.36	B
S2-025	0.098	0.955	1.283	0.076	644	0.56	1.87	2.43	B
S2-026	0.089	1.061	1.613	0.055	680	0.53	2.33	2.86	B

(Continued)

Ref.	U_{SG} $[m/s]$	U_{SL} $[m/s]$	U_G $[m/s]$	α	f $[Hz]$	L_B $[mm]$	L_{LS} $[mm]$	L_{UC} $[mm]$	FP
S2-027	0.098	1.167	1.657	0.059	796	0.53	1.60	2.13	B
S2-028	0.093	1.273	1.924	0.049	868	0.50	2.00	2.50	B
S2-029	0.089	1.379	1.985	0.045	1000	0.53	2.07	2.60	B
S2-030	0.083	1.485	1.992	0.042	1058	0.50	1.30	1.80	B
S2-031	0.074	1.592	2.266	0.033	1178	0.46	1.50	1.96	B
S2-032	0.068	1.698	2.613	0.026	1290	0.46	1.57	2.03	B
S2-035	0.180	0.212	0.428	0.421	124	2.20	1.33	3.53	S
S2-036	0.182	0.318	0.527	0.346	180	1.53	1.43	2.96	S
S2-037	0.178	0.424	0.636	0.280	244	1.20	1.43	2.63	S
S2-038	0.178	0.531	0.767	0.233	332	1.00	1.36	2.36	S
S2-039	0.178	0.637	0.931	0.191	420	0.86	1.44	2.30	B
S2-040	0.176	0.743	1.069	0.165	488	0.86	1.37	2.23	B
S2-041	0.174	0.849	1.244	0.140	564	0.80	1.63	2.43	B
S2-042	0.172	0.955	1.384	0.124	616	0.76	1.74	2.50	B
S2-043	0.170	1.061	1.583	0.107	708	0.73	1.67	2.40	B
S2-044	0.168	1.167	1.872	0.090	812	0.63	1.30	1.93	B
S2-045	0.168	1.273	1.993	0.084	884	0.63	1.10	1.73	B
S2-046	0.172	1.379	2.092	0.082	984	0.70	1.83	2.53	B
S2-047	0.161	1.485	2.154	0.075	1048	0.63	1.93	2.56	B
S2-048	0.142	1.592	2.280	0.062	1112	0.46	1.87	2.33	B
S2-049	0.144	1.698	2.472	0.058	1212	0.60	1.26	1.86	B
S2-052	0.242	0.212	0.462	0.523	136	2.46	1.20	3.66	S
S2-053	0.242	0.318	0.589	0.411	200	1.80	1.26	3.06	S
S2-054	0.238	0.424	0.703	0.338	272	1.46	1.24	2.70	S
S2-055	0.236	0.531	0.828	0.284	348	1.23	1.23	2.46	B
S2-056	0.236	0.637	0.947	0.249	400	1.13	1.37	2.50	B
S2-057	0.233	0.743	1.071	0.218	468	0.96	1.34	2.30	B
S2-058	0.233	0.849	1.218	0.192	556	0.86	1.34	2.20	B
S2-059	0.233	0.955	1.423	0.164	632	0.86	1.97	2.83	B
S2-060	0.231	1.061	1.683	0.137	736	0.76	1.50	2.26	B
S2-061	0.227	1.167	1.840	0.123	780	0.80	1.56	2.36	B
S2-062	0.225	1.273	1.874	0.120	876	0.70	1.26	1.96	B
S2-063	0.223	1.379	2.214	0.101	1012	0.73	1.57	2.30	B
S2-064	0.221	1.485	2.254	0.098	1068	0.63	1.37	2.00	B
S2-065	0.216	1.592	2.461	0.088	1212	0.63	1.23	1.86	B
S2-066	0.214	1.698	2.522	0.085	1256	0.56	0.94	1.50	B

(Continued)

Ref.	U_{SG} $[m/s]$	U_{SL} $[m/s]$	U_G $[m/s]$	α	f $[Hz]$	L_B $[mm]$	L_{LS} $[mm]$	L_{UC} $[mm]$	FP
S2-069	0.295	0.212	0.549	0.537	148	2.90	1.13	4.03	S
S2-070	0.293	0.318	0.661	0.443	208	2.06	1.24	3.30	S
S2-071	0.291	0.424	0.781	0.372	284	1.73	1.17	2.90	S
S2-072	0.286	0.531	0.886	0.323	368	1.46	1.10	2.56	S
S2-073	0.286	0.637	0.997	0.287	432	1.16	1.17	2.33	S
S2-074	0.286	0.743	1.136	0.252	484	1.13	1.23	2.36	S
S2-075	0.286	0.849	1.242	0.231	552	1.06	1.20	2.26	S
S2-076	0.284	0.955	1.397	0.204	620	1.10	1.40	2.50	S
S2-077	0.284	1.061	1.592	0.179	692	1.10	1.53	2.63	B
S2-078	0.282	1.167	1.699	0.166	788	1.00	1.63	2.63	B
S2-079	0.280	1.273	1.888	0.148	884	0.86	1.57	2.43	B
S2-080	0.274	1.379	2.073	0.132	1028	0.73	1.17	1.90	B
S2-081	0.274	1.485	2.320	0.118	1064	0.70	1.50	2.20	B
S2-082	0.272	1.592	2.533	0.107	1220	0.60	0.96	1.56	B
S2-083	0.267	1.698	2.743	0.097	1288	0.66	1.14	1.80	B
S2-086	0.340	0.212	0.558	0.609	152	2.84	0.97	3.81	S
S2-087	0.337	0.318	0.687	0.491	216	2.15	1.13	3.28	S
S2-088	0.335	0.424	0.794	0.422	292	1.78	1.09	2.87	S
S2-089	0.333	0.531	0.906	0.368	372	1.50	0.93	2.43	S
S2-090	0.333	0.637	1.021	0.326	420	1.40	1.10	2.50	S
S2-091	0.331	0.743	1.129	0.293	496	1.28	1.09	2.37	S
S2-092	0.329	0.849	1.249	0.263	564	1.21	1.19	2.40	S
S2-093	0.329	0.955	1.360	0.242	620	1.10	1.33	2.43	S
S2-094	0.327	1.061	1.508	0.217	708	1.21	1.25	2.46	B
S2-095	0.327	1.167	1.612	0.203	796	0.93	1.50	2.43	B
S2-096	0.325	1.273	1.816	0.179	900	0.84	1.28	2.12	B
S2-097	0.320	1.379	2.135	0.150	1012	0.96	1.17	2.13	B
S2-098	0.323	1.485	2.246	0.144	1048	0.76	1.37	2.13	B
S2-099	0.318	1.592	2.427	0.131	1184	0.70	1.53	2.23	B
S2-100	0.318	1.698	2.612	0.122	1272	0.70	1.33	2.03	B
S2-103	0.384	0.212	0.673	0.570	156	3.36	1.07	4.43	S
S2-104	0.380	0.318	0.785	0.484	224	2.56	1.07	3.63	S
S2-105	0.397	0.424	0.903	0.440	292	2.03	1.13	3.16	S
S2-106	0.376	0.531	0.957	0.392	376	1.60	1.10	2.70	S
S2-107	0.373	0.637	1.157	0.323	428	1.76	1.14	2.90	S
S2-108	0.373	0.743	1.262	0.296	500	1.53	1.13	2.66	S

(Continued)

Ref.	U_{SG} $[m/s]$	U_{SL} $[m/s]$	U_G $[m/s]$	α	f $[Hz]$	L_B $[mm]$	L_{LS} $[mm]$	L_{UC} $[mm]$	FP
S2-109	0.371	0.849	1.394	0.266	564	1.43	1.33	2.76	S
S2-110	0.371	0.955	1.547	0.240	640	1.40	1.06	2.46	S
S2-111	0.365	1.061	1.675	0.218	708	1.33	1.07	2.40	S
S2-112	0.367	1.167	1.786	0.206	796	1.16	1.44	2.60	S
S2-113	0.367	1.273	2.040	0.180	896	1.10	1.40	2.50	B
S2-114	0.365	1.379	2.299	0.159	992	1.10	1.43	2.53	B
S2-115	0.363	1.485	2.301	0.158	1084	0.96	1.04	2.00	B
S2-116	0.363	1.592	2.472	0.147	1188	0.83	1.27	2.10	B
S2-117	0.361	1.698	2.788	0.129	1244	0.70	0.96	1.66	B
S2-120	0.473	0.212	0.782	0.605	164	3.90	1.00	4.90	S
S2-121	0.473	0.318	0.902	0.525	228	2.96	1.14	4.10	S
S2-122	0.471	0.424	1.050	0.448	300	2.50	1.13	3.63	S
S2-123	0.469	0.531	1.160	0.404	368	2.13	1.13	3.26	S
S2-124	0.471	0.637	1.048	0.450	436	1.93	1.27	3.20	S
S2-125	0.469	0.743	1.423	0.330	520	1.80	1.03	2.83	S
S2-126	0.469	0.849	1.514	0.310	572	1.70	1.16	2.86	S
S2-127	0.469	0.955	1.667	0.281	628	1.66	1.24	2.90	S
S2-128	0.469	1.061	1.832	0.256	700	1.50	1.30	2.80	S
S2-129	0.469	1.167	1.954	0.240	784	1.38	1.23	2.61	S
S2-130	0.469	1.273	2.160	0.217	892	1.09	1.61	2.70	S
S2-131	0.465	1.379	2.206	0.211	1000	1.09	1.13	2.22	S
S2-132	0.460	1.485	2.280	0.202	1096	1.06	1.26	2.32	B
S2-133	0.460	1.592	2.320	0.198	1176	1.09	1.39	2.48	B
S2-134	0.458	1.698	2.308	0.199	1280	0.77	0.97	1.74	B
S2-137	0.637	0.212	0.920	0.692	160	5.36	1.04	6.40	S
S2-138	0.639	0.318	1.101	0.580	232	4.06	1.07	5.13	S
S2-139	0.639	0.424	1.373	0.465	304	3.56	1.14	4.70	S
S2-140	0.637	0.531	1.461	0.436	368	3.10	1.10	4.20	S
S2-141	0.637	0.637	1.520	0.419	444	2.60	1.13	3.73	S
S2-142	0.637	0.743	1.691	0.377	516	2.36	1.27	3.63	S
S2-143	0.637	0.849	1.946	0.327	584	2.06	1.24	3.30	S
S2-144	0.637	0.955	1.877	0.339	648	1.96	1.16	3.12	S
S2-145	0.637	1.061	2.000	0.318	700	2.10	1.40	3.50	S
S2-146	0.637	1.167	2.168	0.294	784	1.90	0.23	2.13	S
S2-147	0.632	1.273	2.257	0.280	892	1.66	1.40	3.06	S
S2-148	0.630	1.379	2.296	0.275	956	1.53	1.47	3.00	S

(Continued)

Ref.	U_{SG} $[m/s]$	U_{SL} $[m/s]$	U_G $[m/s]$	α	f $[Hz]$	L_B $[mm]$	L_{LS} $[mm]$	L_{UC} $[mm]$	FP
S2-149	0.630	1.485	2.440	0.258	1092	1.50	1.13	2.63	S
S2-150	0.630	1.592	2.536	0.249	1164	1.43	1.07	2.50	S
S2-151	0.632	1.698	2.652	0.238	1232	1.16	1.27	2.43	S
S2-153	0.950	0.042	1.200	0.792	-	-	-	-	C
S2-154	0.950	0.106	1.156	0.822	96	-	-	-	C
S2-155	0.950	0.212	1.360	0.699	168	8.26	0.87	9.13	S
S2-156	0.950	0.318	1.524	0.623	240	5.90	0.96	6.86	S
S2-157	0.950	0.424	1.641	0.579	304	4.80	1.06	5.86	S
S2-158	0.950	0.531	1.987	0.478	376	3.70	1.10	4.80	S
S2-159	0.950	0.637	1.917	0.496	448	3.40	0.83	4.23	S
S2-160	0.950	0.743	2.057	0.462	520	2.83	1.07	3.90	S
S2-161	0.950	0.849	1.693	0.561	560	2.90	0.93	3.83	S
S2-162	0.950	0.955	2.316	0.410	624	2.60	1.13	3.73	S
S2-163	0.950	1.061	2.383	0.399	688	2.63	1.03	3.66	S
S2-164	0.950	1.167	2.514	0.378	784	2.36	1.30	3.66	S
S2-165	0.950	1.273	2.600	0.365	848	2.16	1.20	3.36	S
S2-166	0.950	1.379	2.629	0.362	936	1.86	0.97	2.83	S
S2-167	0.950	1.485	2.785	0.341	1024	1.80	1.30	3.10	S
S2-168	0.950	1.592	2.899	0.328	1088	1.83	1.33	3.16	S
S2-169	0.950	1.698	3.073	0.309	1184	1.23	0.70	1.93	B
S2-172	1.099	0.106	1.385	0.794	104	-	-	-	C
S2-173	1.097	0.212	2.084	0.526	168	-	-	-	C
S2-174	1.099	0.318	1.844	0.596	240	7.43	0.70	8.13	C
S2-175	1.099	0.424	1.928	0.570	304	6.70	0.40	7.10	C
S2-176	1.099	0.531	1.990	0.552	384	4.43	0.90	5.33	S
S2-177	1.099	0.637	2.167	0.507	448	3.96	0.84	4.80	S
S2-178	1.099	0.743	2.243	0.490	520	3.46	0.94	4.40	S
S2-179	1.099	0.849	2.366	0.465	576	3.26	0.97	4.23	S
S2-180	1.099	0.955	2.400	0.458	640	3.03	0.93	3.96	S
S2-181	1.099	1.061	2.578	0.426	686	2.93	0.97	3.90	S
S2-182	1.099	1.167	2.698	0.407	776	2.43	1.17	3.60	S
S2-183	1.099	1.273	2.960	0.371	888	2.36	0.97	3.33	S
S2-184	1.099	1.379	3.074	0.358	944	2.13	1.07	3.20	S
S2-185	1.099	1.485	3.017	0.364	1016	2.13	1.40	3.53	S
S2-186	1.099	1.592	3.215	0.342	1128	2.03	1.33	3.36	S
S2-187	1.099	1.698	3.256	0.338	1208	1.80	1.10	2.90	S

(Continued)

Ref.	U_{SG} $[m/s]$	U_{SL} $[m/s]$	U_G $[m/s]$	α	f $[Hz]$	L_B $[mm]$	L_{LS} $[mm]$	L_{UC} $[mm]$	FP
S2-212	2.101	0.531	2.236	0.940	-	-	-	-	C
S2-213	2.101	0.637	2.492	0.843	-	-	-	-	C
S2-214	2.101	0.743	2.862	0.734	516	-	-	-	C

Ref.	U_{SG} $[m/s]$	U_{SL} $[m/s]$	f $[Hz]$	FP
S1-001	0.005	0.308	10	B
S1-002	0.011	0.308	20	S
S1-003	0.021	0.308	37	S
S1-004	0.032	0.308	53	S
S1-005	0.042	0.308	53	S
S1-006	0.053	0.308	70	S
S1-007	0.064	0.308	83	S
S1-008	0.085	0.308	107	S
S1-009	0.106	0.308	127	S
S1-010	0.212	0.308	190	S
S1-011	0.318	0.308	217	S
S1-012	0.424	0.308	227	S
S1-029	0.005	0.615	32	B
S1-030	0.011	0.615	52	B
S1-031	0.021	0.615	104	B
S1-032	0.032	0.615	136	B
S1-033	0.042	0.615	160	B
S1-034	0.064	0.615	224	B
S1-035	0.085	0.615	236	B
S1-036	0.106	0.615	276	B
S1-037	0.170	0.615	352	B
S1-038	0.212	0.615	380	S
S1-039	0.318	0.615	424	S
S1-040	0.424	0.615	444	S
S1-041	0.531	0.615	444	S
S1-042	0.637	0.615	444	S

Ref.	U_{SG} $[m/s]$	U_{SL} $[m/s]$	f $[Hz]$	FP
S2-034	0.182	0.106	68	S
S2-050	0.246	0.042	28	S
S2-051	0.242	0.106	76	S
S2-067	0.297	0.042	28	S
S2-068	0.297	0.106	80	S
S2-084	0.344	0.042	28	S
S2-085	0.344	0.106	88	S
S2-101	0.384	0.042	32	S
S2-102	0.384	0.106	92	S
S2-118	0.477	0.042	-	S
S2-119	0.471	0.106	96	S
S2-135	0.641	0.042	-	S
S2-136	0.639	0.106	92	S
S2-152	0.950	0.022	-	C
S2-170	1.101	0.022	-	C
S2-171	1.101	0.042	-	C
S2-188	1.634	0.022	-	C
S2-189	1.634	0.042	-	C
S2-190	1.634	0.106	-	C
S2-191	1.634	0.212	-	C
S2-192	1.634	0.318	-	C
S2-193	1.634	0.424	312	C
S2-194	1.634	0.531	392	C
S2-195	1.634	0.637	448	C
S2-196	1.634	0.743	512	S
S2-197	1.634	0.849	560	S

(Continued)

Ref.	U_{SG} $[m/s]$	U_{SL} $[m/s]$	f $[Hz]$	FP
S1-043	0.743	0.615	436	S
S1-044	0.849	0.615	440	S
S1-045	0.955	0.615	436	S
S1-063	0.005	0.836	72	B
S1-064	0.011	0.836	124	B
S1-065	0.021	0.836	184	B
S1-066	0.032	0.836	308	B
S1-067	0.042	0.836	392	B
S1-068	0.064	0.836	468	B
S1-069	0.085	0.836	556	B
S1-070	0.106	0.836	556	B
S1-071	0.170	0.836	600	B
S1-072	0.212	0.836	604	B
S1-073	0.318	0.836	608	B
S1-074	0.424	0.836	604	S
S1-075	0.531	0.836	600	S
S1-076	0.637	0.836	588	S
S1-077	0.743	0.836	604	S
S1-078	0.849	0.836	620	S
S2-001	0.065	0.042	20	S
S2-002	0.062	0.106	37	S
S2-016	0.112	0.042	20	S
S2-017	0.100	0.106	44	S
S2-033	0.185	0.042	24	S

Ref.	U_{SG} $[m/s]$	U_{SL} $[m/s]$	f $[Hz]$	FP
S2-198	1.634	0.955	632	S
S2-199	1.634	1.061	720	S
S2-200	1.634	1.167	792	S
S2-201	1.634	1.273	904	S
S2-202	1.634	1.379	944	S
S2-203	1.634	1.485	1048	S
S2-204	1.634	1.592	1104	S
S2-205	1.634	1.698	1192	S
S2-206	2.101	0.022	-	A
S2-207	2.101	0.042	-	A
S2-208	2.101	0.106	-	C
S2-209	2.101	0.212	-	C
S2-210	2.101	0.318	-	C
S2-211	2.101	0.424	-	C
S2-215	2.101	0.849	568	S
S2-216	2.101	0.955	624	S
S2-217	2.101	1.061	716	S
S2-218	2.101	1.167	796	S
S2-219	2.101	1.273	868	S
S2-220	2.101	1.379	944	S
S2-221	2.101	1.485	1060	S
S2-222	2.101	1.592	1132	S
S2-223	2.101	1.698	1200	S

References

[1] P. Andreussi, A. Minervini, and A. Paglianti. Mechanistic model of slug flow in near horizontal pipes. *AIC*, 39:1281–1291, 1993.

[2] S. Arias, R. González-Cinca, X. Ruiz, L. Ramírez-Piscina, and J. Casademunt. Characterization of the performance of a minibubble generator in conditions relevant to microgravity. *Colloids and Surfaces A: Physicochem. Eng. Aspects*, 365:52–55, 2010.

[3] S. Arias, X. Ruiz, J. Casademunt, L. Ramírez-Piscina, and R. González-Cinca. Experimental study of a microchannel bubble injector for microgravity applications. *Microgravity Sci. Technol*, 21:107–111, 2009.

[4] P. Aussillous and D. Quéré. Quick deposition of a fluid on the wall of a tube. *Phys. Fluids*, 12:2367–2371, 2000.

[5] O. Baker. Simultaneous flow of oil and gas. *Oil Gas J.*, 53:185, 1954.

[6] K.H. Bendiksen. An experimental investigation of the motion of long bubbles in inclined tubes. *Int*, 6:467–483, 1984.

[7] A. Bhunia, S.C. Pais, Y. Kamotani, and I. Kim. Bubble formation in a coflow configuration in normal and reduced gravity. *AIChE J.*, 44:1499Â–1509, 1998.

[8] T. Bonometti and J. Magnaudet. Transition from spherical cap to toroidal bubbles. *Phys. Fluids*, 18:052102, 2006.

[9] T. Bonometti and J. Magnaudet. An interface capturing method for incompressible two-phase flows. Validation and application to bubble dynamics. *Int. J. of Multiphase Flow*, 33(2):109–133, 2007.

[10] W.S. Bousman. Studies of two-phase gas-liquid flow in microgravity. *NASA Contractor Report 195434*, 1995.

[11] W.S. Bousman, J.B. McQuillen, and L.C. Witte. Gas-liquid flow patterns in microgravity: effects of tube diameter, liquid viscosity and surface tension. *Int. J. Multiphase Flow*, 22(6):1035–1053, 1996.

[12] J.U. Brackbill, D.B. Kothe, and C. Zemach. A continuum method for modelling surface tension. *Journal of Computational Physics*, 100(2):335–354, 1992.

[13] F.P. Bretherton. The motion of long bubbles in tubes. *J. Fluid Mech.*, 10:166–188, 1961.

[14] J. Carrera, R.N. Parthasarathy, and S.R. Gollahalli. Bubble formation from a free-standing tube in microg. *Chem. Eng. S.*, 61:7007, 2006.

[15] J. Carrera, X. Ruiz, L. Ramírez-Piscina, J. Casademunt, and M. Dreyer. Generation of a monodisperse microbubble jet in microgravity. *AIAA Journal*, 46:2010–1019, 2008.

[16] C. Colin and J. Fabré. Gas-liquid pipe flow under microgravity conditions: influence of tube diameter on flow pattern and pressure drops. *J. Adv. Space Research*, 16:137–142, 1995.

[17] C. Colin, J. Fabré, and A.E. Dukler. Gas-liquid flow at microgravity conditions - I (dispersed bubble and slug flow). *International Journal of Multiphase Flow*, 17:533–544, 1991.

[18] C. Colin, J. Fabré, and McQuillen. Bubble and slug flow at microgravity conditions: state of knowledge and open questions. *Chem. Eng. Comm.*, 141/142:155–173, 1996.

[19] R. Collins, F.F. De Moraes, J.F. Davidson, and D. Harrison. The motion of large bubbles rising though liquid flowing in a tube. *J. F*, 89:497–514, 1978.

[20] C.J. Crowley, M.G. Izenson, J. Barry, J.L. Martin, R.S. Ent, and J.A. Valenzuela. Design manual for two-phase components of spacecraft thermal management systems. *PL-TR-92-3002*, 1992.

[21] C.A. Damianides and J.W. Westwater. Two-phase flow patterns in a compact heat exchanger and in small tubes. *In: Proc. Second UK National Conf. On Heat Transfer, Glasgow, 14-16 September, Mechanical Engineering Publications, London*, pages 1257–1268, 1988.

[22] A.E. Dukler, J.A. Fabré, J.B. McQuillen, and R. Vernon. Gas-liquid flow at microgravity conditions: flow patterns and their transitions. *International Journal of Multiphase Flow*, 14:389Â–400, 1988.

[23] A.E. Dukler and M.G. Hubbard. A model for gas liquid slug flow in horizontal and near horizontal tubes. *Ind. Eng. Chem. Fundam*, 14:337–47, 1975.

[24] J.-B. Dupont and D. Legendre. Numerical simulation of static and sliding drop with contact angle hysteresis. *J. Comput. Phys.*, 229:2453–2478, 2010.

[25] R.E. Eastman, C.J Feldmanis, W.L. Haskin, and K.L. Weaver. Two-phase fluid thermal transport for spacecraft. *AFWAL-TR-84-3028*, 1984.

[26] J. Fabre and A. Liné. Modeling of two-phase slug flow. *Annu*, 24:21–46, 1992.

[27] R.C. Fernandes. Experimental and theoretical studies of isothermal upward gas-liquid flows in vertical tubes. *PhD thesis, Univ. Houston*, 1981.

[28] R.C. Fernandes, R. Semiat, and A.E. Dukler. A hydrodynamic model for gas-liquid slug flow in vertical tubes. *AIChE J.*, 29:981–989, 1983.

[29] Figueroa and J. Fabré. Taylor bubble moving in a flowing liquid in vertical channel: transition from symmetric to asymmetric shape. *J. Fluid Mech.*, (Submitted).

[30] S.E. Forrester and C.D. Rielly. Bubble formation from cylindrical, flat and concave sections exposed to a strong liquid cross-flow. *Chem. Eng. Sci.*, 53:1517Â–1527, 1998.

[31] D. Fréchou. Etude de l'écoulement ascendant á trois fluides en conduite verticale. *Tése Inst. Natl. Polytech., Toulouse*, 1986.

[32] T. Fu, D. Funfschilling Y. Ma, C. Zhu, and H.Z. Li. Squeezing-to-dripping transition for bubble formation in a microfluidic t-junction. *Chem. Eng. Sci.*, 65(12):3739–3748, 2010.

[33] K.S. Gabriel. Microgravity two-phase flow and heat transfer. *Microcosm Press and Springer*, 2007.

[34] P. Garstecki, M. J. Fuerstman, H. A. Stone, and G. M. Whitesides. Formation of droplets and bubbles in a microfluidic t-junction scaling and mechanism of break-up. *The Royal Society of Chemistry*, 6:437–446, 2006.

[35] P. Garstecki, I. Gitlin, W. DiLuzio, G.M. Whitesides, E. Kumacheva, and H.A. Formation of monodisperse bubbles in a microfluidic flow-focusing device. *Appl. Phys. Lett.*, 85:2649–2651, 2004.

[36] G. W. Govier and K. Aziz. The flow of complex mixtures in pipes,. *Van Nostrand-Reinhold*, 503, 1972.

[37] G.A. Gregory and D.S. Scott. Correlation of liquid slug velocity and frequency in horizontal cocurrent gas-liquid slug flow. *AIC*, 15:833–35, 1969.

[38] D.B. Heppner, C.D. King, and J.W. Littles. Zero-g experiments in two-phase fluids flow patterns. *In: ICES Conf.San Francisco, CA, ASME paper No. TS-ENAs-24*, 1975.

[39] S.A. Hill, C. Kostyk, B. Motil, W. Notardonato, S. Rickman, and T. Swanson. Thermal management systems roadmap. *National Aeronautics and Space Administration*, November 2010.

[40] K. Hurlbert, B. Bagdigian, C. Carroll, A. Jeevarajan, M. Kliss, and B. Singh. Human health, life support and habitation systems roadmap. *National Aeronautics and Space Administration*, November 2010.

[41] E. Iacona, C. Herman, S. Chang, and Z. Liu. Electric field effect on bubble detachment in reduced gravity environment. *Therm. Fluid Sci.*, 31:121Â–126, 2006.

[42] M. Ishii. One-dimensional drift-flux model and constitutive equations for relative motion between phases in various two-phase flow regimes. *Argonne National Lab Report*, ANL 77-47, 1977.

[43] S.B.R. Karri and V.K. Mathur. Two-phase flow pattern map predictions under microgravity. *AIChE J.*, 34:137–139, 1988.

[44] M.N. Kashid, F. Platte, D.W. Agar, and S. Turek. Computational modelling of slug flow in a capillary microreactor. *J. Comput. Appl. Math.*, 203:487–497, 2007.

[45] A.A. Kulkarni and J.B. Joshi. Bubble formation and bubble rise in gas-liquid system: a review. *Ind. Eng. Chem. Res.*, 44:5873–5931, 2005.

[46] B. Lafaurie, C. Nardone, R. Scardovelli, S. Zaleski, and G. Zanetti. Modelling merging and fragmentation in multiphase flows with surfer. *J.Comp.Phys.*, 113:134–147, 1994.

[47] D. Lee. Thermohydraulic and flow regime analysis for condensing two-phase flow in a microgravity environment. *PhD thesis, Texas A&M University*, 1987.

[48] D. Legendre. On the relation between the drag and the vorticity produced on a clean bubble. *Phys. Fluids*, 19:018102, 2007.

[49] D. Legendre and C. Colin. Enhancement of wall-friction by fixed cap-bubbles. *Phys. Fluids*, 20:051704, 2008.

[50] D. Legendre, E. Lauga, and J. Magnaudet. Influence of slip on the dynamics of two-dimensional wakes. *J. Fluid. Mech.*, 633:437–447, 2009.

[51] D. Legendre and J. Magnaudet. The lift force on a spherical bubble in a viscous linear shear flow. *J. Fluid. Mech.*, 368:81–126, 1998.

[52] D. Legendre, J. Magnaudet, and G. Mougin. Hydrodynamic interactions between two spherical bubbles rising side by side in a viscous liquid. *J. Fluid Mech.*, 497:133–166, 2003.

[53] H. Liu, C.O. Vandu, and R. Krishna. Hydrodynamics of Taylor flow in vertical capillaries: flow regime, bubble rise velocity, liquid slug length and pressure drop. *Ind. Eng. Chem. Res*, 44:4884–4897, 2005.

[54] V.J. Lyons, G.A. Gonzalez, M.G. Houts, C.J. Iannello, J.H. Scott, and S. Surampudi. In-space power and energy storage roadmap. *National Aeronautics and Space Administration*, November 2010.

[55] J. Magnaudet and I. Eames. The motion of high-reynolds-number bubbles in inhomogeneous flows. *Annu. Rev. Fluid Mech.*, 32:659–708, 2000.

[56] J. Magnaudet, M. Rivero, and J. Fabré. Accelerated flows past a rigid sphere or a spherical bubble. Part 1: steady straining flow. *J. Fluid Mech.*, pages 97–135, 1995.

[57] P. Di Marco, W. Grassi, G. Memoli, T. Takamasa, A. Tomiyama, and S. Hosokawa. Influence of electric field on single gas bubble growth and detachment in microgravity. *Int. J. Multiph. Flows*, 29:559–578, 2003.

[58] J. McQuillen, C. Colin, and J. Fabré. Ground-based gas-liquid flow research in microgravity conditions: state of knowledge. *Space Forum*, 3:165–203, 1998.

[59] M. De Menech, P. Garstecki, F. Jousse, and H.A. Stone. Transition from squeezing to dripping in a microfluidic T-shaped junction. *J. Fluid Mech.*, 595:141–161, 2008.

[60] L. Ménétrier-Deremble and P. Tabeling. Droplet breakup in microfluidic junctions of arbitrary angles. *Phys. Rev. E*, 74:035303(R), 2006.

[61] M. Meyer, L. Johnson, B. Palaszewsky, D. Goebel, H. White, and D. Coote. In-space propulsion system roadmap. *National Aeronautics and Space Administration*, November 2010.

[62] D.W. Moore. The boundary layer on a spherical gas bubble. *J. Fluid Mech.*, 16:161–176, 1963.

[63] H.K. Nahra and Y. Kamotani. Bubble formation from wall orifice in liquid cross-flow under low gravity. *Chemical Engineering Science*, 55:4653–4665, 2000.

[64] H.K. Nahra and Y. Kamotani. Prediction of bubble diameter at detachment from a wall orifice in liquid cross-flow under reduced and normal gravity conditions. *Chemical Engineering Science*, 58:55–69, 2003.

[65] H. Ngoc and J. Fabré. The velocity and shape of 2D long bubbles in inclined channels or in vertical tubes. Part I: in a stagnant liquid. *Multiphase Sciences and Technology*, 16:175–188, 2004.

[66] D.J. Nicklin, J.O Wilkes, and J.F. Davidson. Two phase flow in vertical tubes. *Trans. Inst. Chem. Eng.*, 40:61–68, 1962.

[67] Z. Nie, M. Seo, S. Xu, P.C. Lewis, M. Mok, E. Kumacheva, G.M. Whitesides, P. Garstecki, and H.A. Stone. Emulsification in a microfluidic flow-focusing device: effect of the viscosities of the liquids. *Microfluid Nanofluid*, 5:584–594, 2008.

[68] H. Ohta, A. Baba, and K. Gabriel. Review of existing research on microgravity boiling and two-phase flow. *Ann. N.Y. Acad. Sci.*, 974:41, 2002.

[69] S. Ostrach. Industrial processes influenced by gravity. *NASA CR-182140, C-21066-G*, 1988.

[70] S.C. Pais, Y. Kamotani, A. Bhunia, and S. Ostrach. Bubble generation in a flowing liquid medium and resulting two-phase flow in microgravity. *Proceedings of the Fourth Microgravity Fluid Physics and Transport Phenomena Conference, NASA*, pages pp. 70–77, 1999.

[71] O. Pampering and H.J. Rath. Influence of buoyancy on bubble formation at submerged orifices. *Chem. Eng. Sci.*, 50:3009–3024, 1995.

[72] S. Popinet and S. Zaleski. A front-tracking algorithm for accurate representation of surface tension. *Int. J. Numeric. Meth. Fluid*, 30:775–793, 1999.

[73] D. Qian and A. Lawal. Numerical study on gas and liquid slugs for Taylor flows in a t-junction microchannel. *Chem. Eng. Sci.*, 61:7609–7625, 2006.

[74] T.R. Reinarts. Adiabatics two phase flow and modelling for zero and reduced (horizontal flow) acceleration fields. *Pd D Thesis, Texas, A&M University*, 1993.

[75] T.R. Reinarts. Slug to annular flow regime transition modelling for two-phase flow in a zero gravity environment. *In: Proceedings of 30th International Energy Conversion Engineering Conference, Orlando, FL*, 1995.

[76] R. Revellin, B. Agostini, T. Ursenbacher, and J.R. Thome. Experimental investigation of velocity and length of elongated bubbles for flow of r-134a in a 0.5 mm microchannel. *Experimental Thermal and Fluid Science*, 32:870–881, 2008.

[77] K.S. Rezkallah. Weber number based flow-pattern maps for liquid-gas flows at microgravity. *J. Multiphase Flow*, 22 (6):1265–1270, 1996.

[78] F. Sarrazin, T. Bonometti, L. Prat, C. Gourdon, and J. Magnaudet. J. hydrodynamic structures of droplets engineered in rectangular micro-channels. *Micro. Nano*, 5:131–137, 2008.

[79] R. Scardovelli and S. Zaleski. Direct numerical simulation of free surface and interfacial flow. *Ann. Rev. Fluid Mech.*, 31:567, 1999.

[80] N. Sen. Suratman number in bubble-to-slug flow pattern transition under microgravity. *Acta Astronautica*, 65:423–428, 2009.

[81] J. Sethian. Level set methods and fast marching methods. *Cambridge University Press*, 1999.

[82] V. Steijn, C.R. Kleijn, and M.T. Kreutze. Flows around confined bubbles and their importance in triggering pinch-off. *Physical Review Letters*, 103:214501, 2009.

[83] M. Suo and P. Griffith. Two-phase flow in capillary tubes. *J. Basic Eng.*, 86:576–582, 1964.

[84] M. Sussman, E. Fatemi, P. Smereka, and S. Osher. A level set approach for computing solutions in incompressible two-phase flows. *Comput. Fluids*, 27:567, 1998.

[85] G.I. Taylor. Deposition of a viscous fluid on the wall of a tube. *J. Fluid Mech.*, 10(2):161–165, 1961.

[86] K.A. Triplett, S.M. Ghiaasiaan, S.I. Abdel-Khalik, A. LeMouel, and B.N. McCord. Gas-liquid two-phase flow in microchannels. Part II: void fraction and pressure drop. *Int. J. Multiph. Flows*, 25:395–410, 1999b.

[87] K.A. Triplett, S.M. Ghiaasiaan, S.I. Abdel-Khalik, and S.A. Sadowdki. Gas-liquid two-phase flow in microchannels. Part I: two-phase flow patterns. *Int. J. Multiph. Flows*, 25:377–394, 1999a.

[88] J.-R. Turnau, H. Ngoc, and J. Fabré. The motion of long bubbles in tube at negligible gravity. *6th International Conference on Multiphase Flow, ICMF*, 2007.

[89] G.B. Wallis. *One-Dinemsional Two-Phase Flow*. New York: McGraw-Hill, 1969.

[90] S.T. Zalesak. Fully multidimentional flux-corrected transport algorithms for fluids. *J. Comput. Phys.*, 31:335–362, 1979.

[91] J.F. Zhao. A review of two-phase gas-liquid flow patterns under microgravity conditions. *Adv. in Mech. (Chinese)*, 29:369–382, 1999.

[92] L. Zhao and K.S. Rezkallah. Gas-liquid flow patterns at microgravity conditions. *Int. J. Multiphase Flow*, 19:751–763, 1993.

[93] N. Zuber and J.A. Findlay. Average volumetric concentration in two-phase flow systems. *J. Heat Transfer*, 87:458–463, 1965.

Publications

Articles

S. Arias, X. Ruiz, J. Casademunt, L. Ramírez-Piscina, and R. González-Cinca. Experimental study of a microchannel bubble injector for microgravity applications. *Microgravity Sci. Technol.* 21:107-111, 2009.

S. Arias, R. González-Cinca, X. Ruiz, L. Ramírez-Piscina, and J. Casademunt. Characterization of the performance of a minibubbles generator in conditions relevant to microgravity. *Colloids and Surfaces A: Physicochem. Eng. Aspects* 365: 52-55, 2010.

S. Arias, D. Legendre, and R. González-Cinca. Numerical simulation of bubble generation in a T-junction. Submitted at *Computers & Fluids* in January 2011.

Conferences

S. Arias, X. Ruiz, L. Ramírez-Piscina, J. Carrera, J. Casademunt, and R. González-Cinca. Experimental study of a microbubble Injector for microgravity applications. *International Workshop on Bubble and Drop Interface*, Granada (Spain), 2007.

J. Carrera, X. Ruiz, P. Bitlloch, L. Ramírez-Piscina, S. Arias, R. González-Cinca, M. Dreyer, and J. Casademunt. A study of a monodisperse microbubble jet under microgravity conditions. *Experiments in Space and Beyond*, Brussels (Belgium), 2007.

S. Arias, X. Ruiz, L. Ramírez-Piscina, J. Carrera, J. Casademunt, and R. González-Cinca. Experimental characterization of a microbubble inyector. *European Low*

Gravity Research Association (ELGRA), Florence (Italy), 2007.

S. Arias, X. Ruiz, L. Ramírez-Piscina, J. Carrera, J. Casademunt, and R. González-Cinca. Characterization of a microbubble injector for applications in microgravity. *Experiments in Space and Beyond*, Brussels (Belgium), 2007.

S. Arias, X. Ruiz, L. Ramírez-Piscina, J. Carrera, J. Casademunt, and R. González-Cinca. Microbubble injector: an experimental quantitative characterization. *3rd International Workshop on Bubble and Drop Interfaces*, Nara (Japan), 2007.

S. Arias, X. Ruiz, L. Ramírez-Piscina, J. Carrera, J. Casademunt, and R. González-Cinca. Characterization of the performance o an injector for the generation of controlled microbubbles. *Third International Topical Team Workshop on two-phase systems for ground and space applications*, Brussels (Belgium), 2008.

S. Arias, X. Ruiz, L. Ramírez-Piscina, J. Carrera, J. Casademunt, and R. González-Cinca. Characterization of the performance o an injector for the controlled generation of microbubbles. *International Astronautical Congress*, Glasgow (Scotland), 2008.

S. Arias and R. González-Cinca. Characterization of bubbly and slug flow regimes generated in a minichannel in microgravity conditions. *International Workshop on Bubble and Drop Interfaces*, Thessaloniki (Greece), 2009.

S. Arias and R. González-Cinca. Experimental analysis of the bubble-slug transition in a minichannel in microgravity conditions. *European Low Gravity Research Association (ELGRA)*, Bonn (Germany), 2009.

S. Arias, R. Garby, and R. González-Cinca. Comparison of two methods for generating small bubbles in microgravity conditions. *38th COSPAR Scientific Assembly*, Bremen (Germany), 2010.

S. Arias, D. Legendre, and R. González-Cinca. Numerical simulation of bubble generation in a T-junction. *4th International Symposium on Physical Sciences in Space ISPS4*, Bonn-Bad Godesberg, (Germany), 2011.

S. Arias and R. González-Cinca. Comparison of two methods for generating small bubbles with a T-junction in microgravity conditions. *European Low Gravity Research Association (ELGRA)*, Antwerp, (Belgium), 2011.